1-1-2019

Quantitative Aspects of Interface Remodeling During Germband Extension

Timothy E. Vanderleest
University of Denver

Recommended Citation

Vanderleest, Timothy E., "Quantitative Aspects of Interface Remodeling During Germband Extension" (2019). *Electronic Theses and Dissertations*. 1551.
https://digitalcommons.du.edu/etd/1551

Quantitative Aspects of Interface Remodeling during Germband Extension

A Dissertation
Presented to
the Faculty of Natural Sciences and Mathematics
University of Denver

In Partial Fulfillment
of the Requirements for the Degree
Doctor of Philosophy

by
Timothy E. Vanderleest
March 2019
Advisor: Dinah Loerke

Author: Timothy E. Vanderleest
Title: Quantitative Aspects of Interface Remodeling during Germband Extension
Advisor: Dinah Loerke
Degree Date: March 2019

Abstract

Oriented cell intercalation is an essential developmental process that shapes tissue morphologies through the directional insertion of cells between their neighbors. Intercalary behaviors in the early *Drosophila* embryo occur through a remodeling of cell topologies, with cells contracting shared AP interfaces to a single point, followed by newly juxtaposed DV cells constructing horizontally-oriented interfaces between them. Previous research has focused on properties of cell-cell interfaces, and led to a model in which actomyosin networks mediate higher line tensions at AP interfaces to direct contraction. However, the contribution of tricellular vertices to tissue elongation remains unclear. This study shows that cell intercalation uses a novel sliding vertex mechanism that physically couples vertices to radially-oriented forces. Through live imaging and quantitative analysis it was observed that the motion of vertices at contracting interfaces is not coupled, but instead vertices demonstrate strong radial coupling across the area of cells. The vertices of AP junctions show independent sliding behaviors along the cell periphery to produce the topological deformations responsible for intercalation. AP junctions undergo ratcheted length changes that are coordinated with cell area oscillations. These results suggest a model in which oscillations in cell area direct the progressive, ratcheted motion of individual vertices to drive oriented cell intercalation and tissue extension in the *Drosophila* epithelium.

In a second study, analysis of germband extension in 4D revealed that interface contraction and T2 formation can initiate from any point along on the apical-basal

axis, including basolateral regions microns away from the apical caps that host major Myosin II populations. Intriguingly, interface contractions transition smoothly into elongations without systematic T2 waiting times and at similar contraction and elongation speeds, suggesting that a common mechanism may underlie both phases of intercalation. This study also showed that the major component of tissue elongation arises from the growth of new interfaces.

In a third study, the focus was on the role of membrane trafficking during germband extension. The results of this study showed that Rab35 compartments are enriched at contractile interfaces of intercalating cells. When Rab35 function is disrupted, apical area oscillations still occur and contractile steps are observed. However, contractions are followed by reversals and interfaces fail to shorten, demonstrating that Rab35 functions as a ratchet ensuring unidirectional movement. Finally, Rab35 represents a common contractile cell-shaping mechanism, as mesoderm invagination fails in Rab35 compromised embryos and Rab35 localizes to constricting surfaces.

In a fourth and final study, the functional requirements for exocyst complex function during cell division in vivo was investigated, and a common mechanism that directs anaphase cell elongation and cleavage furrow progression during cell division was demonstrated. The results of this study show that onion rings (*onr*) and funnel cakes (*fun*) encode the *Drosophila* homologs of the Exo84 and Sec8 exocyst subunits, respectively. In *onr* and *fun* mutant cells, cytokinesis is disrupted early in furrow ingression, leading to cytokinesis failure. Computational analysis was used to quantitatively compare wild-type versus *onr* and *fun* mutant cells. The results demonstrate that anaphase cell elongation is grossly disrupted in cells that are compromised in exocyst complex function. Additionally, compared to wild-type, *onr* and *fun* mutant cells have a greatly reduced rate of surface area growth specifically during cell division.

Acknowledgements

I would like to express my deepest gratitude and appreciation for my advisor, Dinah Loerke, for her continued support and mentoring over the years. She has taught me so much about image analysis and how to approach problems and implement solutions with MATLAB.

I am also extremely grateful to Todd Blankenship who was a close collaborator on all the projects presented in this dissertation. I have learned so much biology from Todd through his journal club and through private research meetings.

I would like to thank my committee: Dinah Loerke, Todd Blankenship, Michelle Knowles, Joseph Angleson, and my committee chair Ali Azadani.

I want to thank the many other members of Todd's lab who acquired the image data that I was able to analyze and were so helpful in providing me with any information that I needed such as embryo orientations, frame acquisition rates, or pixel sizes: Celia Smits, Cayla Jewett, Yi Xie, Hui Miao, Ashley Motlong, Robyn Harte, and Marissa Kuhl. A special thanks to Celia Smits for her significant contributions on the vertex sliding publication: tons of imaging, helping with figure and video making, and helping with the writing.

Last but not least, I want to thank the other members of our lab, Roopa Madhu and Noah De Leeuw. Together we have been a great team in listening and giving advise during mock presentations, helping each other understand the tough parts of Todd's journal club papers, and working through MATLAB issues together.

Contents

List of Figures

Chapter 1

Introduction

A common characteristic of many tissues and organisms is an elongation along a primary dimensional axis. The oriented intercalation of cells is one of the fundamental mechanisms utilized to direct tissue elongation [35]. Tissue elongation is essential to the shaping of an elongated body axis [35, 30], as well as the development of many internal organs, such as the palate, cochlea, gut, and kidney [10, 64, 67, 42]. Epithelial cell intercalation drives elongation of the *Drosophila* body axis during gastrulation (Fig. 1.1A and B), in a process known as germband extension (GBE; [30]). The intercalary behaviors driving GBE occur through a remodeling of cell topologies, with cells contracting shared anterior-posterior (AP, vertical or T1) interfaces to a single point, followed by newly juxtaposed dorsal-ventral (DV) cells constructing horizontally-oriented interfaces between them (Fig. 1.1C; [30, 4, 5, 13, 31]). This is referred to as a topological T1 process, and results in a cumulative contraction of the embryonic epithelium along the DV axis, which helps to drive a perpendicular elongation along the AP axis.

In addition to T1 processes there are higher order intercalation events known as rosettes [5]. Rosettes form when multiple linked vertical interfaces contract to bring 5 or more cells into a single vertex (Fig. 1.1C) and rosettes resolve into

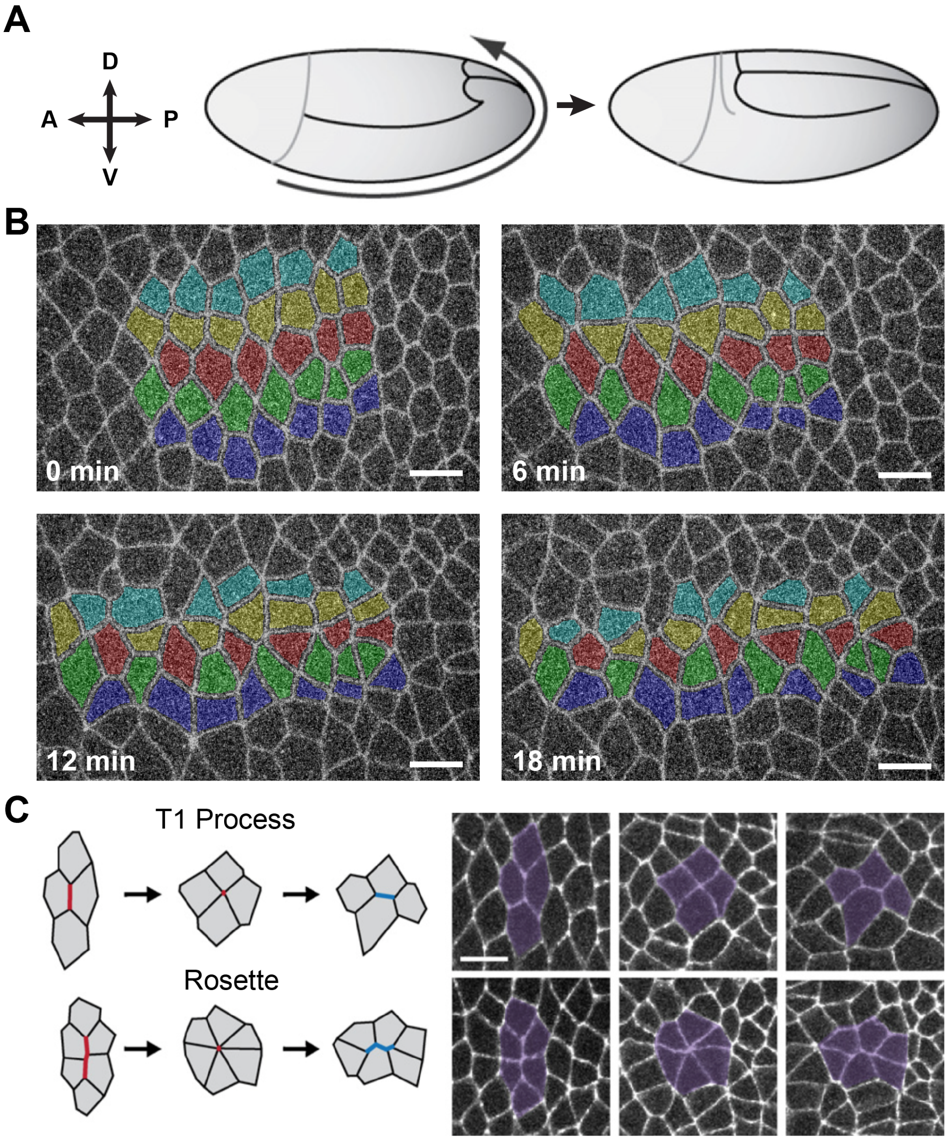

Figure 1.1: GBE occurs via cell intercalation. (**A**) Illustration of the germband tissue elongating towards the posterior and folding upward and around to the dorsal side of the embryo. Anterior, posterior, dorsal, and ventral are labeled A, P, D, and V respectively. Illustration is modified from [66]. (**B**) Intercalation shown through time lapse images of the germband with rows of cells tracked and colored. (**C**) Illustration of a type T1 process (top) and a rosette (bottom). Illustration is modified from [66]. Scale bars are 10 μm.

multiple elongating horizontal interfaces. Rosettes will not be a topic covered in this dissertation which is primarily focused on T1 processes.

The organization of this dissertation is as follows. The first four chapters of this dissertation (Introduction, Methods, Results, and Discussion) are each composed of three different main sections corresponding to three different projects on germband extension. The fifth and final chapter is based on a project on an entirely different system, cytokinesis, and contains its own Intro, Methods, Results, and Discussion sections.

1.1 Uncoupled Vertex Sliding

Previous research into the genetic factors associated with GBE has shown that global polarizing cues from maternal AP patterning are translated into asymmetric protein distributions at the cellular level [30, 5]. At AP interfaces, Myosin II forms both supracellular cables and smaller, transient networks. Protein populations associated with adhesion (E-cadherin, β-catenin, Bazooka/Par-3) are found enriched at non-contracting interfaces [5]. This body of work led to a model in which actomyosin networks mediate higher line tensions along AP interfaces to direct contraction [19, 50]. However, these studies have been limited to the molecular and mechanical characteristics of interfaces between two cells. The discrete regions where these interfaces overlap, tricellular vertices, have never been comprehensively examined.

As a result of the focus on cell-cell interfaces, many studies on force-generation during intercalation have addressed forces oriented along the cell cortex [4, 19, 50, 33, 17, 13, 31, 60]. However, Myosin II populations are highly active and are transiently present in multiple locations in epithelial cells, including in medial and apical cell regions [49, 20, 54, 60]. These medial actomyosin networks drive a number of morphogenetic processes by mediating oscillations in cell area

[43, 53, 57, 2]. Indeed, during GBE medial Myosin II flows direct apical area oscillations that contribute to AP/DV anisotropy within a cell [49, 20, 54]. However, the mechanisms by which they could be linked to cell-neighbor exchange have been unclear.

Results show that vertices move independently of one another during T1 contraction, and exhibit distinct molecular dynamics that are required for effective intercalation. Intercalation proceeds through a sliding vertex mechanism that physically couples vertex motion to radially-oriented forces. E-cadherin and Myosin II are strikingly enriched at vertices, and this vertex enrichment coincides with length stabilization post-sliding. E-cadherin recruitment at vertices is coordinated with apical cell area oscillations, and is favored at vertices associated with AP interfaces. Finally, perturbing Myosin II function reduces E-cadherin enrichment and dynamics at vertices, and leads to a loss of productive intercalation. Together, these observations provide a mechanism by which area oscillations are coupled to cyclic molecular dynamics, and further introduce a link between the molecular properties of tricellular vertices and the emergent biophysical properties of the tissue.

1.2 GBE Along the Apico-Basal Axis and T2-T3 Processes

Currently little is known about what happens at the basal side of the epithelium during GBE. In the canonical model, the apical side of the tissue is where tissue extension is being driven and the basal side extends passively as a result of the apical cell rearrangements. The basis for this model is that the major proteins associated with mechanical force (Actin and Myosin II) and tissue adhesion (E-cadherin) are enriched apically (Fig. 1.2), particularly within the apical-most 2 or 3 microns of cells with a total apico-basal length of about 30 microns. One issue why the basal region of the epithelium perhaps has not received much attention is that it is difficult to get quality imaging basally due to light scattering. Imaging done by the Blankenship lab produced movies where the signal to noise was sufficient to segment the epithelium from the apical cap to about 12 microns deep. This data allowed the observation of cell area oscillations, interface length changes, and in particular type T1 transitions along the apico-basal axis. In one recent study, imaging along the apical-basal axis was performed to study rosette formation and they found that actin-rich basolateral protrusions of dorsal/ventral cells was a driver of rosette formation and that rosettes sometimes formed basally before apically [60].

In this project it was observed that cells display very similar interface dynamics between T1-T2 and T2-T3 transitions and do not possess substantial T2 waiting times, suggesting that a common mechanism may underlie the contraction and elongation phases of intercalary cell movements. Additionally, AP interface contraction is initiated along the full length of the observable apical-basal axis, including lateral regions that are removed from apical myosin populations.

1.3 The Role of Rab35 in GBE

The combination of tension-producing actomyosin networks and cadherin-dependent adhesion complexes are believed to be central determinants directing early morphogenesis in the *Drosophila* embryo; however, the role of membrane trafficking in guiding these events has been less clear [66, 39]. Additionally, how periods of active cytoskeletal contraction are tied to processes that function at the plasma membrane to ensure the consolidation and irreversibility of changes is unclear.

The Rab family of small GTPase proteins are key mediators of membrane trafficking and cytoskeletal dynamics. Rab proteins regulate membrane

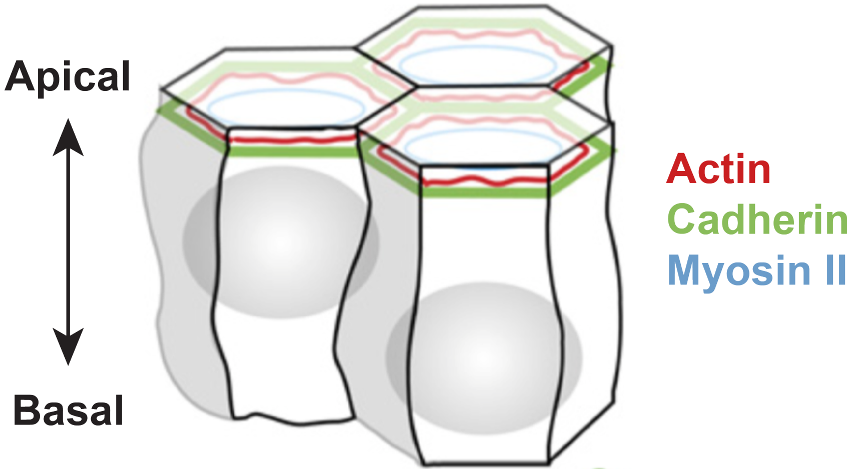

Figure 1.2: 3D illustration of germband epithelial cells with the important proteins (Actin in red, E-cadherin in green, and Myosin II in blue) and their apical localization color coded. Image modified from [18].

compartment behaviors through their association with tethering and trafficking effectors [48, 24, 27], and mutations in Rab proteins are associated with a variety of diseases and developmental disorders [3, 45, 51, 26]. The Rab trafficking pathways that operate during cell intercalation in the early *Drosophila* gastrula have remained undefined, although the function of classic Clathrin and Dynamin-dependent early endocytic pathways has been explored [41]. It has been demonstrated that Formin and Myosin II proteins direct the endocytic uptake of dextran through specialized CIV (cortical immobile vesicle) structures [41]. Additionally, in *Drosophila*, Rab35 has been shown to play a critical role in directing the morphogenesis of tracheal tube growth as well as synaptic vesicle sorting at the neuromuscular junction [65, 55]. In tissue culture models, Rab35 functions early in endosomal pathways to drive the generation of newborn endosomes and is essential for the terminal steps of cytokinesis and neurite outgrowth [38, 12, 15, 36, 11, 37, 9, 22].

This study shows that Rab35 demonstrates compartmental behaviors at the plasma membrane. Rab35 compartments are initially contiguous with the cell surface and form dynamic structures that grow and shrink on the minute time scale. In the absence of Rab35 function, cell interfaces undergo contractile steps, but these steps rapidly reverse themselves, consistent with Rab35 mediating an essential "ratcheting" function that directs progressive interface contraction.

Chapter 2

Methods

The basic process for every project presented in this dissertation is as follows: 1) segment the cells in the image or time-series of images, 2) track the cells in time, 3) extract and store the relevant information from the segmented images, and 4) analyze the data. The first step in this process, image segmentation, is often the most difficult task. Segmentation is the process by which an image is divided into objects of interest and the background. Looking at an image, one can instinctively make the distinction between objects and background with little effort, however, using computers to automate the task can be a significant challenge. The success of the final analysis depends on the quality of the segmentation and for that reason researchers have developed, and continue to develop, numerous segmentation techniques for various problems [34].

One of the goals of a successful computational segmentation algorithm is full automation. This is especially important when faced with large time series of images that include dozens or even hundreds of objects to be detected. If one were to manually segment such a data set by hand it would not only take extremely large amounts of time, the results would vary subject to who is doing the task, and even the same user may segment the same image differently from time to time. Thus, for the sake of speed and objectivity it is highly advantageous to have a fully or mostly automated computational segmentation algorithm.

2.1 Watershed Segmentation

One of the most commonly used techniques for image segmentation is the watershed transform. This algorithm gets its name because it treats an image as a topographic map where the brightness of the pixel represents the height. The basic idea is that each regional minimum (or catchment basin) on this topographic map is a water source and as the water level rises a barrier is formed when two different water sources meet (Fig. 2.1). The algorithm finds these barriers which amount to segments of the image that correspond to each regional minimum.

Two common problems with the watershed transform are over- and under-segmentation. Over-segmentation is the problem of having single objects that are segmented into multiple parts resulting in too many segments; this can be caused by image noise or some internal structure of the object that results in multiple minima or catchment basins. Under segmentation, on the other hand, is when the segmentation lines leak into other objects resulting in too few segments; this can be caused by the outline of the object having low signal in certain areas and therefore not providing a sufficient watershed.

2.1.1 Seeding

Performing the watershed transform directly on raw or filtered images often results in over-segmentation due to there being more than one local minima within a single cell. To overcome this issue the watershed transform is often combined with 'seeding' in a process named seeded watershed [1]. What seeding does is to essentially tell the watershed the only local minima to consider. In practice, a user must manually draw or in some way generate a binary image (or mask) of where

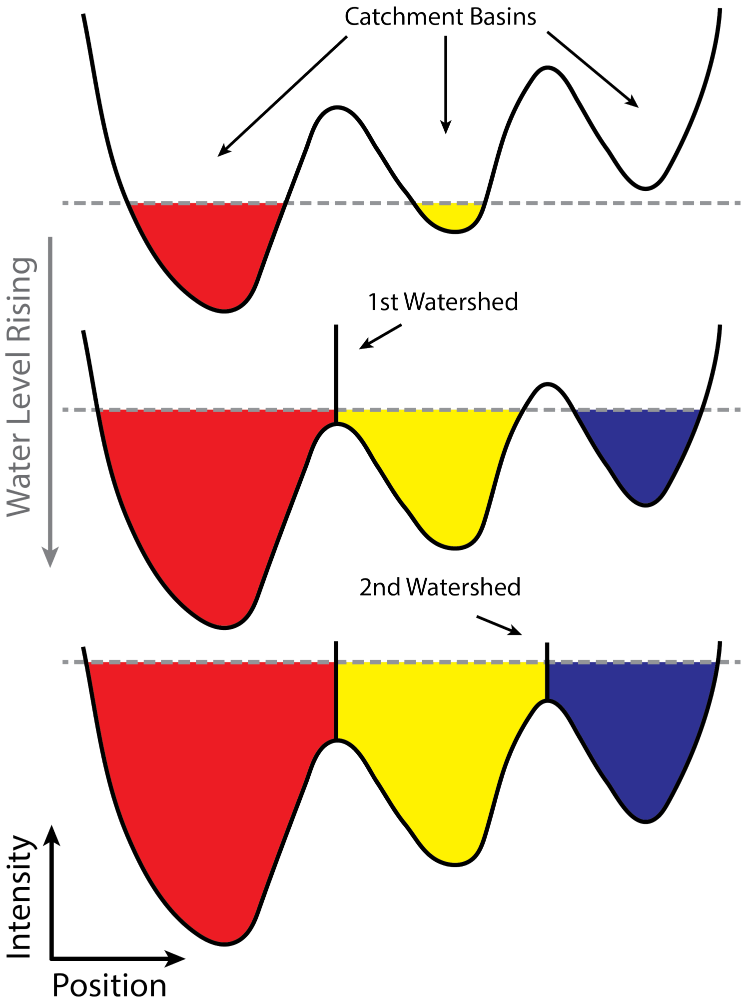

Figure 2.1: Illustration of the Watershed Transform in 1D. The black curve represents the hight of topological landscape (or image intensity) where the minima represent catchment basins. As the water level (gray dashed line) rises, the points at which the water from neighboring catchment basins meet becomes the watershed points (or watershed lines in the 2D case). In this example the curve is segmented into the three regions indicated by the colors red, yellow, and blue.

they want the seeds to be. Then, a morphological reconstruction algorithm (Matlab function *imimposemin*) ensures that the seed regions are the only regional minima in the image. The result of seeding is that the watershed produces one segment around each seed.

Seeds were used in two different ways: 1) seeds were used for objects of interest that data will be extracted from, and 2) seeds were used for objects to be ignored and excluded from data extraction, which here is called the ‘background mask’. The background mask is usually one large seed used to cover all the cells that lie on the boundary of the image which are incomplete. In some instances the background mask was also used to remove cells undergoing cytokinesis (undesirable for the purposes of this work) or regions of the image where signal-to-noise was low leading to a high frequency of segmentation errors.

There was also two different general seeding methods: 1) the point seed method and 2) the extended seed method (Fig. 2.2). Points seeds, as the name implies, were small circular spots (several pixels in diameter) placed within the cells. Point seeds were the most simple seeding method and were ideal in movies where there was little to no cytoplasmic signal. Extended seeds fill more of the cytoplasmic space and can be used to mask cytoplasmic features like vesicles or tubules that can sometimes be brighter than cell junctions and therefore cause segmentation errors. Also, in cases where the cell junction has low signal, extended seeds ensure that the segmentation boundaries stay in the right general location whereas with point seeds the error can be far more significant (Fig. 2.2).

2.1.2 Initiation and Manipulation of Seeds

Generating new seeds for an image was partially automated, generally requiring a couple minutes of manual editing. The automated component of the process essentially finds the regional minima in the Gaussian smoothed image and places

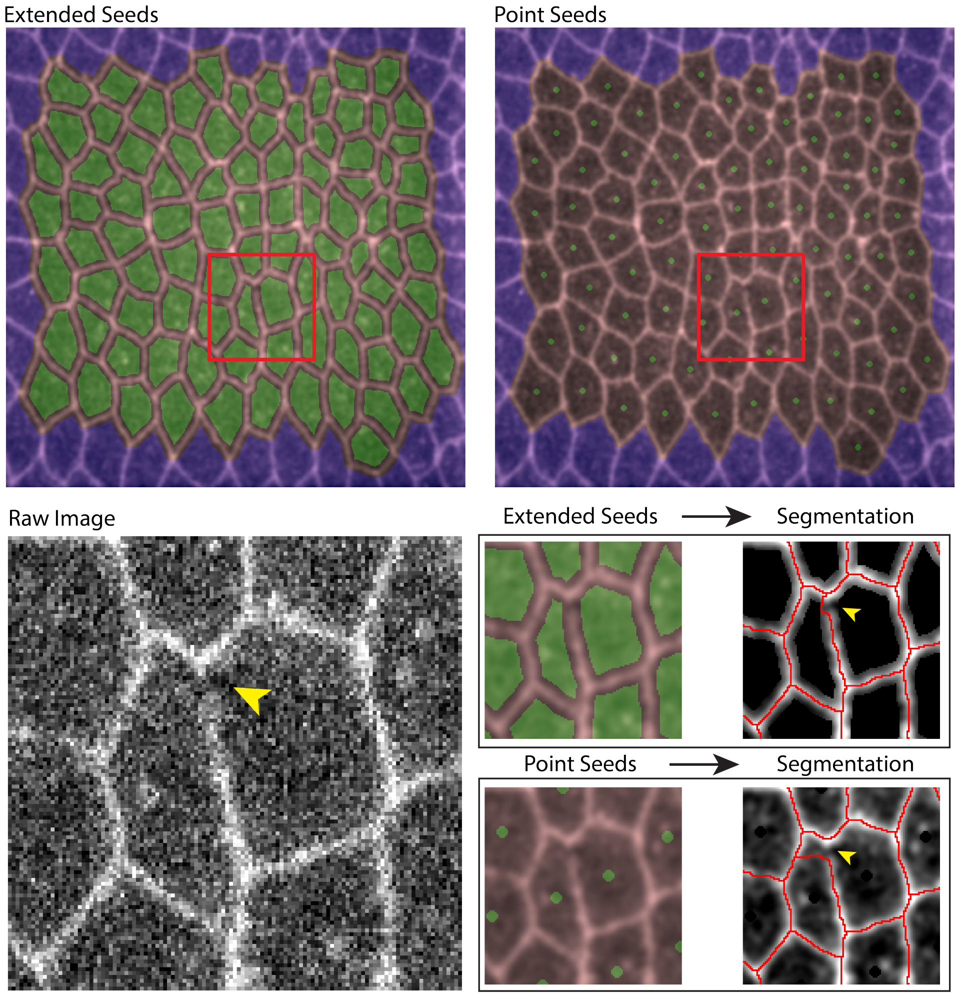

Figure 2.2: Two seed options are extended and point seeds. The top panels show full images of extended seeds (left) and point seeds (right). Seeds are the green regions and the background mask is shown in blue. A zoomed in raw image (bottom left; from red box in top panels) shows a section of the cell-cell junction with low signal (yellow arrowhead). Using point seeds leads to a segmentation error whereas extended seeds fix the error (bottom right).

point seeds at those locations. This step saves the user a lot of time that would be spent clicking on each cell, however on occasion in some cells it produces more than one seed (usually in large elongated cells), or no seeds (usually in smaller cells). The automated step also produces multiple seeds on the edges and corners of the image. Therefore, the manual component of the seed initiation involves 1) removing all edge seeds and adding a background mask, 2) removing duplicate seeds in cells, and 3) adding seeds to cells lacking a seed.

Manual editing of seeds can be a tedious process that really slows down movie segmentation. Therefore, it was important to develop a user interface to quickly and easily make changes to seeds and the background mask. This user interface was developed using MATLAB functions that gather positional data from mouse clicks on the image (and sometimes dragging) and use that positional data to create masks that can either add or remove pixels from seeds (or from the background mask). Due to the various types of situations encountered during segmentation various types of modification have been added and some less efficient or unused ones have been removed. Currently the types of modifications that are included in the user interface, the amount of mouse clicks they require, and what they are used for are as follows (Fig. 2.3):

1. “Add Point Seed” adds a point seed at the location of a single click and is often used as a quick way to begin segmenting new cells that come into the image.

2. “Add Line Seed” adds a line seed that can be added to another seed (or stand alone) and requires a click-drag-click. These are useful in narrow parts of a cell where segmentation errors are more likely due to the cell junctions being close to each other.

3. “Add Polygon Seed” adds a seed of any polygon shape that the user draws with one click per vertex of the polygon. This seed takes more time than adding a point seed however it is useful in situations where the user needs to cover a bright cytoplasmic feature or to ‘force’ a watershed along a junction that has too low signal-to-noise by drawing seeds on both sides of where that junction is.

4. “Add Polygon Mask” works the same as “Add Polygon Seed” except that it is used to draw and add polygon regions to the background mask.

5. “Remove Region” removes and entire continuous region (seed or background mask) with a single click anywhere on the region. This is useful for removing cells getting close to an edge or removing a seed that needs to be redrawn.

6. “Remove Polygon” removes any portion of a seed or background mask that is enclosed in the drawn polygon. This is useful in cases where a seed has ‘leaked’ into another cell and just a portion of the seed needs to be removed

7. “Erode Regions” morphologically erodes a seed or background mask with a single click anywhere on the region (and multiple clicks performs the erosion multiple times). This is sometimes a quicker way to correct a seed that has crossed over its’ cell boundary.

8. “Dilate Regions” morphologically erodes any region with a single click on the region (and multiple clicks performs the dilation multiple times). This is useful when a bright puncta near a cell junction needs to be covered up by a seed. However, the user must be careful that they don’t dilate the seed so much that it overlaps with any of the cell junctions.

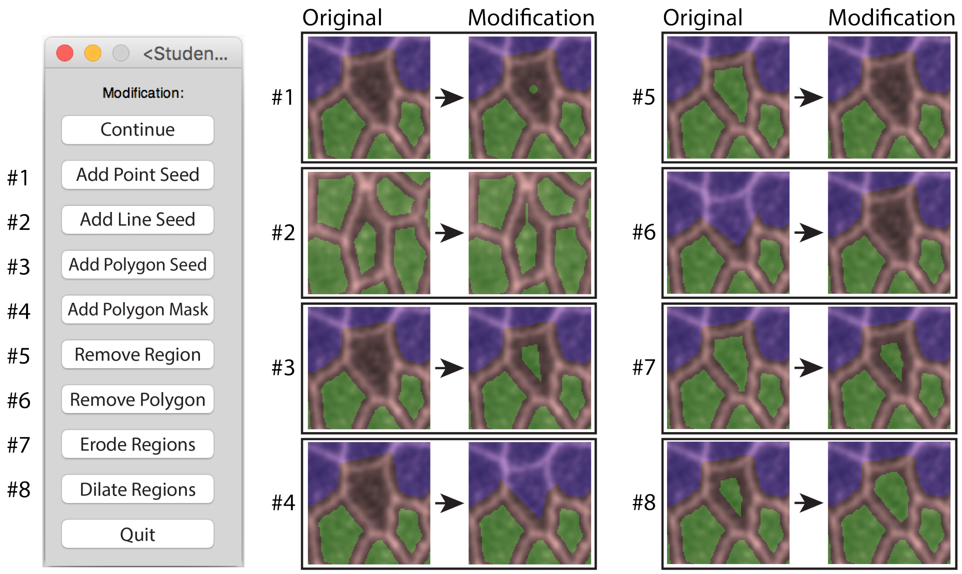

Figure 2.3: A user interface for quick and easy modification of seeds (green regions) or the background mask (blue regions) via mouse clicking, dragging, and drawing.

2.1.3 Segmentation of a Time Series

Segmentation of a time series is done by an iterative process that typically started from the first frame of the movie and with each iteration advances by one frame. For the first frame, seeds were initiated as described above and then the frame was segmented. To segment the next frame, seeds are generated from the segmentation result of the previous frame. If using point seeds, point seeds are placed at the centroid locations of the segmented regions. If using extended seeds, the segmented regions are morphologically eroded (which essentially shaves pixels off the region's perimeters) by an amount the user sees fit. This type of seed propagation is only possible if the cells are not moving so fast that frame-to-frame displacements are greater than the cell radius (when using point seeds) or if the displacements are less than the erosion radius (when using extended seeds). In general, if frame n has been segmented seeds can be propagated forward or backwards to segment frames $n+1$ or $n-1$.

The above described seed propagation technique allows for fully automated movie segmentation, however, due to a couple issues it was necessary to stop the iterative process periodically to check the results and make any necessary modifications. One issue was that, by the nature of germband extension, cells are constantly moving into and out of the field-of-view. To maximize the amount of cells tracked for data analysis it was important that new cells that came into the image were assigned new seeds. This usually involved removing the edge mask from the new cell (via the modification "Remove Polygon") and placing a point seed there with a single mouse click (which in the next iteration would become an extended seed). The other issue was that occasionally segmentation errors would occur and left unchecked they would propagate and sometimes get worse. Therefore, for each movie a 'check interval' frame number was chosen, i.e. the number of frames to iterate through before checking the results. The value of the check interval period was based on how fast cells moved in and out frame and how prone the movie was to segmentation errors.

2.1.4 Image Filtering

There is one last important pre-processing step before using the watershed transform algorithm. The raw images must be filtered before performing the watershed algorithm. Without filtering, the watershed segmentation boundaries end up jagged as a result of image noise. In all of the image data segmented for the projects presented in this dissertation a Gaussian filter was used. In cases where the movie contained image z-stacks a 3D spatial filter was used and in cases where the movie was a single z-plane a 2D spatial filter was used. The Gaussian parameter σ, which determines the spatial scale of smoothing, was typically 2 pixels in the x- and y-dimensions and if 3D, σ_z was typically 1 pixel. If the σ used was too small the segmented junctions between cells would be fairly jagged as a result of the image noise along cell junctions. If the σ used was too large then segmentation errors would arise in cases where part of the cell was narrow and two junctions were close together.

2.1.5 Data Extracted

The 'skeletonized' representation of the tissue directly yields vertex positions, interface contours, lengths and orientation angles, cell areas and perimeters, which were stored together with cell-cell and vertex-vertex connectivity matrices. Cell areas were measured as the sum of the pixels within the contour of the watershed segmentation lines (multiplied by a scale factor to convert to square microns). Interface lengths were calculated as the Euclidian distances between the corresponding vertices.

2.2 Uncoupled Vertex Sliding

2.2.1 Line Intensity Plots

Line plots were generated by Celia Smits as single pixel intensities along an interface line drawn manually in ImageJ, and the minimum value was subtracted from all data points and plotted using MATLAB. Images displayed in the figures were cropped and leveled in Adobe Photoshop, and figures were prepared in Adobe Illustrator.

2.2.2 Vertex Intensity Ratio Measurement and Quantification

Intensity measurements of vertices, local interfaces, and local background were automated using the watershed segmentation data to generate ROIs (using distance transforms) that were then used to measure average pixel intensities (Fig. 2.4). Vertex ROIs were generated by making a binary matrix of the vertex pixel and using the distance transform to identify all pixels within 3 pixels of the vertex (forming a pixelated disk 7 pixels in diameter). The local interface and background intensities were measured within a 41-by-41 pixel square centered at the vertex, and local interface and background intensities were used to account for non-uniform illumination and varying junctional protein enrichment. Within the square neighborhood, the interface ROI was acquired using the distance transform to identify all pixels within 3 pixels of the interfaces and removing the vertex ROI. The local background ROI was acquired using a distance transform to identify all pixels at least 7 pixels in distance from the segmentation lines: the 7 pixel value was chosen to create a 3 pixel buffer zone between the interface/vertex ROIs and the background. The intensity ratio for each vertex was calculated as (V-B)/(J-B) where V is the vertex, B is the background, and J is the junction (interface) intensity measurements. Quantification of the intensity ratio was performed by averaging over all vertex time-points during GBE and all embryos or resolved in time.

2.2.3 Vertex Intensity Ratio Variability in Time Measurements

Measurement of the dynamics of protein enrichment at vertices was done by calculating the standard deviation of the intensity ratio over time for each vertex. This was then quantified by averaging over all vertices.

2.2.4 Separation of Vertex Motion and Tangential Component

With respect to the embryo or the imaging field of view, vertices undergo primarily two different components of motion: drift (or translational motion) as the germband elongates, and cell-centric motion such as cell shape changes and intercalation movements. Thus, to analyze the motions associated with cell shape changes and intercalation, the drift component was removed by measuring vertex

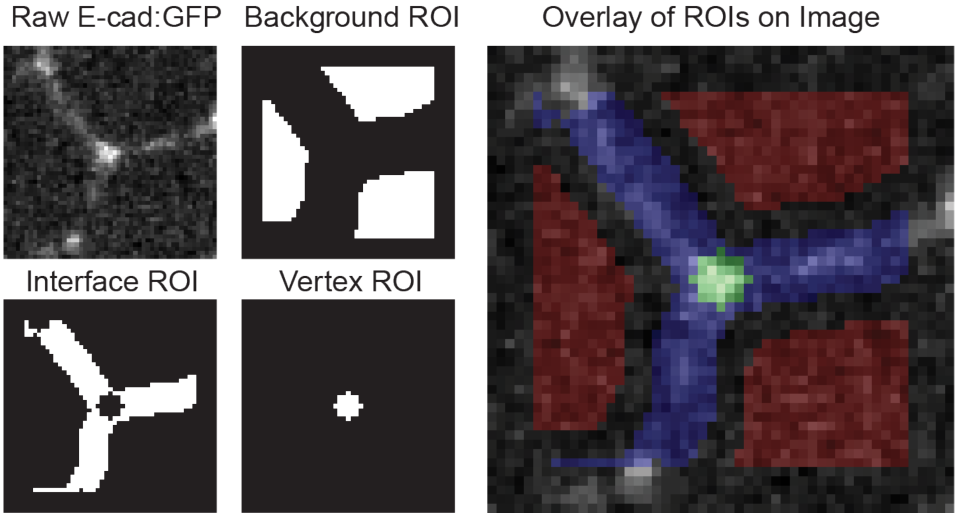

Figure 2.4: Images showing the local regions of interest (ROIs) used to measure average background (top middle), interface (bottom left), and vertex (bottom middle) intensities for the vertex shown (top left, raw image). All three ROIs are color shaded on the raw image (right).

positions with respect to the centroid of the cell, $\vec{c}(t) = [x_c(t), y_c(t)]$, where $x_c(t)$ and $y_c(t)$ are the x- and y-coordinates of the cell centroid at time t. The centroids of each cell were obtained over time using MATLAB's *regionprops* function. In this cell-centric reference frame the position of a vertex is given by $\vec{v}(t) = [x_v(t) - x_c(t), y_v(t) - y_c(t)]$, where $[x_v(t), y_v(t)]$ is the position of the vertex in the image frame of reference. For measuring vertex tangential motion, vertex positions were converted to polar coordinates, $\vec{r}(t) = [r(t), \theta(t)]$, where $r(t)$ is the radial position of the vertex from the centroid of the cell and $\theta(t)$ is the angle. Tangential displacements of the vertex are given by $\Delta s = r \times \Delta\theta$, where, by convention, displacements towards the opposing vertex of the interface were assigned a negative sign. Thus, interface-contracting displacements of an individual vertex are negative and interface-elongating displacements are positive.

2.2.5 Correlating Vertices Coupled Direct Motion

The motion coupling of each vertex with each neighbor vertex within the same cell was quantified via the cross-correlation at zero-lag of the vertices' rate of displacement towards each other. The motions correlated are the components of displacement in the direction parallel to the two vertices, i.e., along the line connecting the pair of vertices. The parallel component is calculated by taking the dot product of the displacement with the average vertex-to-vertex vector before and after displacement, the vertex position trajectories are then computed by taking the cumulative sum of the parallel displacement components. Rates of vertex displacement were calculated over 25 seconds to avoid correlating localization error [70]. Like pairs of vertices were combined in the quantification: 1 vs. 5 includes 2 vs. 4 representing horizontally coupled vertices, 1 vs. 4 includes 2 vs. 5 representing diagonally coupled, etc. The highlighted plot regions were manually selected to show periods in which the vertex is highly active in inward or outward motion. Vertex movements towards or away from each other result in a positive correlation, while a negative correlation value indicates that they move in the same direction.

2.2.6 Vertex Sliding Shown Through Sum of Contracting and Transverse Interfaces

One prediction of vertex sliding is length (i.e. plasma membrane) compensation of the adjacent interfaces, i.e. as a vertex slides one interface gets longer by the same amount that the other gets shorter. To quantify this on time scales of interface contraction, the sum of the contracting interface with both of its transverse interfaces was taken (note: this accounts for the sliding motion of both vertices of an interface) to see if total length was conserved. This sum was performed on all available fully contracting interfaces that had a duration of 5 minutes before contracting to zero length. Individual cases were aligned such that the last time point was T=0 min. Each contracting interface has two pairs of two transverse interfaces, those for cell A and for cell B, and both pairs were counted in the average.

2.2.7 Acquisition of Instantaneous Phase and Amplitude from Cell Area

To get the instantaneous phase (Fig. 2.5) of an oscillating signal such as the area of a cell, a method known as the Osculating Circle Method [28] was used, which is based on the Hilbert Transform but better suited for signals with non-zero mean. To get meaningful results using this method, the signal must be filtered to remove the noise that will result in artificial high frequency oscillations. A Savitzky-Golay filter of polynomial order 3 and frame size 45 seconds (the exact number of frames varied based on the frame rate of the movies) was used because it performed best at removing noise and preserving true cell area oscillations. Before applying the Savitzky-Golay filter, the signal was de-trended by subtracting a long time scale Gaussian filtered (sigma = 180 seconds) version of the signal. Instantaneous phase was shifted such that -180 to 0 degrees represents peak-to-trough and 0 to 180 degrees trough-to-peak. The Osculating Circle Method also gives an instantaneous amplitude which was averaged over time to calculate a cell's average area oscillation amplitude.

Once the instantaneous phase trajectory of a cell's area oscillations is obtained, other time-dependent readouts of the cell dynamics, such as the length of an interface, motion of a vertex, or intensities of a vertex, can be remapped from the time domain to the cell phase domain to average how those parameters change over the course of a cell's oscillation cycle; this averaging is difficult or impossible in the time domain due to variations in oscillation cycle length. Mapping into the phase domain results in a 2D scatter plot of parameter values versus phase values

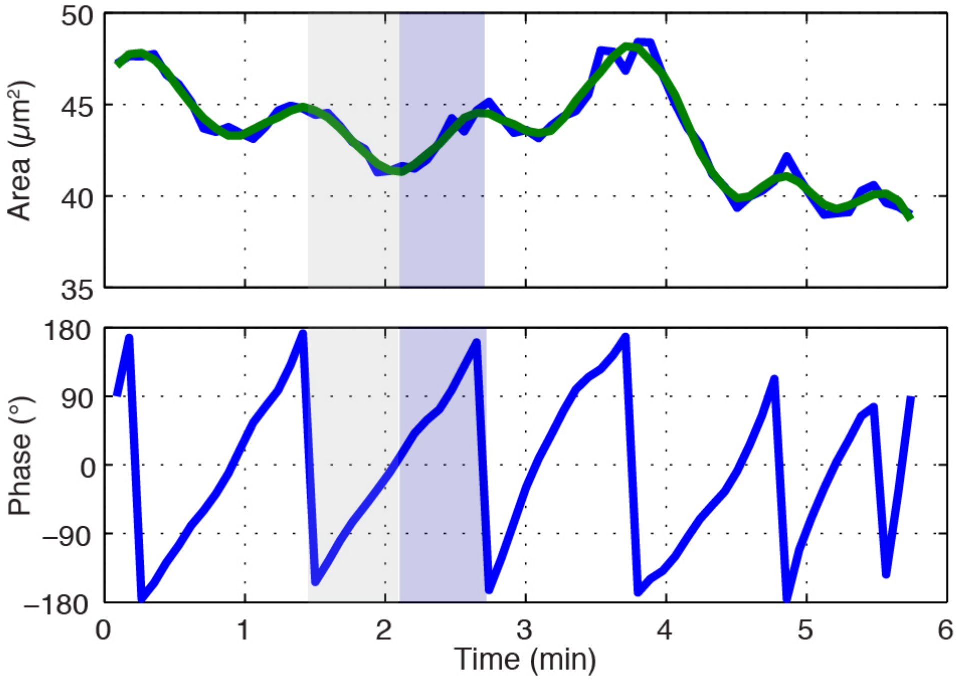

Figure 2.5: The osculating circle is used to obtain instantaneous phase of a signal. (top) Plot of raw cell area trace over time in blue and the filtered signal in green. An oscillatory cycle is highlighted with gray and blue for the decreasing and increasing phases, respectively. (bottom) Phase plot generated from the filtered signal with the same highlighted regions shown.

for multiple cycles of phase; the interpolation was done by Gaussian weighted averaging of the parameter to a grid of phase values.

2.2.8 Interface Length and Fractional Length with Respect to Area Phase

To determine how interface lengths change over the course of an area oscillation cycle the data was mapped into the phase space of the adjacent cells, separately for the phases of cell A and cell B (Fig. 2.6). For each phase cycle the interface length trajectory was shifted, by subtracting the initial length, so that it starts from $L = 0$ with each cycle. This 'reset' to zero with the start of each cycle was done so that positive lengths represent interface growth and negative lengths represent interface contraction with each phase cycle. The 2D set of data points (phases and shifted lengths) for all phase cycles (from both cell A and cell B, for all AP interfaces, and all movies) were combined and interpolated as described above. The quantification, to be shown later in Fig. 3.5C', was done by measuring the average shifted length within two 10° phase bins: one bin centered at 0° to capture the length change after the area decreasing phase and one centered at 175° (170-180°) to capture the average length change after a full cycle. From the values in the bin centered at 175° the average of the 0° bin was subtracted to get the length change over just the area expanding phase. The methods for fractional length are the same as above, except that interface lengths are replaced with the ratio of the interface length divided by cell perimeter.

2.2.9 Contour over Euclidean Area Ratio

Contour cell area is defined as the area within the watershed segmentation lines plus half the area of the pixels that make up the watershed boundary lines (otherwise the contour areas would be artifactually small). The Euclidean area is defined as

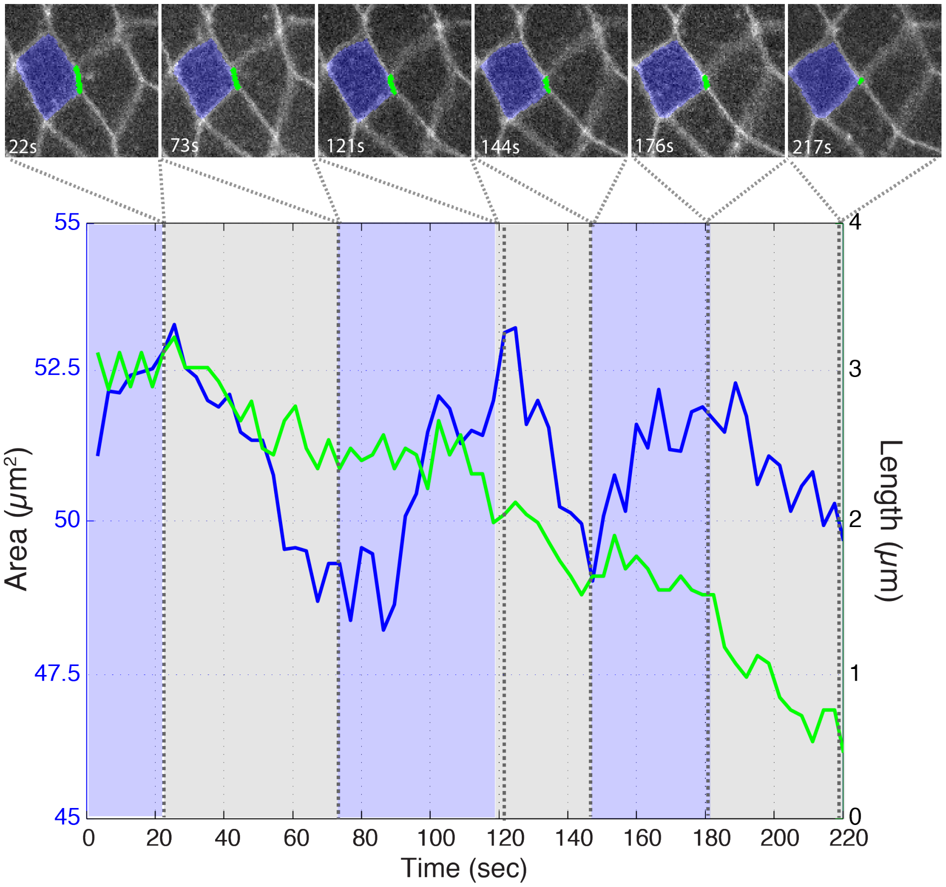

Figure 2.6: Plots of a T1 junction length (green) and cell area (blue) of the junction and cell highlighted in the image panels. In the plot, area contraction phases are highlighted in gray and area expansion phases in blue; dashed lines show the time points the images are from.

the area of the polygon whose vertices are the cell's detected vertices. The contour over Euclidean area ratio (or cell shape metric) is a simple ratio of these two values. When interpolating the cell shape metric to phase space the phase of the Euclidean cell area was used. The quantification shown later in Fig. 3.6B was done on 10° phase bins centered at ±180°, ±90°, and 0°.

2.2.10 Vertex Displacement Rate with Respect to Cell Phase

To see whether individual vertex motion was correlated to cell area oscillation cycles, vertex displacements were tracked with respect to the phases of the three cells that make up the tricellular vertex. The particular type of vertex displacement measured was the cell-tangential component, which is perpendicular to the vector from the cell centroid to the vertex, and therefore independent, to the radial motion associated with cell area oscillations. Cell-tangential displacements were assigned a negative sign if the displacement contracted the vertical interface. For each vertex there are two tangential motion trajectories, one with respect to cell A, and one with respect to cell B, thus the methods described here were performed twice for each vertex, once with respect to each cell. For one vertex motion trajectory the instantaneous phases of cells A, B, and the other cell in the triad (C or D) are collected for each time point in the trajectory. Vertex displacements were interpolated to a 3D grid with the three cell phases on the 3 axes. To account for edge effects of interpolation, data near the edges (±180°) was wrapped around by adding or subtracting 360° to the phases.

2.2.11 Vertex Intensity with Respect to Cell Phase and Vertex Angle

Vertex intensities of Ecad:GFP and mCherry:Sqh were also interpolated into area phase space in a spatial angle resolved manner. Each vertex has an angle with respect to the centroid of each cell it borders, which also varies over time. These angles were measured with respect to a global reference angle, the angle along the dorsal-ventral axis of the embryo towards the ventral. The intensity trajectory of each vertex was normalized (zero mean and s.d. of 1). Normalized intensities were interpolated to a 2D grid of vertex angle and cell phase angle. To account for edge effects of interpolation, data near the edges (±180°) was wrapped around by adding or subtracting 360° to the phases.

2.2.12 Cross-correlation of Intensity Ratios of E-cad and Myosin at Vertices

To quantify the temporal correlation between E-cad and Myosin enrichment at vertices, a cross-correlation of the rates of change of the vertex intensity ratios was performed (Fig. 2.7). Rates of change were calculated over 25 seconds to avoid correlating localization error. Signals were normalized such that mean and standard deviation were 0 and 1, respectively, and an unbiased cross-correlation was computed via MATLAB's *xcorr* function. The temporal lag was estimated by calculating the centroid of the positive peak.

2.2.13 Fly Stocks and Genetics

Stocks were kept at 25° C and maintained by standard procedures. Fly stocks used in this study were E-cad:GFP; Gap43:mCh/TM3 and E-cad:GFP; mCherry:Sqh. All E-cad:GFP was expressed from the endogenous locus on the second chromosome and is homozygous viable.

2.2.14 Live Imaging

Embryos were collected on apple juice agar and dechorionated in 50% bleach for 2 minutes, then rinsed with water and either staged on apple juice agar or

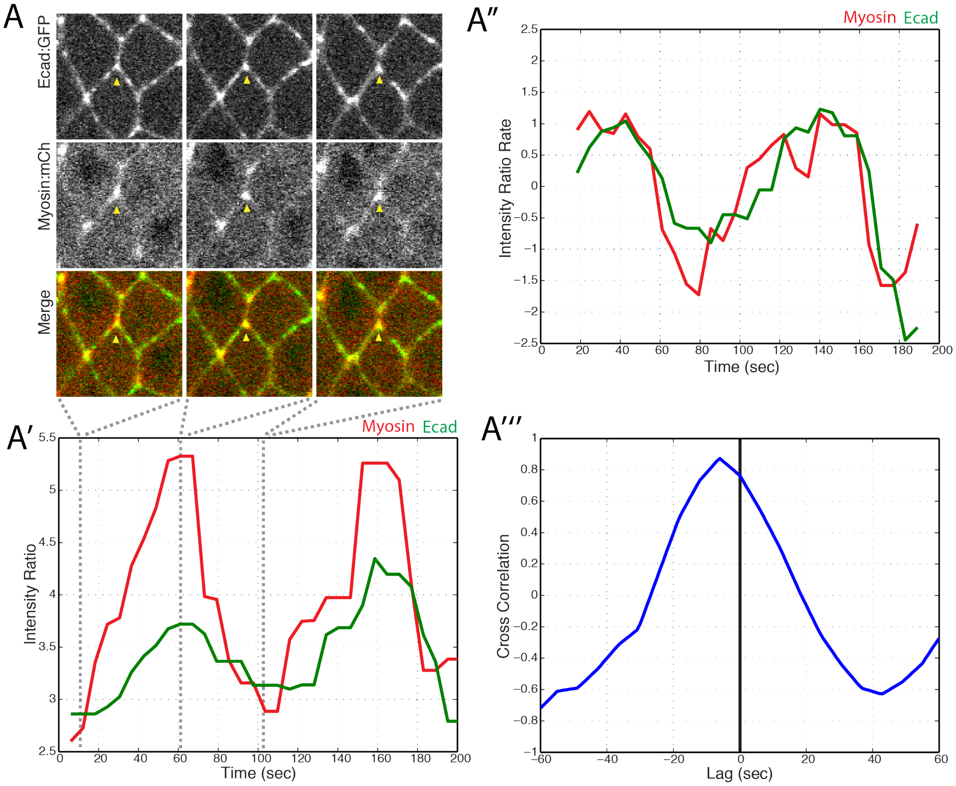

Figure 2.7: Example images and plots showing the process of cross-correlating E-cadherin and Myosin II at vertices. (A) Images at three time points in which enrichment at the vertex (yellow arrowhead) is at a minimum, maximum, and then minimum. (A') Plot of the vertex intensity ratio for both E-cadherin and Myosin (mCh:Sqh), dashed lines indicate time points in (A). (A") Plot of the rate of change of the intensity ratio in (A'). (A"') Cross-correlation of the rates in (A")

transferred to a gas permeable microscope slide and covered with Halocarbon 27 oil. All imaging was performed on a CSU10b Yokogawa spinning disk confocal from Zeiss and Solamere Technologies Group with a 63x/1.4 NA objective, with the exception of Myosin II movies, which were obtained on a CSUX1FW Yokogawa spinning disk confocal from Nikon and Solamere Technologies Group with a 60x/1.4 NA objective. Ecad:GFP; Gap43:mCh images are a summed projection of 5 z-slices taken at 0.5 μm steps starting sub-apically, at 3 seconds/frame. Ecad:GFP; mCh:sqh images are a maximum intensity projection of 8-10 z-slices taken at 0.75 μm steps, at 6 seconds/frame. Imaging was carried out by Celia Smits.

2.2.15 Drug Injections

Following dechorionation as previously described, embryos were staged and aligned on apple juice agar, glued to a coverslip with heptane glue, and desiccated. Embryos were covered with Halocarbon 700 oil then injected with 10mM chlorpromazine, or 25mM or 100mM Y-27632. Embryos at the beginning of GBE were injected in the perivitelline space at 50% egg length. Data was grouped by individual treatment and segmented, analyzed, and reported without masking. Drug Injections were carried out by Celia Smits.

2.3 GBE Along the Apico-Basal Axis and T2-T3 Processes

2.3.1 Alignment to a Common T2 Time Point

To allow averaging over many T1-T2-T3 transitions, associated data (interface lengths, cell areas, and the extension metric) was temporally aligned to the T2 time point, i.e. the transition through the higher-order vertex. Since a cell group will often spend multiple frames in the T2 state, and since there are also reversible

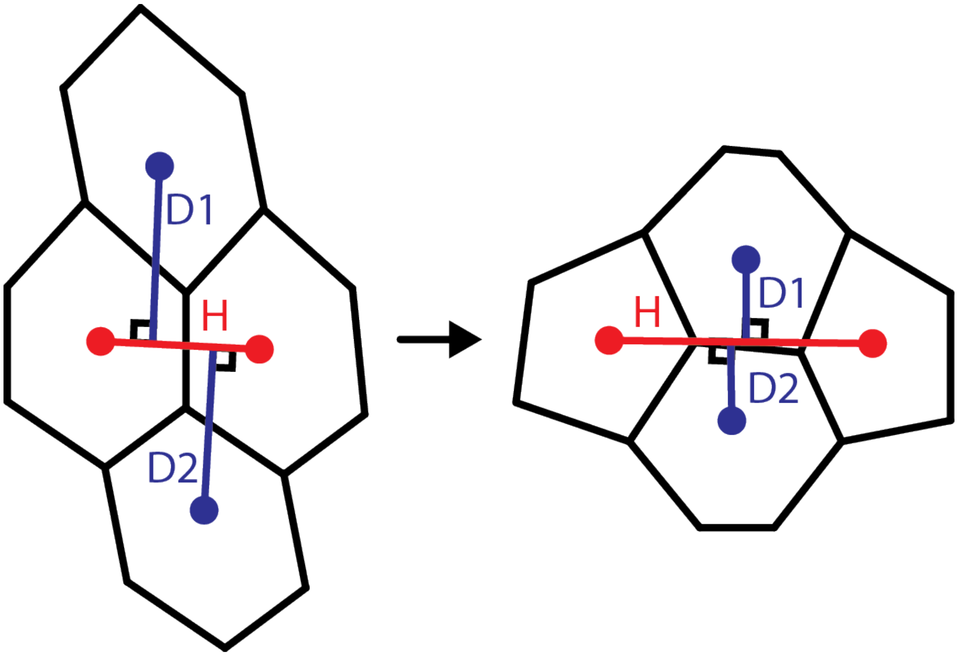

Figure 2.8: Illustration of centroid measurements for extension metric calculation.

transitions between the T1/T2 and between T2/T3 states, the T2 alignment time point was calculated as the average of the time of the last T1 and the first T3 state.

2.3.2 Extension Metric

The extension metric (EM) was based on the four cells involved in a type T1 transition. It is given by $EM = 2H/(D1 + D2)$, where H is the distance between the centroids of the two cells that form the T1 interface, and $D1$ and $D2$ are the are the distances to the centroids of the vertical neighboring cells (which later form the T3 interface) as measured perpendicular from the horizontal line H (Fig. 2.8). The discontinuity in the extension metric (to be shown later in Fig. 3.13C, left panel) at the alignment time is due to the fact that the samples of T1 and T3 interfaces were drawn from different cell groups and areas of the tissue; while interfaces can be found that are visible in the field of view for 15 minutes continuously either just before or just after T2, it is rare to find any that are visible continuously for both.

2.3.3 Leading Layer

The 'leading layer' was defined as the z-layer of shortest length in T1 phase and longest length in T3 phase. For a curved epithelium cell areas will be slightly larger farther from the axis of curvature and thus perimeters and interface lengths will have a depth dependent bias. To account for the size variation of the cells along the apico-basal axis for each time frame the interface length was normalized by the cell perimeter in each z-layer. For the analysis in which apical was distinguished from basolateral, 'apical' corresponds the top segmented apical layer and 'basolateral' to the layers from 3 down to the most basal.

2.4 The Role of Rab35 in GBE

2.4.1 Confocal Microscopy and Time-Lapse Imaging

Confocal images were acquired on an Olympus Fluoview FV1000 confocal laser scanning microscope with 40/1.35 NA or 60/1.42 NA objective for fixed specimens. Time-lapse imaging was performed on a CSU10b Yokogawa spinning disk confocal from Zeiss and Solamere Technologies Group with 63/1.4 NA objective. Embryos were imaged after dechorionation and placement on a gas-permeable membrane in Halocarbon 27 oil. Live imaging was performed using exposure settings of 100-350 ms and images were acquired every 1 s. Imaging was performed by Cayla E. Jewett.

2.4.2 Fitting Mean Squared Displacement Curves

The mean squared displacement (MSD) is defined as $MSD(\tau) = \frac{1}{N-n}\sum_{k=1}^{N-n}[l((k+n)\delta t) - l(k\delta t))]^2$, where the time lag is $\tau = n \cdot \delta t$, n is the number of frames for the time shift, δt is the time between frames, and N is the total number of available time points for the length trajectories l. MSD curves were fit to the function $MSD(\tau) = A(1 - exp(-\alpha\tau)) + 2B\tau + C^2\tau^2$, where the first term represents the constrained component with amplitude A and positive time constant α, the second term is the diffusive term with diffusion coefficient B, and the third term the active component with C representing the velocity. The data was fit to this function using a least squares fitting method.

2.4.3 Step Detection

To detect active motion steps in vertex position trajectories a rolling analysis window technique adapted from Huet et al. was used. The MSD is the customary method to classify a sub-trajectory into active, diffusive, or constrained motions based on whether the MSD curves upward, is linear, or curves downward, respectively. For periods of active motion the MSD behaves as a power law $MSD(\tau) \propto \tau^{\gamma}$ where $\gamma > 1$. By calculating the parameter gamma along a trajectory using a rolling window periods of active and inactive (i.e., either diffusive or constrained) motion can be detected. For each window the MSD was fit to lags between 5 and $3(N-1)/4$, where N is the odd-numbered number of points in the window. The first 4 lags were left out of the fitting because localization error leads to artifactual subdiffusion at this short time scale lowering the value of γ. To reduce computation time we performed linear fitting of the MSD verses τ on a log-log plot. Prior to step detection, trajectories were filtered with a 5th-order median filter using the *medfilt1* function in Matlab to remove noise.

One of the challenges of a rolling analysis window is in selecting the size of the window. A window too large makes detecting brief steps unlikely, whereas a window too short performs worse at detecting longer steps. Thus, a rolling window with variable widths optimized for the steps in the trajectories was used. For a given position of the window, which is defined by its center position, γ is calculated for a range of windows from W_{min} to W_{max} (the windows 21, 41, 61, and 81 frames were used) and the maximum value of γ is retained, corresponding to maximum

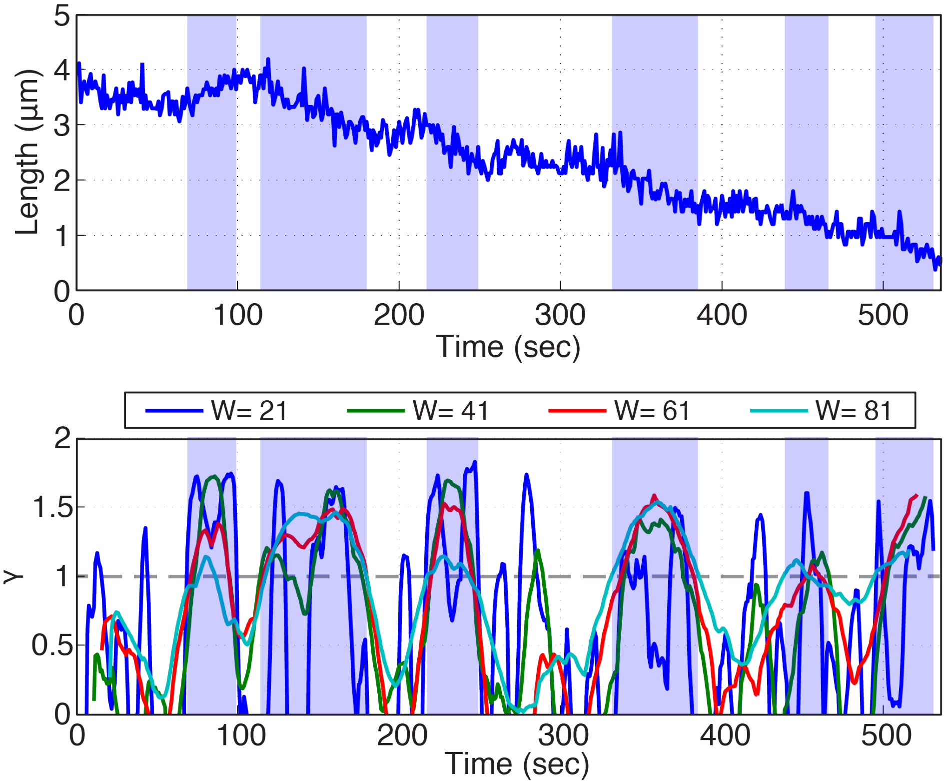

Figure 2.9: Example showing steps detected in the length of a contracting cell-cell junction (top). Gamma (γ; bottom) is calculated for various sliding window sizes (W=21, 41, 61, and 81) and periods where the maximum γ exceed 1 are counted as steps. Step periods 14 seconds or shorter are considered too short for detection and are excluded.

likelihood of systematic motion (Fig. 2.9). This is repeated for each time point along the trajectory to give γ as a function of time. The determination of systematic from non-systematic periods is made by setting a threshold on $\gamma(t)$ of 1. A minimum duration requirement of 14 frames (14 seconds) was applied because it was found that positive detections below that duration did not represent real active periods.

2.4.4 Fraction of Negative Followed by Positive Steps

The fraction of negative followed by positive steps (or FNFPS) is a measure of how many step reversals occur within a cells time course. It is the ratio of the number of times a contraction (negative) step is immediately followed by an expansion (positive) step to the total number of contraction steps. The FNFPS can take values between 0 and 1, 0 if every step of a cell is a contraction, and 1 if every contraction is followed by an expansion.

2.4.5 Neighbor Number Distributions

Cell neighbor numbers were calculated as the sum of cell-cell interfaces. Cells that touched the background (i.e., the edge of the segmented region) were excluded because their total neighbor number was unknown. For each frame the fraction of cells of each neighbor number was computed. Only the fractions of cells with 4, 5, 6, 7, and 8 sides were plotted. Cells with 3 sides or more than 8 did occur on rare occasions in the movies but generally did not exceed 5% in number so their traces were excluded. The traces were Gaussian-smoothed using a sigma of 5 seconds.

2.4.6 Amplitude of Cell Area Oscillations.

To measure the amplitude of cell area oscillations a method based on the Hilbert transform [28] was used that outputs the instantaneous amplitude, frequency, and phase information of a signal given that the noise-associated oscillations have been filtered out. Cell area trajectories were filtered using a Savitzky-Golay filter of polynomial order 3 and frame size 81 (Matlab function *sgolayfilt*). Cell area signals were detrended by subtracting a long-timescale Gaussian filtered ($\sigma = 200$ seconds) version of itself. This long-timescale filtered signal served as the local average area, which was used to compute the amplitude as a percentage of the cell area at each instant. For each cell, the instantaneous amplitude percentage was averaged over its entire time course.

2.4.7 Ventral Furrow Cell Area Analysis

For the cell area verses time plot (to be shown later in Fig. 3.20C) each cell's area trajectory was normalized such that at $t = 0$ the area was 100% and then took the average and standard error over all cells. For the rate of area change bar graph (to be shown later in Fig. 3.20D), for each cell we took the difference between the final and initial area over the full time period (6.6 min) divided by the time period and then took the average and standard error over all cells.

Chapter 3

Results

3.1 Uncoupled Vertex Sliding

3.1.1 E-cadherin is Dynamic and Enriched at Tricellular Vertices

To study in more detail how cell topologies are remodeled, the localization of endogenously tagged E-cadherin (E-cad:GFP) at the onset of intercalation was looked at. Strikingly, and in contrast to the previously reported homogenous distribution of E-cadherin along DV interfaces at mid-GBE [5], E-cadherin was highly enriched at vertices (Fig. 3.1A-C). This strong vertex-association of E-cadherin began at the onset of GBE, with E-cadherin diffusely present at apical cell interfaces prior to intercalation (Fig. 3.1D-D'). Systematic quantification of vertex-associated E-cadherin averaged across the entire time of GBE (see Methods section 2.2.2) also revealed that E-cadherin maintains a higher vertex:interface ratio than does a control, plasma membrane-associated marker (Gap43:mCh; Fig. 3.1B-C). Interestingly, although E-cadherin is enriched at vertices, it possesses a much wider distribution of intensities than the control marker, which suggested that vertex associated E-cadherin might undergo cycles of enrichment and dispersion (Fig. 3.1C). Analysis of vertex E-cadherin confirmed that the intensity of enrichment fluctuates in time (Fig. 3.2A-B). These results show that the vertex-specific localization of E-cadherin temporally coincides with intercalary movements, and suggest that vertex E-cadherin may function in directing GBE.

3.1.2 Movement of Cell Vertices is Physically Coupled in the Radial Direction

A central physical expectation from previously described line-tension models [19, 49] is that the inward movement of vertices connected by a contracting interface should show evidence of mechanical coupling (Fig. 3.3A). However, no evidence of this hypothesized coupling was observed (Fig. 3.3B and C). Indeed, in systematic pair-wise analyses of cell vertices, physical coupling could only be observed in radial directions (e.g., between vertices 3 and 6; Fig. 3.3B',C). In other words, an inward correlation of vertex motion was only found between vertex pairs on opposite sides of the cell, with the largest correlations between those diametrically opposed (Fig. 3.3C). These results indicate that during the contraction of an AP interface, the motion of the two vertices toward the middle of the interface (referred to as 'productive' motion) occurs independently of each other, while all vertices undergo coupled motion into the radial direction. These results argue against a line tension-driven model of interface contraction, and suggest that intercalary movements should be reconsidered in terms of cell vertices and radially exerted forces.

3.1.3 Vertices Slide Independently of One Another

Through the analysis of vertex steps in vivo, a novel behavior began to emerge: cell vertices associated with contracting interfaces often underwent periods of productive sliding along the plasma membrane (Fig. 3.4A). This suggested that the uncoupled motion of T1 vertices is due to vertex sliding, a previously

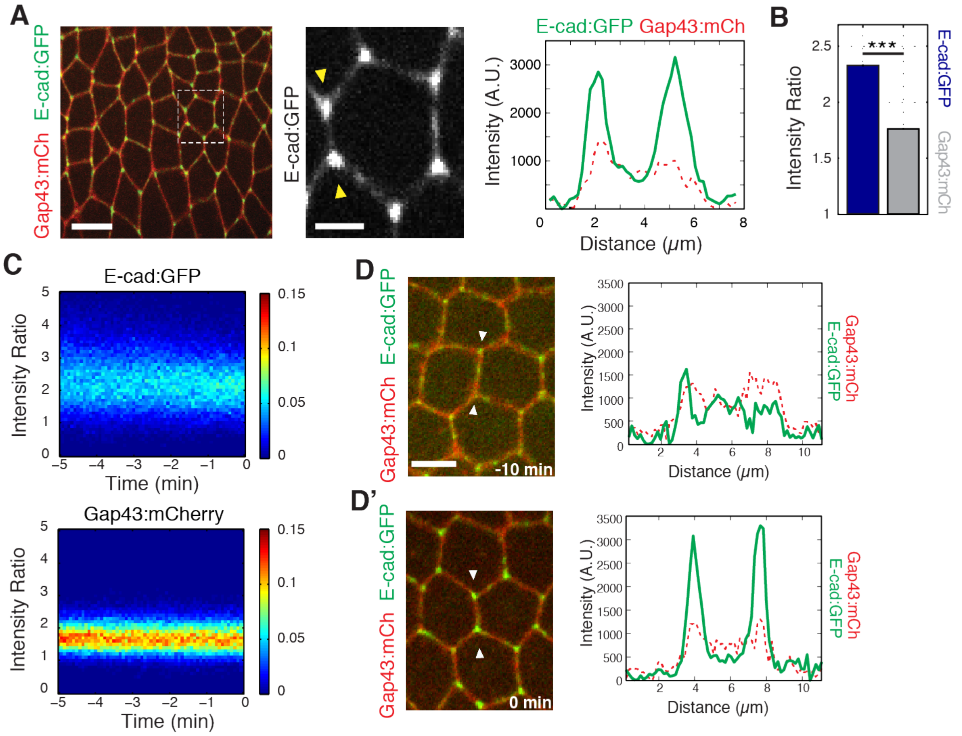

Figure 3.1: Vertex enrichment of E-cadherin at the initiation of GBE. Endogenous locus E-cad:GFP (green) and plasma membrane marker (Gap43:mCh, red). Single pixel intensity line plot (right) for both E-cad:GFP and Gap43:mCh from region between the yellow arrow heads (middle panel). (B) Vertex:interface intensity ratios computed for each vertex and frame (n = 87662 vertex time points). (C) Heat maps showing the distribution of vertex intensity ratios of Ecad:GFP (left) and Gap43:mCh (right) as a function of time over all embryos aligned to their most contracted state. Color bar shows relative frequency. (D-D') T1 configuration of cells expressing E-cad:GFP and membrane marker (Gap43:mCh) imaged 10 min before start of GBE (D) and at the onset of intercalation (D'). Intensity line plot corresponds to the single pixel intensity line drawn between the two arrowheads in the left panel. Scale bars are 10 mm (A, left), 3 mm (A, middle), and 5 mm (D). The data are from five embryos and represent mean ± s.e.m. Statistical tests were done by Student's t-test. *** denotes p<0.0001.

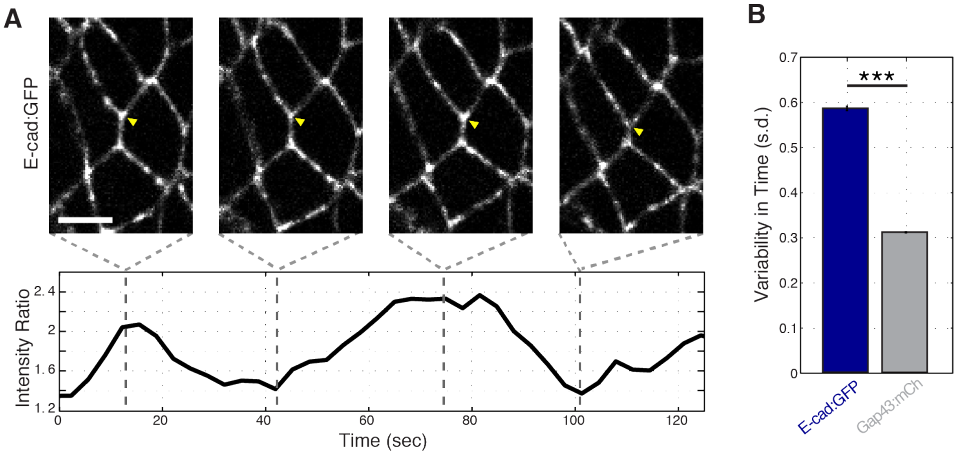

Figure 3.2: (A) Oscillations in E-cad intensity at an individual T1-associated vertex (yellow arrowhead). Scale bar is 5mm. The intensity ratio is plotted over time (bottom).(B) Vertex-associated E-cad intensities display greater variation than control Gap43:mCh membrane marker. Standard deviation over time for a given vertex's intensity ratio averaged (n = 3188 vertex trajectories). The data are from five embryos and represent mean ± s.e.m. Statistical tests were done by Student's t-test. *** denotes $p<0.0001$.

uncharacterized form of cell-shape deformation. Measurement of interface lengths showed that as a vertical interface contracts (Fig. 3.4A-A'; blue) the interface adjacent to it elongates (Fig. 3.4A-A'; red), and consequently the total length stays constant (Fig. 3.4A-A'; black). This compensatory increase in adjacent interface length is contrary to what would be expected through canonical models of interface contraction, in which the contracting interface shortens while adjacent interfaces maintain a constant length. Additionally, analysis of the lengths of all contracting and adjacent interfaces throughout GBE demonstrated that this behavior is a systematic component of T1-associated vertex movements (Fig. 3.4C). Also instances were observed where vertices take turns sliding over the course of a T1 contraction (Fig. 3.4B-B'). These results are consistent with the uncoupled movement of vertices, and provide a mechanism by which a single vertex can independently produce the changes in cell shape that drive cell intercalation.

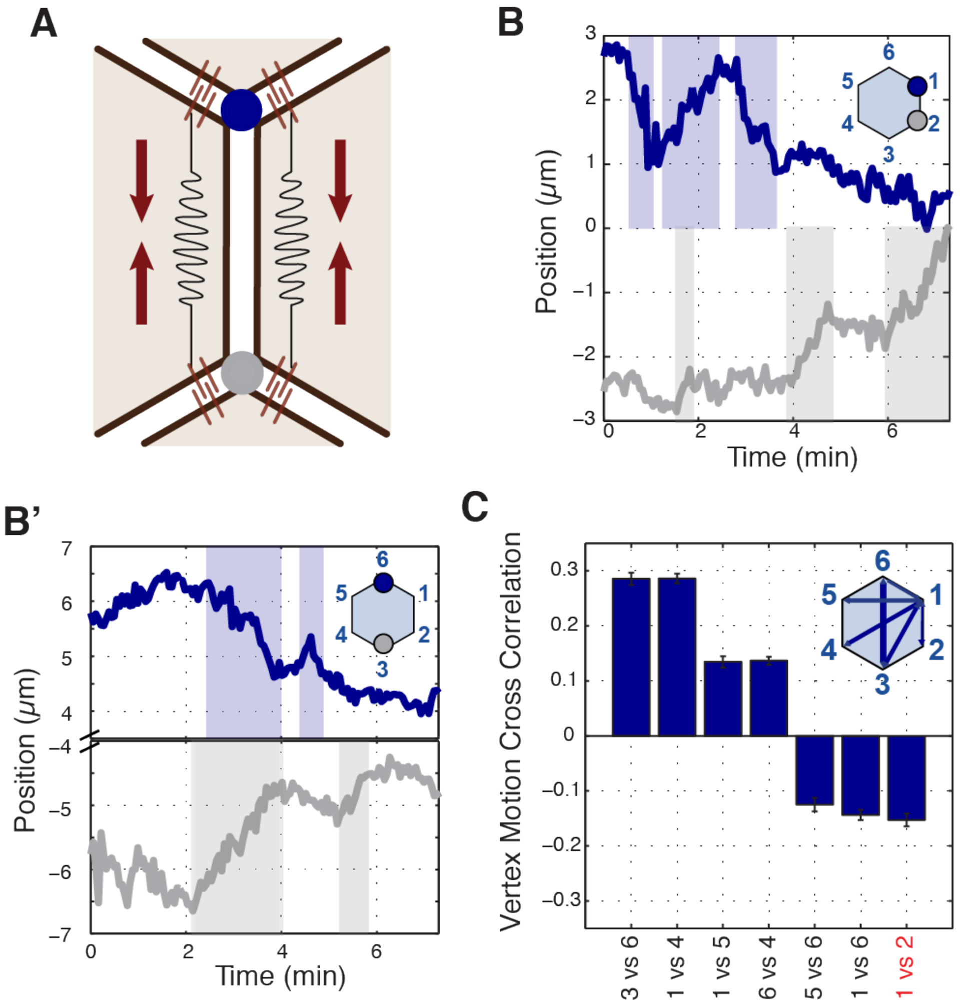

Figure 3.3: (A) Schematic showing line tension model, in which tensioned springs pull across interface lengths on either side of a contracting interface. Blue and gray dots indicate tricellular vertices. (B) Vertices at either end of a T1 interface display uncoordinated movements and a lack of physical coupling. Vertex displacement plotted over time. (B') Radial coupling of cell vertices. Vertices that are radially opposed display coordinated movements and coupling of physical displacements. Shaded regions were manually drawn to point out active motion. (C) Quantification of cross-correlation between vertex pairs (n = 385, 772, 769, 1551, 716, 824, 436 for vertex pair categories from left to right, data from first 20 min of cell intercalation when T1 behaviors occur). $p<0.0001$ for all vertex pairs. Mean ± s.e.m is shown and one sample Student's t-test was performed with hypothesized mean of 0.

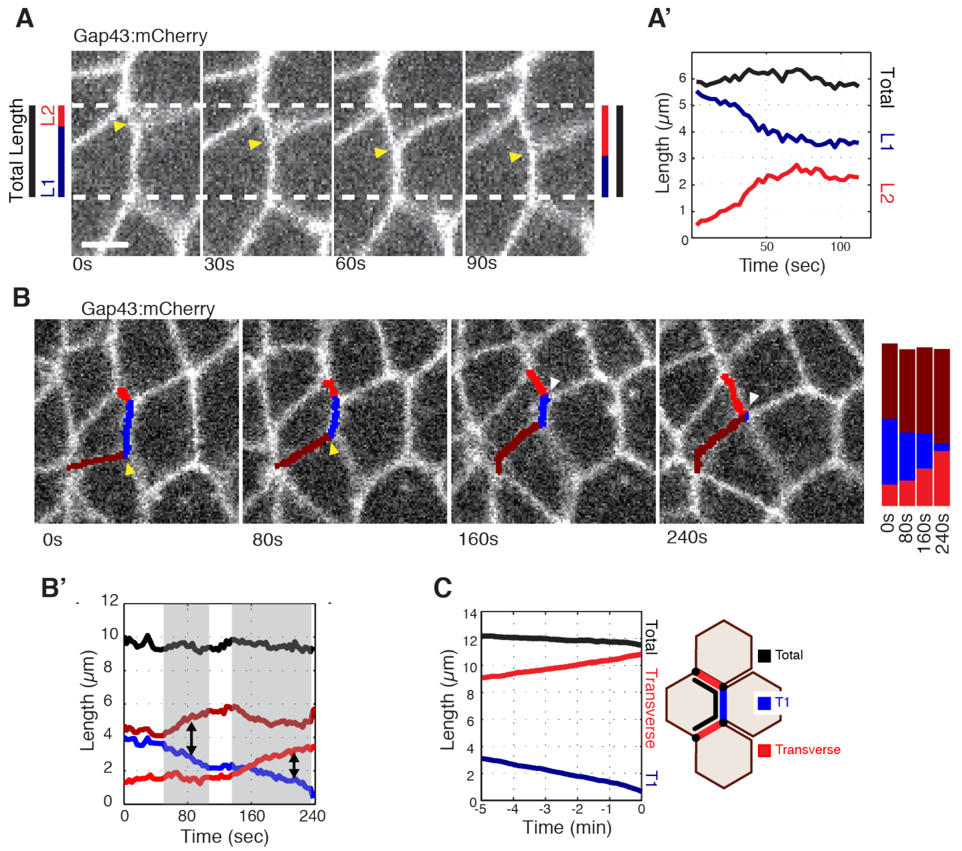

Figure 3.4: (A) Total interface lengths (black bar) are conserved during a vertex sliding event, while the contracting L1 interface shrinks (blue). The associated L2 interface (red bar) has a compensatory increase in length as the AP interface contracts (L1, blue bar). Yellow arrowhead shows sliding vertex, white dashed lines mark total length. Scale bar is 5 mm. (A') Total, L1, and L2 lengths plotted over time. (B) Time series shows a fully contracting T1 interface (blue), and top (red) and bottom (maroon) transverse junctions lengthening over time. The bottom vertex slides first (yellow arrowhead) followed by the top vertex (white arrowhead). (B') Plot of the interface lengths (same colors in B) and the sum of the three lengths in black; grey shading and black arrowheads point to sliding events. (C) Systematic measurement of all fully contracting interface lengths (n = 168 triplet interfaces). Contracting interfaces are aligned and averaged such that their last time point is set to t = 0 (blue curve). The summed lengths of both associated transverse junctions is in red, and the total summed lengths of all three junctions is in black. The data are from five embryos.

3.1.4 Interface Contraction Occurs During Periods of Cell Area Contraction

Since the data demonstrated that the motion of vertices is coupled radially, this raised the question as to what forces could drive this movement. Previous research has shown that an apical actomyosin network drives area oscillations during GBE ([49, 20] ,Fig. 3.5A and A'). This appears to be a common feature of many cell shaping processes, as similar apical area oscillations occur in the invagination of the *Drosophila* ventral furrow [43, 53], neuroblast ingression [57, 2], and the internalization of the C. elegans endodermal precursor cells [53]. To study the dynamics of cell vertices and interface lengths in terms of these radially oriented oscillations, a computational assay was developed to identify the instantaneous phase of cell area oscillations. This allowed the interpolation of vertex motion and interface length changes in this area phase space for large numbers of cell oscillations (see Methods section 2.2.7). This instantaneous phase data follows a coordinate system where area contraction corresponds to angles from -180 to 0 degrees (Fig. 3.5B and B'; gray shading), while area expansion occurs in the period from 0 to +180 degrees (Fig. 3.5B and B'; blue shading).

Using this method, systematic changes in interface lengths during apical area oscillations were measured. Under isotropic conditions, the expected theoretical behavior would be that interface lengths would oscillate along with oscillations in cell area (Fig. 3.5C and C'; black). However, an intriguing behavior is observed when empirical interface lengths are plotted against cell phase. A larger than isotropic decrease in vertical interface length during area contraction was observed (Fig. 3.5C and C'; blue; see Methods Fig. 2.6 for an individual example). Notably, this decrease is preserved even as area contractions are reversed. Conversely, transverse interfaces undergo a smaller than isotropic decrease in interface length, and appear to undergo a compensatory increase in interface length during area expansion (Fig. 3.5C and

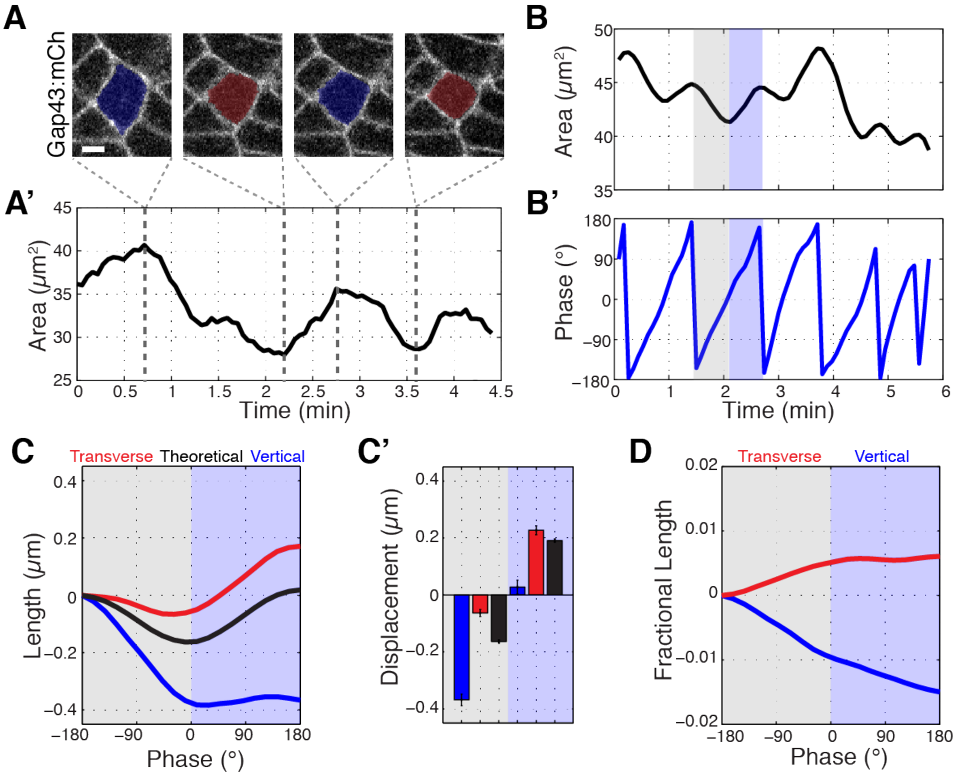

Figure 3.5: Intercalary cell undergoing apical area oscillations colored blue for maxima and red for minima (A) and plot of the area over time (A'). Gray dashed lines indicate image time points. (B) Plot of cell area trace over time. An oscillatory cycle is highlighted with gray and blue for the decreasing and increasing phases, respectively. (B') Phasic plot of the cell in (B) with the same highlighted regions shown. (C) Vertical (blue), transverse (red), and theoretical (black) interface length change interpolated into phase space of the associated cell's area oscillations, n = 212 vertical interfaces. (C') Quantification of the total length change per decreasing (gray side) and increasing (blue side) half-cycles. (D) Fractional length (Length/Perimeter) change for the same interfaces as analyzed in (C, C'). Vertical interfaces show contraction in fractional length, while transverse interfaces possess compensatory increases in cell length, consistent with vertex sliding. Scale bars are 3 mm (A) and data are from five embryos. The data shown in (C') represent mean ± s.e.m. (F) One sample Student's t-test was performed with hypothesized mean of 1. * denotes $p<0.01$.

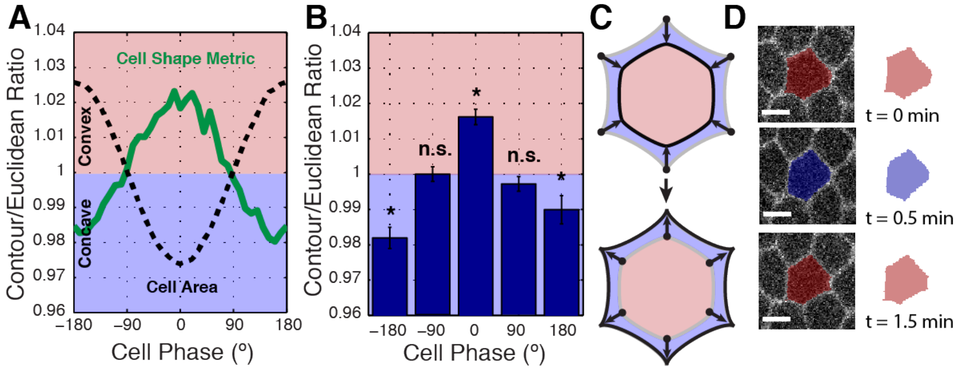

Figure 3.6: (A) Mean contour over Euclidean cell area ratio (or cell shape metric) verses cell area phase (green curve) and cell area (for reference, black dashed curve), n = 304 cells and 5 embryos. (B) Quantification of the cell shape metric at specific phase bins. (C) Illustration showing that cells at area maxima are more concave, while cells at area minima bulge outwards. (D) Sample raw (left) and cartoon (right) cell during one area oscillation. Scale bars are 5 mm. The data shown in (B) represent mean ± s.e.m. (B) One sample Student's t-test was performed with hypothesized mean of 1. * denotes $p<0.01$.

C'; red). To account for the fact that area contraction and expansion generally are associated with decreases and increases in cell perimeter, the effective length changes were also plotted, or fractional length (defined as interface length divided by cell perimeter), of vertical and transverse interfaces (Fig. 3.5D). The fractional length metric has the advantage that isotropic area changes do not result in changes of total fractional length. These results show that about 64% of the effective length contraction of vertical interfaces occurs during area contraction, while only 36% occurs during area expansion when absolute length is stabilized (Fig. 3.5D). Thus, vertex sliding occurs opportunistically during area contraction phases in a ratchet-like fashion, so that shortened vertical interface lengths are stabilized during area expansion.

The phasic analysis was also used to examine cell contours during periods when cells are actively contracting in cell area as compared to periods when cells are expanding (Fig. 3.6A and B). A convexity/concavity cell shape metric was generated by comparing the area ratio between a theoretical straight-line Euclidean geometry that connects cell vertices to the experimentally defined cell contours. Interestingly, cells possess concave cell contours during contraction, and convex boundaries during apical area expansion (Fig. 3.6A-D). These results are consistent with cell vertices, but not cell interfaces, leading overall changes in cell shape and again suggest that cell vertices are key structures that govern cell topologies.

3.1.5 E-cadherin Intensities are in Phase with Area Oscillations and Peak with Vertex Stabilization

As cell areas contracted, instances were observed where E-cadherin became distinctly more enriched at specific vertices (Fig. 3.7A, yellow arrowhead). In these instances, the associated T1 interface length decrease observed during area contraction was stabilized during subsequent area expansion. In contrast, other vertices had very little E-cadherin enrichment, and the interface length change of these vertices scaled with area oscillations (Fig. 3.7A, white arrowhead). A cross-correlation function relating E-cadherin intensity and cell area showed that as areas decreased, vertex-associated E-cadherin intensity systematically increased (Fig. 3.7B). Interestingly, this cross-correlation also showed that vertex E-cadherin intensity peaks just before cell area is in its most contracted state and before the onset of area expansion (Fig. 3.7B). Together, this phase relationship suggests that E-cadherin intensity is coordinated with cell area oscillations, and that enrichment of E-cadherin acts to stabilize sliding vertices. These results further indicate a model in which area oscillations provide the force for intercalation, with E-cadherin dynamics functioning as a molecular ratchet to harness vertex-sliding into productive movement.

If oscillations in E-cadherin enrichments are essential to vertex movements and sliding, one might hypothesize that artificially stabilizing and/or increasing

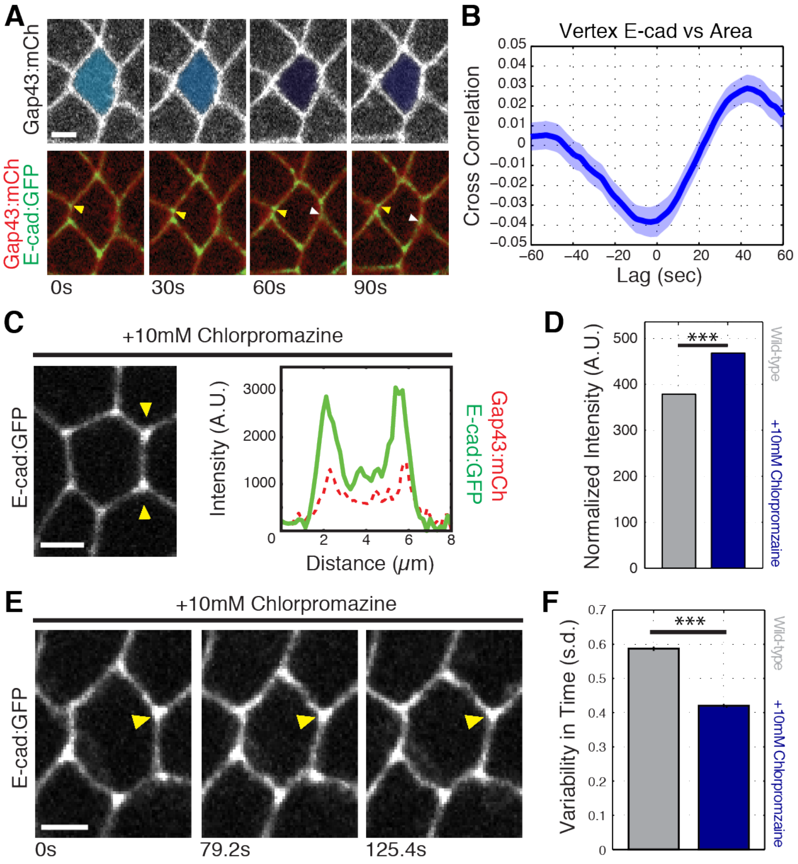

Figure 3.7: Example of a cell contracting in area while vertical interfaces contract. Top: Gap43:mCh (plasma membrane) channel with cell color-coded such that darker blue represents smaller apical area. Bottom: yellow arrowhead points to vertex E-cad:GFP that increases as the area contracts and interface length is stabilized at shortened length. White arrowhead shows vertex with less E-cad, where interface length increases during expansion phase following contraction. (B) Cross-correlation of vertex E-cad intensity and cell area rates of change (n = 610 cells). (C) Stabilization of E-cadherin by chlorpromazine injection. Single pixel intensity line plot between the yellow arrowheads shows vertices maintain enrichment of E-cad. (D) Quantification of normalized vertex intensities in control and chlorpromazine-injected embryos for E-cad:GFP (blue) and Gap43: mCh (red) over all vertices and time points in the last 5 min before the most contracted state (control: 87662 vertex time points; chlorpromazine: 60935 vertex time points. (E) Time series of chlorpromazine-injected E-cad:GFP embryo shows vertex (yellow arrowhead) that does not fluctuate in intensity. (F) Averaged standard deviation over time for each vertex's intensity ratio (n = 3188 control and n = 1934 chlorpromazine vertex trajectories). Scale bars are 3 mm. The data shown in (B, D, F,) represent mean ± s.e.m. Statistical tests were done by Student's t-test. *** denotes $p<0.0001$.

E-cadherin at the plasma membrane should disrupt vertex displacement. To test this, endocytosis was inhibited by injecting embryos with a small-molecule inhibitor, chlorpromazine [41]. This increased the total amount of E-cadherin at cell vertices and interfaces compared to control embryos; additionally, cells maintained a vertex-associated enrichment of E-cadherin throughout GBE (Fig. 3.7C and D). Importantly, endocytic inhibition prevented E-cadherin from oscillating to a lower enrichment state (Fig. 3.7E and F). Although E-cadherin dynamics were disrupted, oscillations in cell areas still occurred. However, under these conditions there was virtually no difference between the theoretical isotropic length change and the observed length changes for either vertical or transverse interfaces (Fig. 3.8). To account for the possibility that vertex sliding is reduced due to other effects of endocytic inhibition, measurements were also made of length changes in E-cadherin overexpressing embryos and found that length ratcheting is also reduced. Vertices in Ubiquitin-E-cadherin:GFP overexpressing embryos had displacements that were reduced by 41% as compared to control embryos (data not shown). Thus, stabilizing E-cadherin prevents vertex sliding and uncouples the ratcheted motion of individual vertices from the motive oscillations in cell area. This further suggests that increased E-cadherin levels restrict vertex sliding, and supports a model in which E-cadherin enrichment at the end of an apical area oscillation serves as a ratchet that stabilizes vertices post-sliding.

3.1.6 Cell-specific Phase Anisotropy Drives Vertex Displacements

Since vertices receive molecular and mechanical inputs from three different cells (Fig. 3.9B), new approaches to study vertex motion with respect to the phases of all three involved cells were needed. To do so, the displacement of a given vertex was decomposed into two independent components: one tangential and one radial to the cell center (Fig. 3.9A', cyan and blue lines, respectively). Since radial

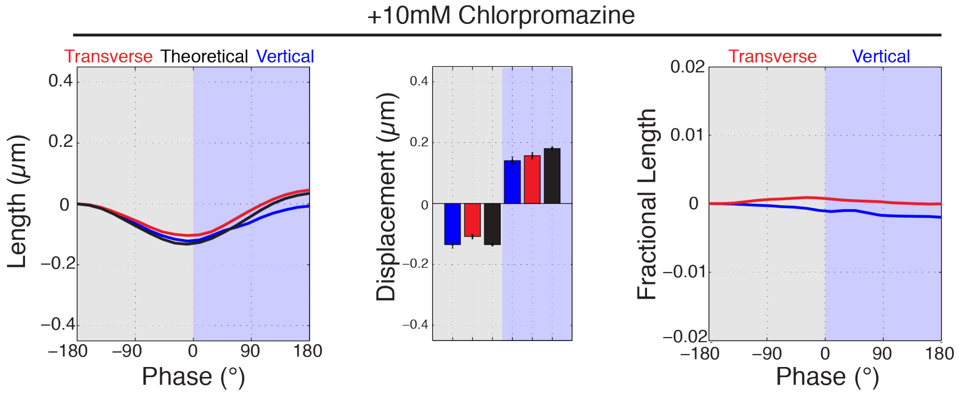

Figure 3.8: Length analyses for chlorpromazine injected embryos (n = 219 vertical junctions). Data are from five embryos (control) and three embryos (chlorpromazine) and the first 20 min of cell intercalation. Scale bars are 3 mm. The data shown in represent mean ± s.e.m.

displacement would be expected from isotropic area contraction, productive sliding displacements were defined as cell-tangential motions (Fig. 3.9A', cyan). This was then plotted against the phases of each cell that share a common vertex, permitting the measurement of the relative contribution of each cell to productive vertex motion. When tangential displacement rates were plotted with the phases of cells A and B (the two AP neighboring cells at a T1 interface, Fig. 3.9C'), productive displacements occurred when both cells were contracting (Fig. 3.9C, C', E and E'). However, when the phases of cells A and C were examined, productive displacements were the strongest during the coordinated expansion of cell C with the contraction of cell A (Fig. 3.9D, D', E, and E'). Strikingly, the magnitude of displacement was much greater in this latter condition than in the first condition (Fig. 3.9E and E'). This demonstrates that the phase of cell C is more predictive of productive vertex sliding events than cells A or B, and provides a mechanism for how anisotropic, radial force balance between three cells sharing a common vertex could couple individual T1-associated vertex steps to cell area oscillations.

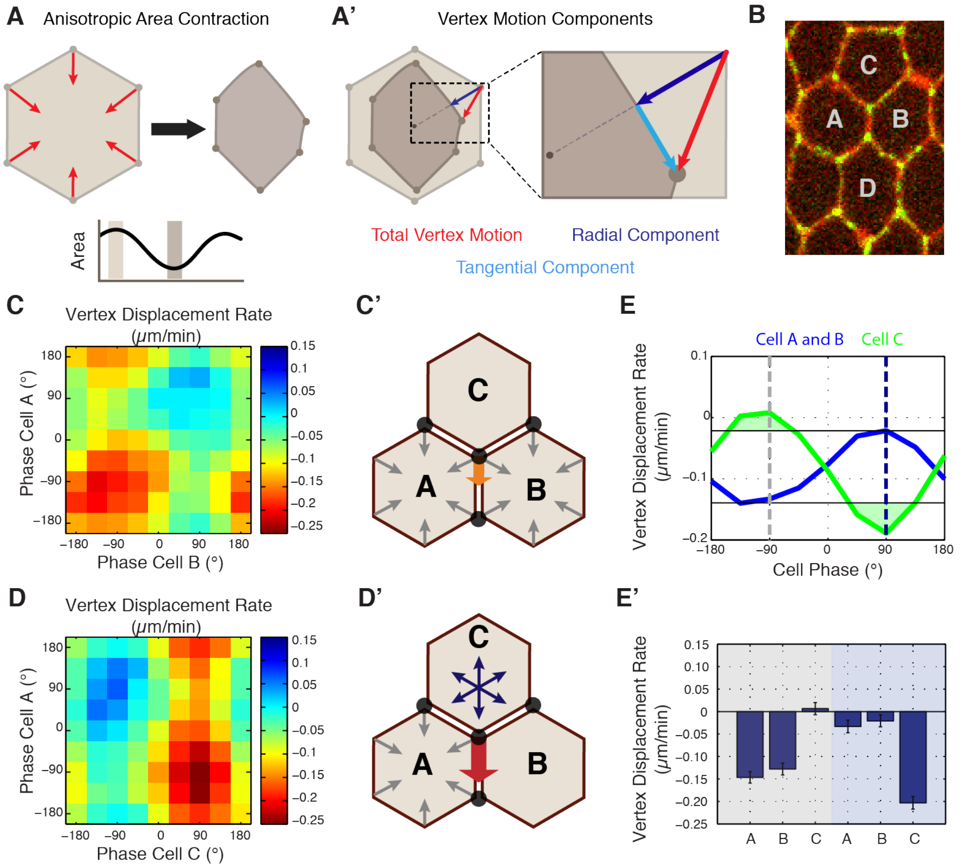

Figure 3.9: (A) Illustration of cell undergoing anisotropic apical area contraction. Red arrows represent inward contractile force. (A') Illustration of vertex displacement (red arrow) broken into tangential (cyan) and radial (dark blue) motion. (B) Cell labeling scheme: cells A and B share a common vertical, T1 junction, while cells C and D are to the top and bottom of T1-associated vertices, respectively. (C, D) Heat map of the tangential vertex displacement rate with respect to the area phases of cells A and B (C) and cells A and C (D), (n = 171 T1 interfaces from five embryos). (C', D') Model schematics showing net displacement of a vertex (orange arrow) when cells A and B are contracting in phase (C'), and a greater net displacement if A and C are in opposite phases with A contracting and C relaxing (D'). (E) Plot of the average rate of tangential vertex displacement for cells A and B (blue) and cell C (green), the black horizontal lines show the max and min levels of cells A and B. (E') Quantitation of vertex displacement rates at peak contraction and peak expansion (phases ± 90 degrees). Gray and blue shading corresponds to gray and blue dashed lines in (E).

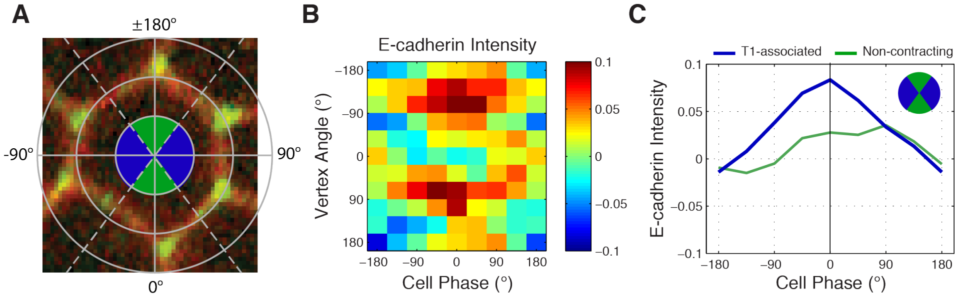

Figure 3.10: E-cadherin is recruited to T1-associated vertices in a phase dependent manner. (A) Illustration of vertex angle assignment used in (B, C). Ventral direction is assigned as angle zero. Dashed lines separate regions associated with T1 vertices (blue) and non-contracting vertices (green) angle categories. (B) Heat map of the normalized E-cad:GFP intensity of vertices with respect to the angle of the vertex and the cell area phase (n = 238 cells from three embryos). (C) Plot of average normalized E-cad:GFP intensity for T1-associated and non-contracting vertices with respect to area phase.

In light of this phase-correlated mechanical anisotropy, the question arose as to whether the molecular properties of vertices also displayed symmetry-breaking differences between AP and DV interface-associated vertices. To address this question, E-cadherin intensities with respect to both area phase and vertex position were examined (Fig. 3.10A). As before, there was strong increase in E-cadherin intensity as cell areas contracted (Fig. 3.10B). Interestingly, this correlation was observed specifically in vertices with polar angles near 90 degrees, corresponding to vertices associated with T1 interfaces (Fig. 3.10B and C). Indeed, only contractile, T1-associated vertices show the maximal intensity increases that peak at the end of area contractions, while DV-associated vertices experienced reduced E-cadherin recruitment (Fig. 3.10B and C). Stabilizing E-cadherin by disrupting endocytosis reduced the correlation between area phase and vertex movements, again consistent with E-cadherin dynamics directing productive vertex sliding events. These results demonstrate that E-cadherin is specifically recruited to contracting vertices during apical cell area oscillations and suggest a mechanism to achieve anisotropic stabilization of vertex movements.

3.1.7 Myosin II Directs Phasic E-cadherin Enrichment at Cell Vertices

Previous work has shown that medial Myosin II networks flow towards cell interfaces, and locally cluster E-cadherin for endocytic uptake [49, 41]. This raised the question as to whether medial Myosin II networks could similarly influence the localization and dynamics of E-cadherin at vertices. Simultaneous imaging of Myosin II:mCherry and E-cad:GFP revealed that, in addition to its previously described junctional and medial populations, Myosin II is highly, and dynamically, enriched at vertices (Fig. 3.11A-A"). This unexpected population of Myosin II exhibited a strong colocalization with vertex-associated E-cadherin (Fig. 3.11A and A'). Furthermore, systematic quantitation of vertex Myosin II and vertex E-cadherin demonstrated a strong cross-correlation, showing that the dynamics of enrichment of both proteins are temporally coupled (Fig. 3.11B). Interestingly, this cross-correlation function also revealed a slight temporal offset, with Myosin II becoming enriched at vertices about 3.3 seconds before E-cadherin (Fig. 3.11B). Similar to E-cadherin (Fig. 3.10B), phase-based analysis of Myosin II indicated an enrichment during periods of cell area contraction that is polarized to T1 associated vertices (Fig. 3.11C and C'). However, these dynamics again subtly preceded those of E-cadherin (compare Fig. 3.11C and C' and Fig. 3.10B and C). As was previously described for interfaces [49], live imaging of individual cell behaviors showed that approximately 50% of medial Myosin II flows moved toward vertices, resulting in vertex enrichment (Fig. 3.11D, E). Taken together, these observations show that Myosin II dynamics at vertices are similar to, but temporally precede, those of E-cadherin, and suggest a role for Myosin II in clustering E-cadherin at vertices. This additionally provides a potential mechanistic link between apical cell area oscillations and fluctuations in E-cadherin intensities at cell vertices.

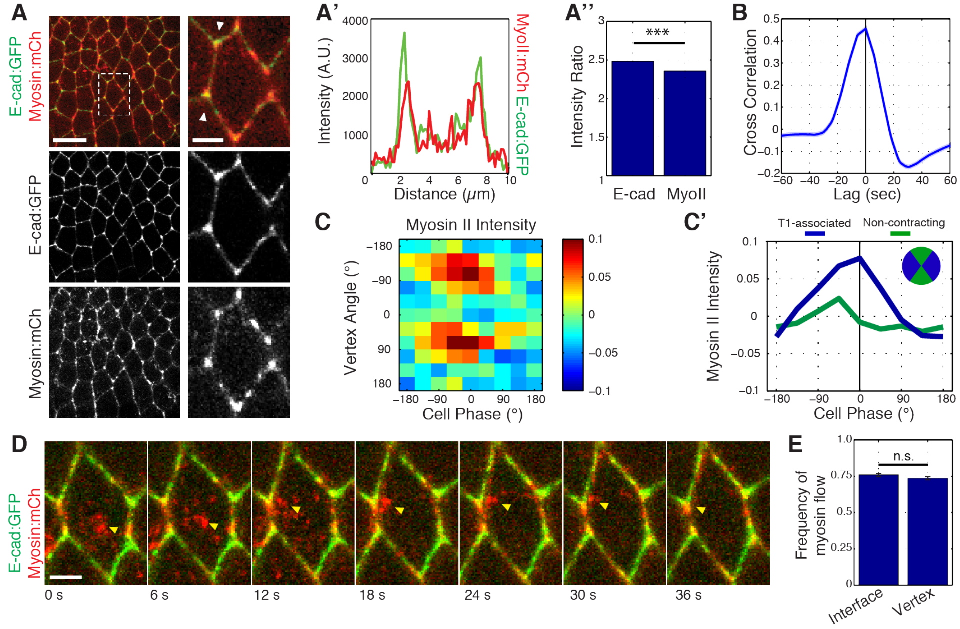

Figure 3.11: (A) Live imaging of Myosin II (mCh:Sqh, red) and E-cad:GFP (green) embryos during GBE. (A') Single pixel intensity line plot between arrowheads shown in (a). (A") Quantification of Myosin II (mCh:Sqh) and E-cad:GFP vertex intensity ratios (n = 44356 vertex time points). (B) Cross-correlation of the rate of change of intensity ratios for E-cad versus Myosin II (n = 800 vertices). (C) Heat map of the normalized Myosin II vertex intensity with respect to the vertex angle and area phase, n = 238 cells from three embryos. (C') Plot of average normalized Myosin II intensity for vertical and horizontal vertices with respect to area phase. (D) Time sequence showing medial Myosin II flows (yellow arrowheads) toward vertices in merged images. (E) Quantification of Myosin II (mCh:Sqh) flow destinations. The frequency shows the number of each myosin flow events per cell per min. (n = 30 cells and 537 Myosin II flows in three embryos, n.s., not significant). Data are from three embryos. Scale bars in (A) are 10 μm (left) and 3 μm (right). Scale bar in (D) is 3 μm. *** denotes p<0.0001. Statistical tests were done by Student's t-test. (A", E) Mean ± s.e.m are shown.

To investigate if Myosin II is required for vertex-associated E-cadherin behaviors, Myosin II was functionally disrupted by injection of the Rok inhibitor Y-27632. Injection of a high concentration of Y-27632 (100mM) disrupted E-cadherin enrichment to cell vertices, as well as E-cadherin dynamics (Fig. 3.12A, C, and E). Additionally, analysis of sqhAX mutant embryos produced a similar defect in vertex-associated E-cadherin. The phenotype of Y-27632 injected embryos was dose dependent, as injection of a lower concentration (25mM Y-27632) preserved an enrichment of E-cadherin at cell vertices (Fig. 3.12B). In this background, however, E-cadherin was not significantly polarized to T1 associated vertices, and it lacked cycles of vertex enrichment (Fig. 3.12D, F, and G). As a consequence, vertex displacement was severely disrupted in Y-27632 injected embryos at both concentrations (Fig. 3.12H and I). Interestingly, although productive vertex displacements are observed (Fig. 3.12H and I, red areas), these displacements are offset by backwards displacements (Fig. 3.12H and I, blue areas). These results are consistent with Myosin II functioning upstream of the ratchet-like behavior of E-cadherin at vertices. It is additionally important to note that cell area oscillations are highly disrupted in Y-27632 injected embryos, and that the observed lack of E-cadherin dynamics could represent a disruption of coupling between vertex populations of E-cadherin and medial actomyosin-dependent area oscillations. Either way, these results are consistent with a functional role for Myosin II in clustering E-cadherin at vertices and directing the stabilization of productive sliding movements.

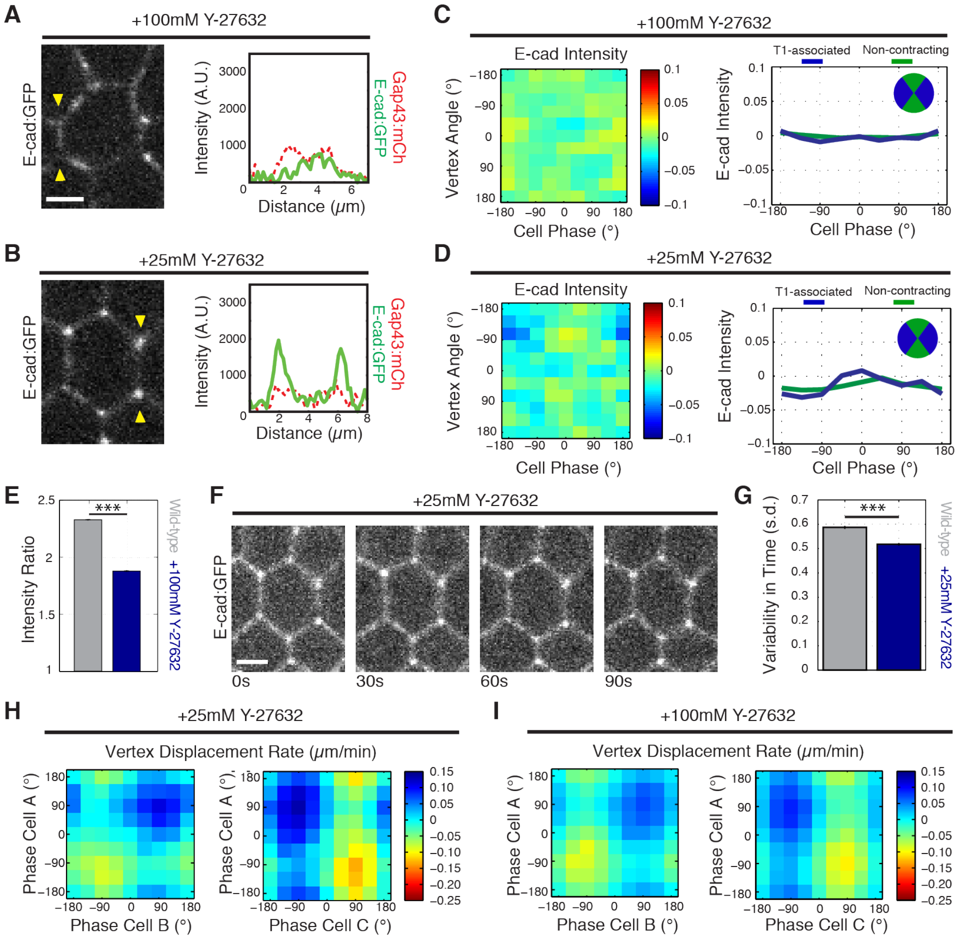

Figure 3.12: E-cad:GFP image of cell and single pixel intensity line plot between arrowheads for 100 mM (A) and 25 mM (B) Y-27632 injection. (C,D) Heat map and plot of the normalized E-cad:GFP intensity at vertices with respect to the angle of the vertex and the area phase for 100 mM (c, n = 409 cells) and 25 mM (d, n = 363 cells) Y-27632 injection. (E) Quantification of vertex-to-junction intensity ratios measured for each vertex and each frame of 5 min during GBE (n = 86939 vertex time points). (F) Time sequence of images showing loss of E-cad:GFP dynamics at vertices in 25 mM Y-27832 injected embryos. (G) The averaged standard deviation over time for each vertex's intensity ratio. Control, n = 3188 vertex trajectories; 25 mM, n = 1868 vertex trajectories. (H, I) Heat map of tangential vertex motion rates versus the phases of cell A and cell B (left) and cell A and cell C (right) for 25 mM (H) and 100 mM (I) Y-27632 injection. (H) n = 175 junctions. (I) n = 220 junctions. Control data from three embryos, Y-27632 25 mM from three embryos, and Y-27632 100 mM from three embryos. Scale bars are 3 μm. *** denotes p<0.0001. (E, G) Mean ± s.e.m are shown.

3.2 GBE Along the Apical-Basal Axis and T2-T3 Processes

Individual length time courses of T1 processes are very dynamic; instead of continuous sustained contraction or elongation, there are variable contraction and elongation steps mixed with sustained periods of stable interface lengths. Due to this variability, it is essential to average a large number of interfaces in order to gain insight into typical transition dynamics. Since the individual transitions are temporally staggered within the tissue over the course of several minutes, this was achieved by aligning all recorded individual interface transition measurements relative to their respective T2 time points (see Fig. 3.13A and B and Methods section 2.3.1). In the averaged aligned individual length trajectories (Fig. 3.13C, blue curves), the interface lengths are initially stable before they proceed through full contraction in T1 within 12 minutes; similarly, the final stable length of the new T3 interface is also reached within about 12 minutes of elongation. In order to quantify how the contraction phase in T1 and the elongation phase in T3 contribute to the ultimate goal of tissue elongation, a local tissue extension metric was introduced that quantifies the effective 'convergent extension' of the local neighborhood of the interface of interest (see Methods Fig. 2.8) by calculating the ratio between effective horizontal and vertical cell neighbor distances (Fig. 3.13C, green curves). It was found that the AP interface contraction phase during T1 contributes only about a third of the functional extension, while two thirds is produced during the elongation of the new horizontal interface during T3. This suggests that, mechanistically, the contraction phase can be thought of as a priming or nucleation step, whose primary purpose is not to produce significant tissue extension per se, but to create the higher-order vertices whose subsequent resolution into the desired direction is the primary mechanism for tissue elongation.

Through examining the 5 minutes immediately before and after T2 formation more closely (Fig. 3.13C, right panel), there were two additional features of interest: First, the average rates of T1 contraction and T3 elongation are strikingly similar; this is somewhat unexpected because the prevailing mechanistic model suggests that contraction and elongation are driven by physically and molecularly completely distinct mechanisms. In addition, it is notable that there is no visible 'saddle' of the length time course at the T2 configuration at t=0 (instead, the slope even appears to increase in the vicinity of T2); this suggests that once interfaces have fully contracted, the elongation of the new interface can proceed without any required minimum waiting period in the T2 configuration.

3.2.1 Leading Layer Behaviors Occurs Throughout the Apical-Basal Axis

Planar-polarized Myosin II structures are enriched at cell-cell boundaries near adherens junctions and in the apical cell cortex [50, 19, 49]. Given this localization pattern, if contraction of these structures is the driver for AP interface contraction, then one would expect interface remodeling to be initiated at the apical end of cells, and to propagate from there along the apical-basal axis. To test this hypothesis, T1 transitions in 4D movies (x, y, z, and t) were taken at 0.2Hz (5s between individual z-stacks) with cross-sections starting just below the apical cap spaced 2 μm apart, spanning 12 μm basally. The time lag between individual cross-sections of the same z-stack was 0.27s. Tracking the interface length in each layer (Fig. 3.14A), allowed identification of the 'leading layer' at each time point, i.e., the depth along the apical-basal axis in which contraction or elongation of the interface had progressed the furthest (see Methods section 2.3.3). It was observed that both apical and basal

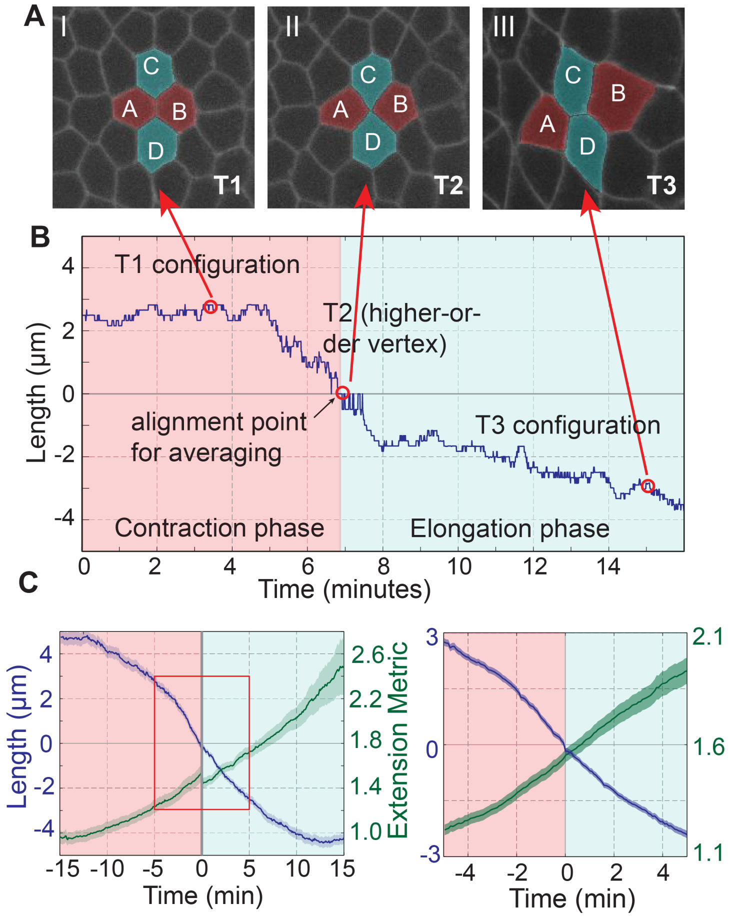

Figure 3.13: (A) Sample transition from T1 configuration to T3 configuration; AP neighbors (red) are designated as cells A and B, and DV neighbors (green) are designated as cells C and D. (B) Interface length time course for the sample cells shown in (A) where the red highlighted region corresponds to the length of the contracting T1 junction and the green highlighted region to the elongating T3 junction (negative values are assigned to T3 lengths for graphical purposes). Red arrows indicate the time points corresponding to the cell configurations in A. (C) Average of length traces aligned to the T2 time point (blue trace, plotted on left axis) and corresponding extension metric (green trace, plotted on right axis). Left: Average of interface trajectories with minimum length of 15 min either pre-T2 (n=37) or post-T2 (n=40); Right: Zoom-in corresponding to red bounded region in left panel; average of interface trajectories that were continuous from 5 min pre-T2 to 5 min post-T2 (n=147). Length dynamics are similar in T1 and T3.

layers can act as leading layers during T1 and T3, and that the leading layer can switch from apical to basal on the timescales of minutes within the same interface. In the sample trajectory in Fig. 3.14A, there are two examples of cross-over events (see arrows), one around the 7 minute mark, where the most basal layer overtakes the most apical layer in contraction, and another instance around the 13 minute mark, where the apical layer overtakes the most basal layer in elongation. This example shows that the apical layer can precede (or lag behind) the most basal layer by ≈ 2 mins or more (in the example shown in Fig. 3.14A this is visible during the minutes immediately following the indicated cross-over events).

Systematic examination of the leading layer at the T2 time point revealed that T2 is initiated in the apical layer in only about 34% of the interfaces (Fig. 3.14A right panel) and that about 44% of the interfaces first reach T2 configuration at a z-depth of 8 μm or more. This result does not support an exclusive role for the apical side of the cells in driving the progression of contraction. The contribution of apical and basolateral layers in T1 transitions was quantified by identifying the leading layer for all available T1 transitions as a function of time (Fig. 3.14B). It was observed that during the time window between about 13.5–10 minutes before T2, the fraction of apically leading interfaces increases rapidly from around 40% to about 60%, which indicates that the ongoing contraction during this time period has to be preferentially initiated from the apical side. However, the apical contribution peaks at approximately 9 min before T2, and the fraction of basolaterally leading interfaces increases steadily for the rest of the T1 phase, indicating that ongoing contraction during this time period has to be preferentially initiated from the basolateral side. A few minutes into T3 configuration, the apical and basolateral fractions reach a plateau, which indicates that new elongation events during this period initiate apically and basolaterally with approximately equal probabilities. Thus, a preference for apical initiation can only be found in a transient phase during the earliest stage

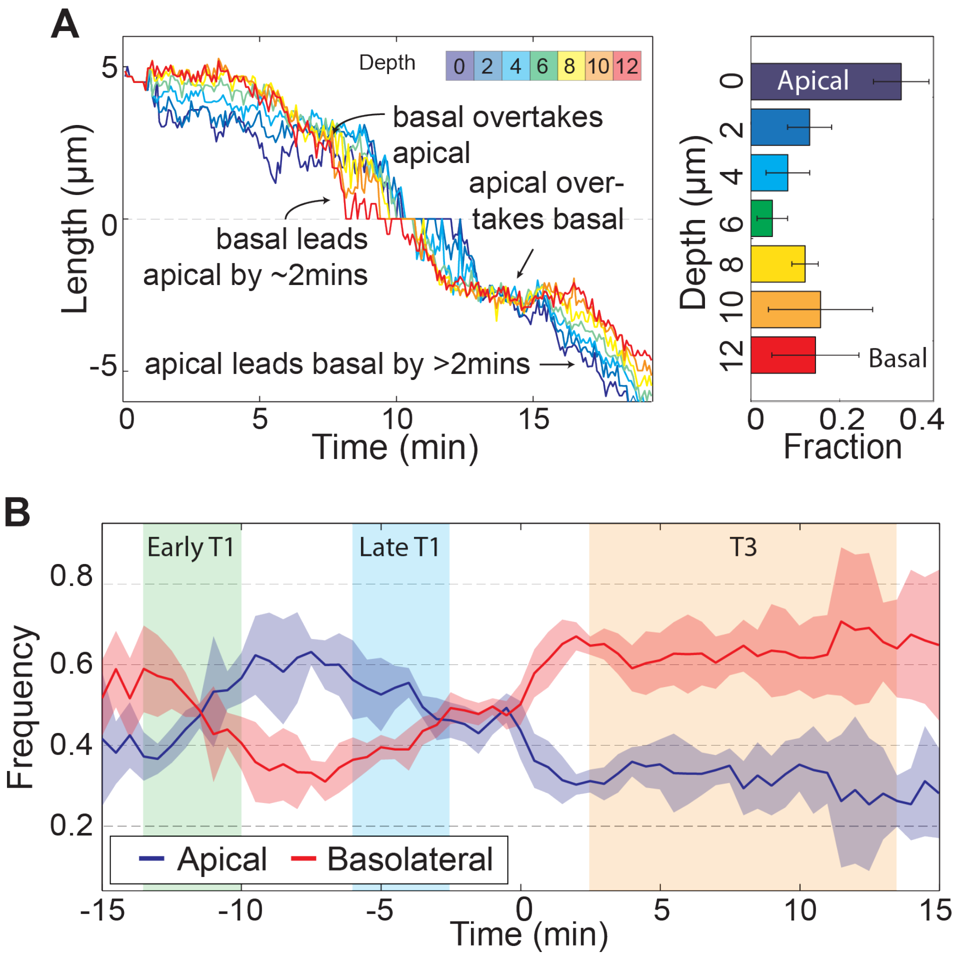

Figure 3.14: (A) Interface length time courses for all layers in a z-stack. Trace color corresponds to z-depth. Histogram indicates the number of events where the specified depth layer is the leading layer at T2 (n=197 transitions, k=4 embryos, average and STD error over embryos). (B) The average frequency over time with respect to the T2 time in which the apical (blue trace) and basolateral (red trace) layers leads in terms of interface length (mean is the average over the 4 movies, shaded regions are standard deviations).

of GBE (which contributes only a small fraction of the total length contraction of T1 interfaces), while the majority of the T1 contraction phase sees a slight preference for basolateral initiation, and T3 elongation events are about equally weighted between apical and basolateral.

3.2.2 Length and Area Changes Propagate Along Apico-Basal Axis

To examine spatiotemporal dynamics of remodeling quantitatively, interface length and cell area gradients (for time shift of 25s) were extracted for all available time points and across all z-layers in each T1 process. In the length gradient (see heat map in Fig. 3.15 top panel), there is a distinct striped pattern indicating length contraction and elongation 'pulses'; similar cycles of shrinkage and stabilization were observed by [49]. Importantly, as discussed previously, both positive and negative slopes in these stripes were observed that indicate propagation from the basal to apical and vice versa, where the slope of the stripes corresponds to the propagation velocity in z-direction. Similar propagating pulse properties were observed in the area gradients of the participating cells (Fig. 3.15 middle and lower panel show the average gradient of the two participating AP neighbors and of the two participating DV neighbors), consistent with area oscillations observed by [20].

3.3 The Role of Rab35 in GBE

3.3.1 Rab35 Behaviors are Enhanced at AP Interfaces

Rab35, as shown by a YFP:Rab35 transgene, displays striking compartmental behaviors at interfaces between AP neighboring cells during cell intercalation (Fig. 3.16A and B). Prior to cell intercalation, Rab35 is present at low levels at the plasma membrane (Fig. 3.16A, left panel). However, once GBE has initiated,

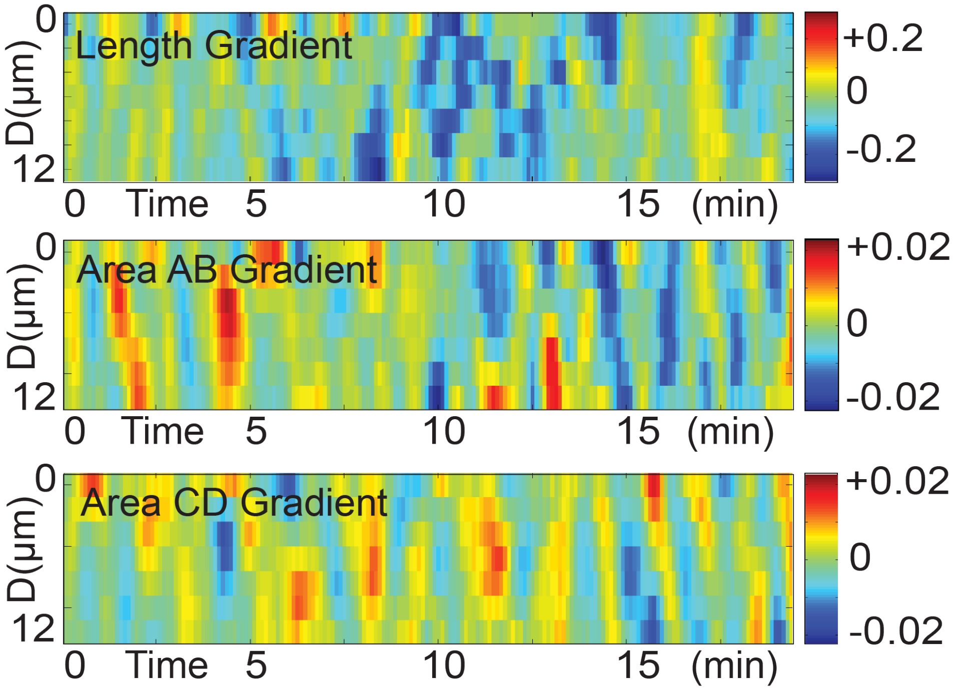

Figure 3.15: Heat map representations of the length gradient (top) and the relative area gradients of the average of cells A and B (middle) and cells C and D (bottom) (designation of cells A-D as in Fig. 3.13A).

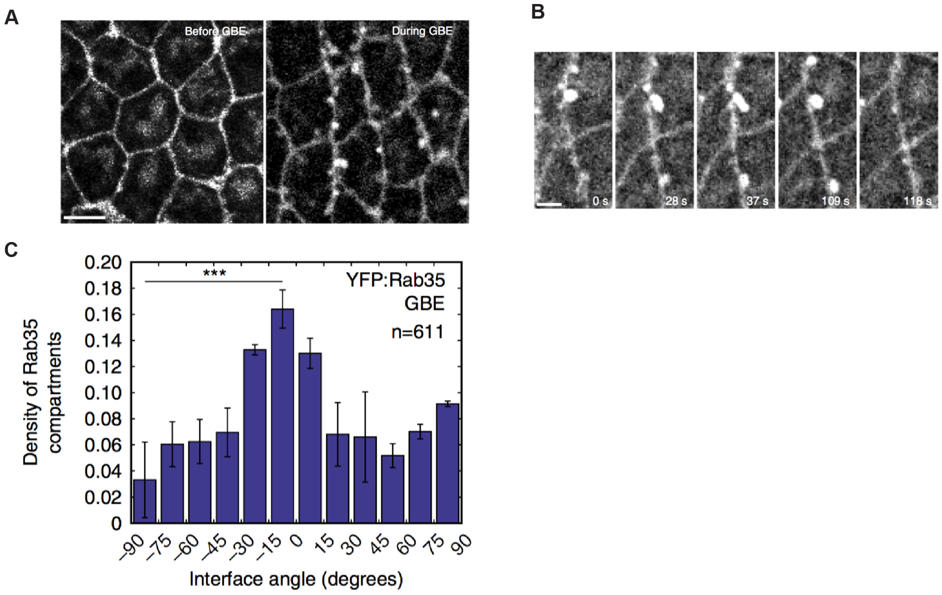

Figure 3.16: Planar polarized Rab35 compartments associate with AP interfaces during periods of active interface contraction. (A, B) Time-lapse images of embryo expressing YFP:Rab35. All images, anterior is to the left and ventral is down. a YFP:Rab35 compartments localize to AP cell interfaces after GBE begins (right image). (B) Representative images depicting the life cycle of a Rab35 compartment: initiation of YFP:Rab35 compartment (0 s), growth phase (28 s), maximum compartment size (37 s), shrinkage (109 s), and compartment termination (118 s). (C) Rab35 compartments occur more frequently at AP interfaces. Compartment density plotted as a function of binned interfaces angles in the germband (n = 611 compartments). Quantification in (C) was performed by Roopa Madhu.

spherical and tubular Rab35 compartments form at the plasma membrane, grow for 1–2 min, and then terminate and disappear from the plasma membrane (Fig. 3.16A, right panel, and B). Rab35 compartmental behaviors are planar polarized, with 57% of measured compartments present at interfaces ranging within 30 degrees of the vertical axis (AP interfaces), while only 11% of compartments were present at interfaces within 30 degrees of the horizontal axis (DV interfaces) (Fig. 3.16C; quantification performed by Roopa Madhu).

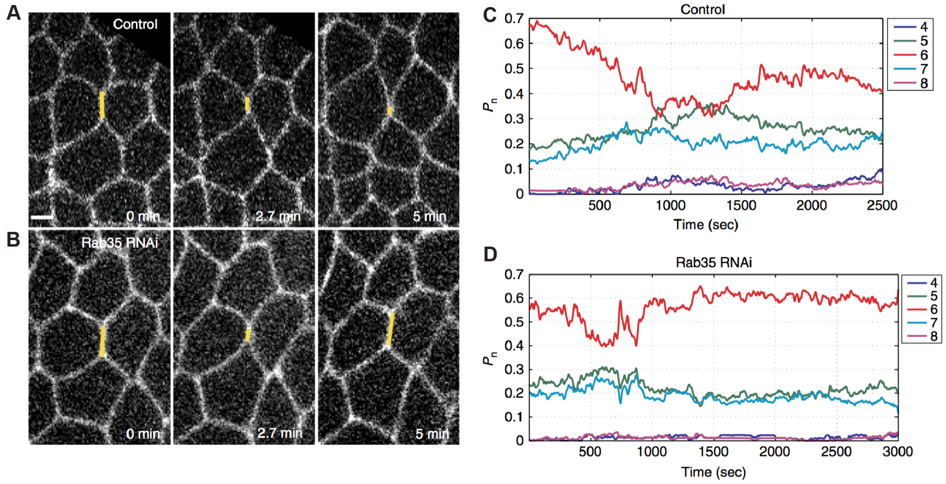

Figure 3.17: Rab35 promotes progressive interface contraction required for cell intercalation. (A, B) Still frames of embryos expressing a cell outline marker (Resille: GFP) injected with control dsRNA (Rhodopsin3, Rh3, A) or Rab35 dsRNA (B). In control-injected embryo, the AP interface (yellow line) has fully contracted after 5 min. (B) In the Rab35 knockdown embryo, the AP interface (yellow line) undergoes an initial contraction (middle panel) but reverses itself. After 5 min the interface shows no net contraction (right panel). (C, D) Frequency of n-sided cells during germband extension in control Rh3 dsRNA and Rab35 dsRNA embryos (n = 74 and 83 cells, respectively). Germband extension initiates as a primarily hexagonal lattice in both control and Rab35 dsRNA embryos. In control embryos, the number of six-sided cells rapidly decreases, while the number of alternatively sided cells increases as convergent extension movements occur. In Rab35 dsRNA embryos, there is a slight initial decrease in hexagonal cell number, before cell topologies return to the initial configuration.

3.3.2 Rab35 is Required for Progressive Interface Contraction

Next, this study examined the effect of disrupting Rab35 function on cell topologies and neighbor relationships during GBE. In Rab35 compromised embryos, cell intercalation was deeply disrupted (Fig. 3.17A and B). The epithelial sheet maintains a primarily hexagonal configuration, with little evidence of neighbor exchange (Fig. 3.17A–D; see Methods section 2.4.5).

In Rab35 dsRNA-injected embryos during the early phase of cell intercalation, it was found that the overall contraction of AP interfaces was deeply compromised,

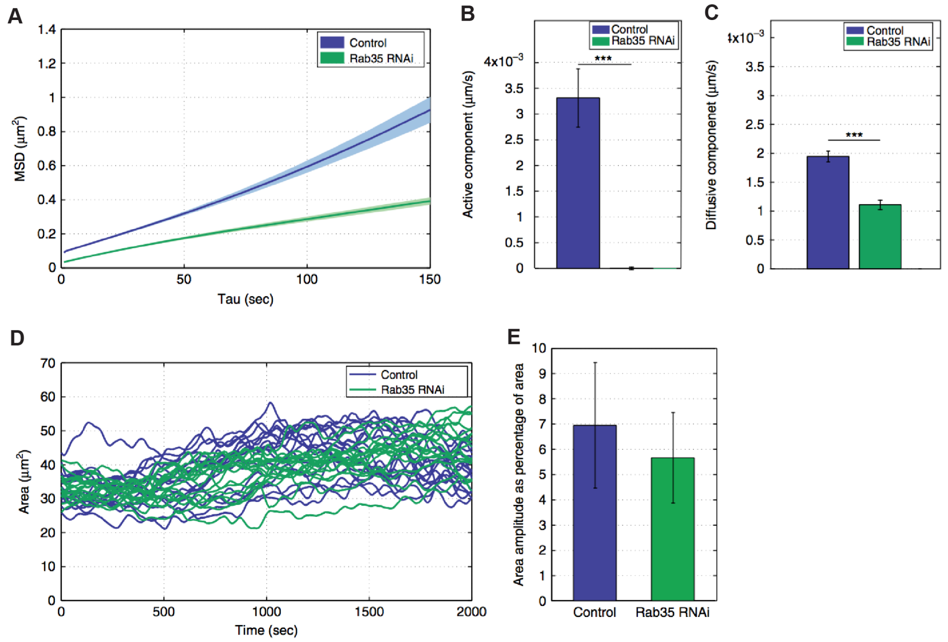

Figure 3.18: Rab35 promotes progressive interface contraction required for cell intercalation. (A–C) Rab35 dsRNA embryos have a decrease in productive interface contractions with reduced MSDs (A), a near absence of the active MSD component (B), and decreased diffusive component (C). n = 286 (control) and 139 (Rab35 dsRNA) cells. (D, E) Oscillations in apical area still occur in Rab35 dsRNA embryos (D), with an amplitude similar to control Rh3 dsRNA-injected embryos (E). n = 631 (control) and 340 (Rab35 dsRNA) cells. Student's t-test, ***$P < 0.0005$. Error bars indicate standard error. Scale bar is 2.5 microns

with decreased active motion components as determined from mean squared displacement analysis (Fig. 3.18A–C; Methods section 2.4.2). However, when individual AP interfaces were examined in Rab35-disrupted embryos, wobble-like behaviors were often observed in which initial periods of interface shortening occurred, but were then followed by a re-lengthening of the interface (Fig. 3.17B). Oscillations in apical area still occur, and the amplitude of these oscillations is similar to that observed in control-injected embryos (Fig. 3.18D and E).

In order to examine the wobble-like behaviors in Rab35-disrupted embryos more closely, an automated step-detection algorithm was used to detect periods of directed movement. AP interfaces in Rab35 compromised embryos still undergo steps with the same frequency, duration, and size as in control embryos (Fig. 3.19A–D). However, contractile steps in Rab35-disrupted embryos are often followed by steps with a positive displacement (Fig. 3.19B inset, E). Due to these reversals, the net stepped distance is much lower in Rab35 compromised embryos (Fig. 3.19F). These results are consistent with Rab35 functioning as a ratcheting module that directs progressive shortening of AP interfaces in response to apical area oscillations.

3.3.3 Rab35 Functions in a Conserved Cell-Shaping Mechanism

Finally, the invaginating mesoderm was analyzed to determine whether Rab35 directs a common contractile mechanism in the generation of cell shapes. Invagination of the mesoderm in the early *Drosophila* embryo occurs through the formation of a ventrally located furrow [40, 61]. Furrow formation is driven by constriction of the apical epithelial surface, a process that relies on radially polarized actomyosin behaviors [16, 21, 43, 44]. Here, too, it was found that Rab35 displays compartmental behaviors at the cell surface. Rab35 compartments form at the apical end of cells undergoing apical constriction in the ventral furrow (Fig. 3.20A). However, Rab35 compartmental behaviors, while polarized in the apical-basal axis, do not demonstrate planar polarities (Fig. 3.20B) and are enriched apically and not at interfaces. Rab35 compartments are therefore specifically polarized to shrinking cell surfaces in cells undergoing cell intercalation or apical constriction in the early embryo. Rab35 function is required for mesoderm invagination, as ventral furrow formation fails in embryos injected with Rab35 dsRNA. Additionally, rates of apical constriction are greatly reduced in embryos in which Rab35 function has been compromised (Fig. 3.20C and D). These results reveal a common direction of Rab35 to shrinking cell surfaces as well

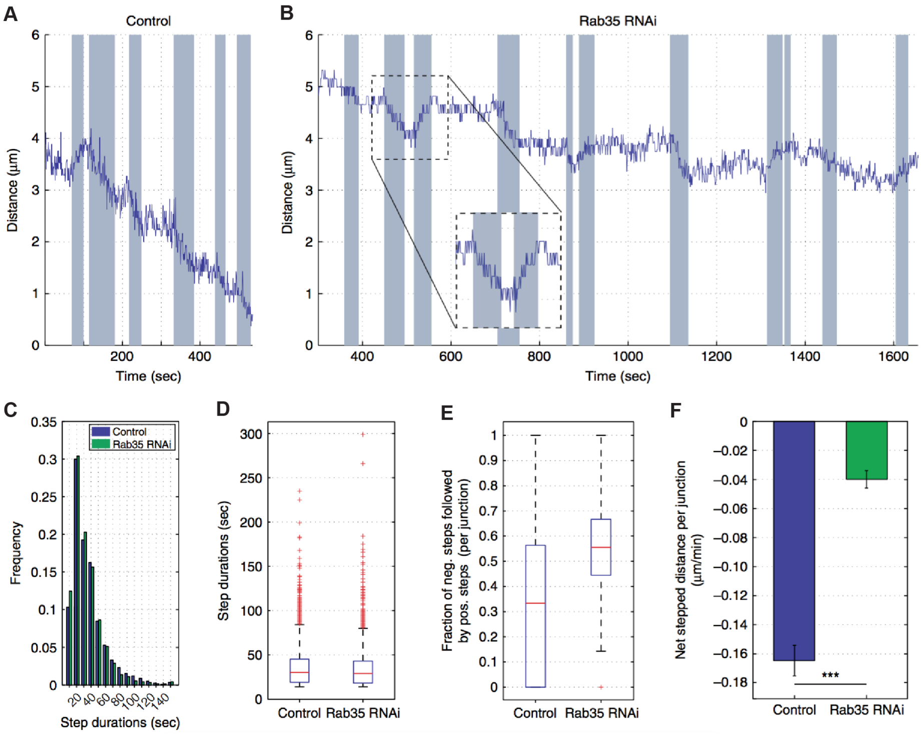

Figure 3.19: (A, B) Individual AP interface length plots in control Rh3 (A) and Rab35 dsRNA (B) embryos. Automated step detection indicates periods of active interface length change (shaded regions). A control interface progressively contracts within 8 min (A), while a Rab35 dsRNA interface undergoes active contractile steps followed by lengthening reversals (B, inset). After nearly 30 min, the AP interface is still preserved in Rab35 dsRNA embryo. (C, D) The histogram of duration (C) and box plot of duration (D) of active stepping is similar in control and Rab35 dsRNA embryos. n = 2990 (control) and 2536 (Rab35 dsRNA) steps. (E, F) Contractile steps are often reversed by positive stepping in Rab35 dsRNA embryos (E) producing a decrease in net displacement (F). n = 328 (control) and 340 (Rab35 dsRNA) interfaces. Error bars indicate standard error. Student's t-test, *** $P < 0.0005$

as a requirement for Rab35 function in shaping epithelial cell behaviors during development.

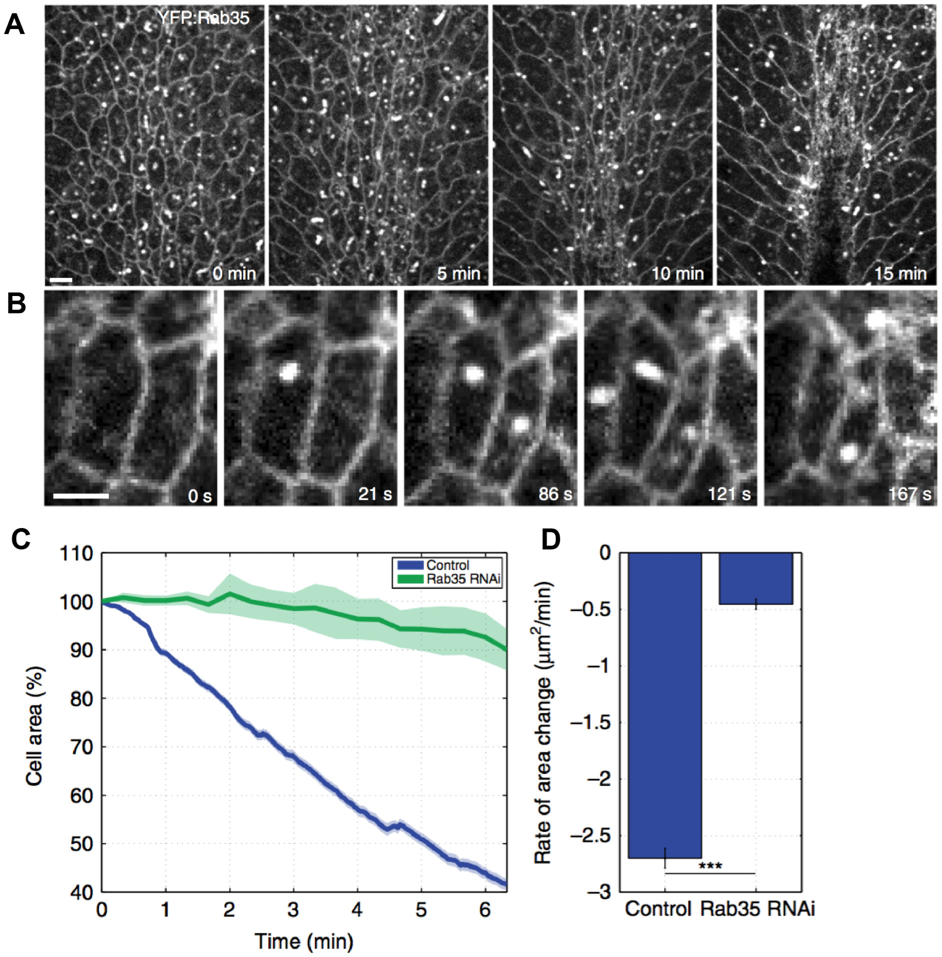

Figure 3.20: Rab35 compartments represent a common contractile mechanism. (A) Rab35 compartments form at contractile surfaces in cells undergoing apical constriction. Time-lapse images of an embryo expressing YFP:Rab35 during ventral furrow formation. (B) Rab35 compartments form on the medial-apical cell surface away from cell-cell interfaces. (C) Plot of percent apical area contraction from automated analysis of ventral furrow cells in control (blue, n = 226 cells) and Rab35 (green, n = 313 cells) dsRNA embryos. (D) Reduction in area rate changes and decreased apical contraction in Rab35 dsRNA embryos compared to control embryos. Student's t-test, ***$P < 0.0005$. Error bars indicate standard error. Scale bars are 5 microns.

Chapter 4

Discussion

4.1 Uncoupled Vertex Sliding

In summary, radial force coupling drives ratchet-like contractions of AP interfaces. The data shown introduces a new functional unit capable of regulating cell topologies — tricellular vertices. A new mechanism driving cell shape remodeling was identified, in which tricellular vertices slide laterally in response to medial force generation (Fig. 4.1). Much of the previous focus in studying intercalary behaviors has been on changes in cell adhesion and force generation at cell interfaces [4, 5, 19, 50, 49, 33, 17, 13, 46]. While higher line tensions at AP interfaces clearly exist and direct distinct aspects of intercalary cell behaviors (such as interface alignment along the DV axis, recoil velocities upon laser ablation, and boundary element behaviors), it will be interesting to further explore the mechanisms regulating tricellular vertex function [50, 19, 63]. As vertices are connected to three (or more) interfaces as well as the radial coupling reported on here, their displacement will rely on the summed total of these local force contributions. Some of the mechanisms may involve the endocytic uptake of plasma membrane and adhesion proteins at interfaces which have been recently described [41, 32]. These molecular models of regulated adhesion are not necessarily dependent on line tensions, and could contribute to the biases in lateral vertex displacements, in particular tangential directions. Although the data presented here argues against a predominant function of interface-spanning line tensions in directing interface contraction, local regions of either medial- or interface-associated Myosin II are likely to impact vertex displacements as well. Indeed, although E-cadherin and Myosin II are primarily located at cell vertices early in GBE, by mid-GBE interface localization of both significantly strengthen and is consistent with interface as well as radial contributions to vertex displacements. Thus, cell vertices are well positioned to integrate the many different force-generating networks that will ultimately determine changes in cell shape and topology.

These results show that intercellular adhesion dynamics are required for vertex movement. Under conditions in which E-cadherin exhibited greater enrichment and/or stability than is present in wild-type embryos, AP and transverse interface lengths oscillated identically, suggesting that cell vertices were unable to slide productively due to increased adhesive stability. Stabilizing E-cadherin was achieved by inhibiting endocytosis [41], and suggests that endocytic events may underlie the dispersion phase of E-cadherin dynamics at cell vertices. Given that endocytic pathways centered on asymmetric planar behaviors of Clathrin, Dynamin, and Rab35-dependent functions have been previously identified [41, 32], it will be interesting to further explore if these same pathways function at or near cell vertices to direct E-cadherin dynamics, and whether endocytosis at vertices or at interfaces is more responsible for vertex E-cadherin redistribution. However, one interesting implication of this work is that these endocytic pathways should alter the balance of adhesion on either side of a vertex, potentially through the uptake of E-cadherin adhesion molecules, but the combined length of T1 and transverse

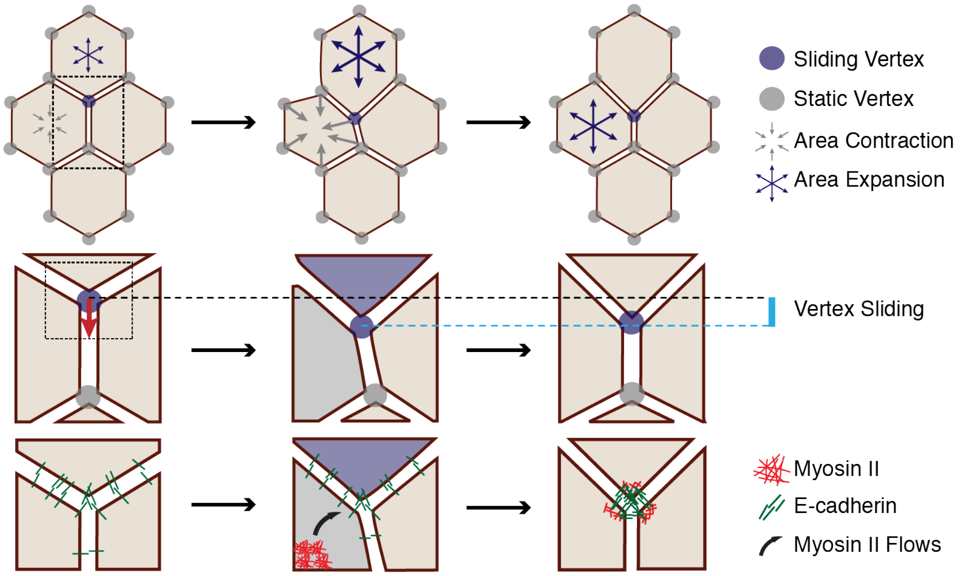

Figure 4.1: Model for vertex-directed changes in cell topologies. As a cell adjacent to a vertex along the AP axis contracts (gray arrows), and the adjacent cell along the DV axis expands (blue arrows), the vertex experiences a cumulative asymmetric force, causing it to slide along the interface (middle row, cyan line). At the molecular level, medial Myosin II flows consolidate E-cadherin at cell vertices post-vertex sliding, resulting in a local increase in adhesive stability. This is coordinated with oscillations in apical cell area, which ensures progressive, non-reversible vertex displacements (bottom). Gray shading indicates a contractile phase; blue indicates expansion.

interfaces would remain largely unchanged. This again suggests that the positioning of cell vertices will reflect the combined activities of contractile and adhesion elements that are located directly at the vertex as well as in local regions near the vertex. It also underlines the importance of cell vertices, and suggests a primary importance of vertices in determining cell topologies, which is further indicated by the strong enrichments of E-cadherin and Myosin II at cell vertices during early GBE. Regardless, it will require additional work to tease apart the contributions of E-cadherin stabilization and turnover pathways at cell vertices versus cell interfaces.

As cells contract their apical area, E-cadherin and Myosin II are preferentially recruited to AP vertices to provide the adhesive force necessary to stabilize vertex position and interface length during area relaxation. This, as well as anisotropy in cell area oscillations and local imbalances in interface-associated forces [49, 20, 54], are likely responsible for enforcing the directionality of intercalation. The results also suggest that, while radial forces in cells sharing a contracting AP interface are important for vertex displacement, vertex displacement has the strongest correlation with expansive motion in the adjacent, DV oriented cells. This is intriguing, and suggests a homology to recent results during interface extension in which the adjacent cells provide motive force for extension rather than the cells that share the newly growing interface [13, 31]. At the molecular level, AP vs DV anisotropy at the level of vertices could be a result of stress anisotropy and a mechanosensory feedback loop. Alternatively, vertices may also experience differentially positioned signaling networks, allowing for Myosin II and E-cadherin vertex enrichment.

While the planar sliding behaviors described here are a novel mechanism underlying intercalary behaviors, it is also interesting to note that a similar adherens junction sliding behavior has been observed during three dimensional epithelial folding events as well as during cell ordering in the *Drosophila* notum [68, 69, 14]. In the formation of the epithelial folds that occur on the dorsal surface of the embryo in response to GBE, there is a basal shift in adherens junction position in response to Rap1 signaling events [68, 69, 62]. It will be intriguing to explore if a similar Rap1-dependent pathway operates on cell vertices during cell intercalation. It is also highly interesting that, in the *Drosophila* pupal notum, a similar conservation of total junctional lengths, referred to as 'continuous neighbor exchange' has been observed [14]. It may well be that the repositioning of junctional/vertex elements will represent a new and conserved paradigm in how cell topologies are re-shaped during development.

There is a growing body of work on tricellular vertices as unique epithelial structures. Previous studies have shown that cell vertices possess important molecular characteristics capable of coordinating complex cell morphologies [59, 47, 56, 29, 5, 8]. Indeed, recent work has shown that tricellular junctions act as key sensors of cell shape that serve as landmarks to orient epithelial cell divisions [7], and intestinal stem cells require tricellular function to maintain appropriate homeostatic levels [52]. This suggests that vertices represent unique domains of the cell surface and that tricellular vertices have a special role as centers of functional signaling and physical networks within epithelial sheets.

4.2 GBE Along the Apico-Basal Axis and T2-T3 Processes

It is notable that similar and symmetric behavior was observed for contraction in T1 and elongation in T3. In the prevailing line tension model, T1 interface contraction is caused by active planar-polarized actomyosin contraction, while subsequent elongation of newly formed T3 interfaces is the result of elastic relaxation of the cell shape, i.e. these processes are currently thought to occur through molecularly and mechanically completely distinct processes. As a result, there would be no compelling reason that the time constants for contraction and elongation to be similar. Thus, the symmetry of T1 and T3 behavior observed suggests to us that the mechanisms could be more similar between T1 and T3 than previously believed. The sliding vertex model could represent a feature of this common mechanism, as cell boundaries remodel themselves in response to cell area oscillations. Current research efforts are to apply the same analysis techniques that were used to study vertices and lengths during T1 to the T3 process.

Due to the demonstrated central role of myosin, all mechanistic models for GBE have postulated a special role for the apical cap, where most of the myosin is concentrated and where a clear planar-polarized distribution of actomyosin proteins exists. Thus, interface length contractions generated by the transient increase of actomyosin-mediated AP line tension would be expected to initiate at and propagate from the apical cap towards basal regions of the cell. However, quantitative analysis failed to uncover an exclusive (or even strongly preferred) role for the apical layer. Instead, it was observed that interface contractions and elongations are initiated along the full length of the observable apical-basal axis and propagate into both directions. In addition, the layer that 'leads' in contraction/elongation can switch on the timescale of minutes between more apical and more basal layers for the same interface.

For future directions, recently the Blankenship lab has been able to produce imaging with greater signal to noise deeper towards the basal side of the epithelium. Some preliminary work has shown that the tissue can be segmented accurately up to about 20 microns deep or more. It will be interesting to reapply the same analysis on this new data to see what is happening closer to the basal end during both the T1-T2 and T2-T3 transitions. If there are two separate mechanisms at play on the apical and basal ends of the cell, an interesting question is how these two mechanisms communicate with each other to ensure the same intercalary changes are occurring. The result that T1 process sometimes lead basally seems to be in agreement with the recent findings that rosettes sometimes lead basally [60] so it would also be interesting to look at actin basally in T1 processes to see if similar actin protrusions are occurring.

4.3 The Role of Rab35 in GBE

Changes in cell shape in many systems are driven by pulsatile processes that initiate directed movement before cycling through periods in which the force generating network reforms [53, 49, 20, 43, 58]. Previous work on ratcheting function has concentrated on different actomyosin regimes governed by Myosin II regulators such as Rho1 and Rok that trigger contraction and cell ratcheting [46]. Importantly, when Rab35 function is disrupted, apical cell areas maintain oscillatory behaviors and AP interface lengths still undergo brief periods of contraction. However, contractile periods are followed by reversals and interfaces re-lengthen, producing a failure in interface shortening. This ‘wobble’ behavior is consistent with Rab35 functioning as a ratchet ensuring unidirectional movement during interface contraction.

Myosin II is found in several different populations within intercalating cells. Transient, web-like Myosin II localizations are found in highly dynamic structures in the apical/medial regions of epithelial cells, while more stable, cable-like structures are present at cell junctions [4, 5, 49, 20]. Junctional Myosin II enrichment is dependent on Rab35 function, and is required for the termination of Rab35 compartments. However, the role of apical/medial actomyosin forces and cell oscillations on Rab35 compartmental behaviors is less clear. It appears that Rab35 compartments may require Myosin II medial ‘flows’ [49] to function as a polarizing cue, as Rab35 compartments become less planar polarized in the absence of Myosin II function. One hypothesis is that cell oscillations produce cycles of high and low tension during which Rab35 compartments can form as infoldings of slackened plasma membrane that, when internalized, prevents interface length from rebounding to the same length as was present prior to area contraction (Fig. 4.2).

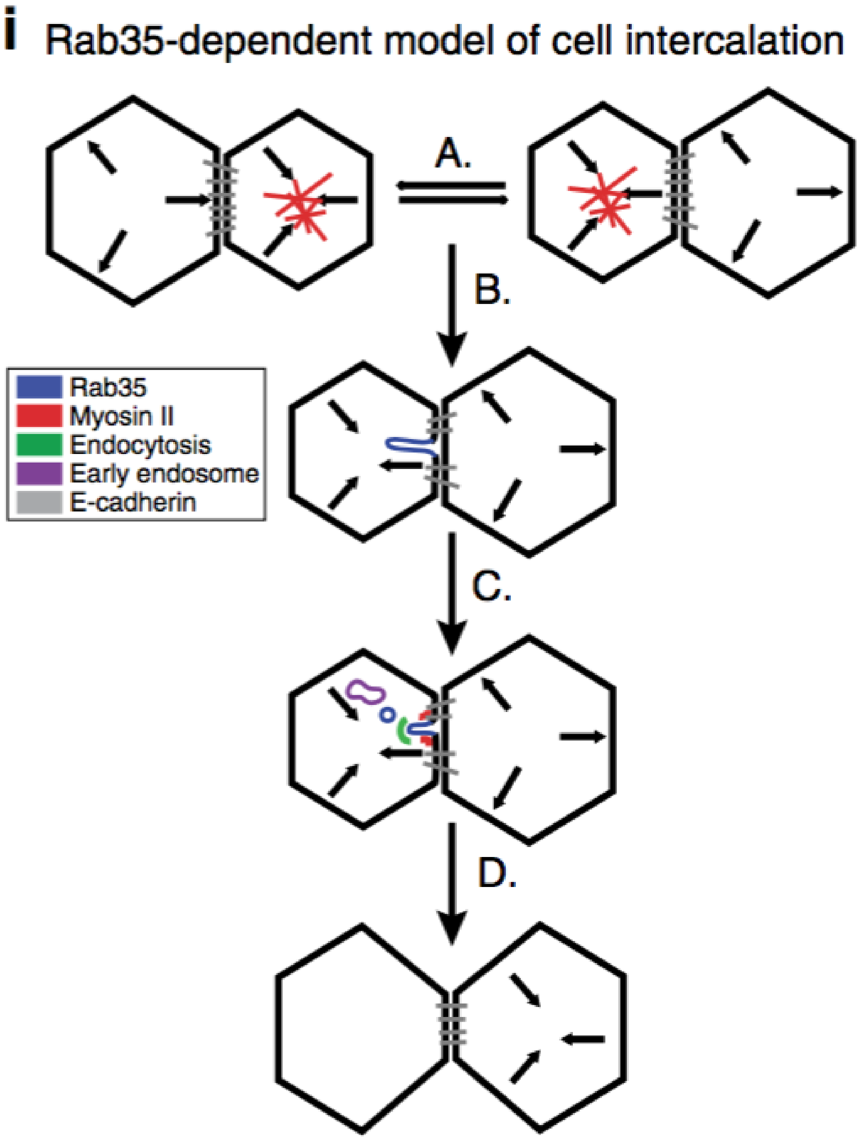

Figure 4.2: Model of Rab35-driven cell shape changes during cell intercalation. (A) Cells undergo oscillatory periods of apical area constriction driven by medial Myosin II (red). (B) Rab35 (blue) compartments take up excess plasma membrane during periods of asymmetric tension generation. (C) Rab35 directs compartment termination through the activity of junctional Myosin II (red) and endocytosis (green) with membrane delivery to internal endosomal stores (purple). (D) AP interfaces are shortened by the uptake of plasma membrane and/or E-cadherin adhesion complexes (gray), preventing a reversal in interface length.

Chapter 5

The Role of the Exocyst in Cytokinesis

5.1 Introduction

Cytokinesis results in the physical separation of two daughter cells. Immediately prior to cytokinesis, cells begin to elongate along the spindle axis, concomitant with anaphase spindle elongation. To achieve such a fundamental remodeling of shape and topology, cells martial multiple cytoskeletal and membrane trafficking pathways. Contraction of an equatorial actomyosin ring is required for inward progression of the cleavage furrow, and a further abscission process operates to fully separate the daughter cells (Fig. 5.1). Processes that regulate membrane trafficking events are also required for successful cytokinesis.

The following results demonstrate that funnel cakes (*fun*) and onion rings (*onr*) encode the exocyst proteins Sec8 and Exo84, respectively. Dividing spermatocytes mutant for either *onr* or *fun* display an exceptionally early defect in progression of the cleavage furrow. Quantitative analysis suggests that rather than disrupting gross membrane addition to the cell surface, these mutations specifically affect a

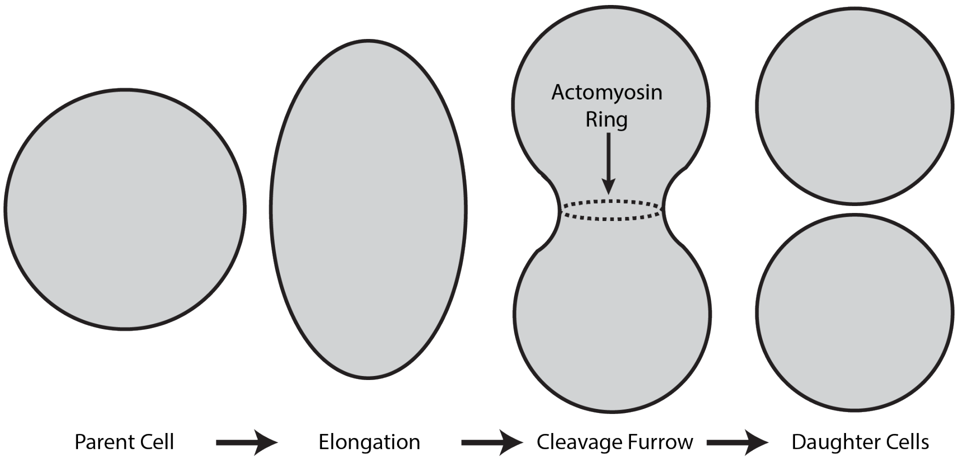

Figure 5.1: The parent cell which starts out somewhat spherical begins to elongate during anaphase. An actomyosin ring forms at the equator and contracts to create a cleavage furrow. Finally, the cleave furrow pinches off resulting in two daughter cells.

trafficking pathway required for both anaphase cell elongation and cleavage furrow ingression.

5.2 Methods

The methods for this project can be broken down into two basic categories: 1) The methods associated with segmenting cells from raw 3D image stacks over a time series, and 2) the methods associated with measuring the relevant geometrical properties of the cells and that of combining data from multiple cells to average these properties. In this project there was a specific interest in the role of membrane trafficking to the PM (plasma membrane) so one important parameter to measure was the cell surface area, i.e., the amount of PM. Another parameter of interest in cytokinesis is the cell volume because the ingression furrow could grow as a result of decreasing volume while holding surface area constant. As such, any decrease in volume would mean less additional surface area would be required to achieve the same amount of furrow ingression. Another interest was in quantifying the cell shape changes that are commonly associated with cytokinesis: anaphase elongation and furrow ingression. These properties were quantified using the aspect ratio to measure elongation and a measure called the convex hull volume ratio (CHVR) to quantify the amount of ingression. These parameters will be described in more detail below.

5.2.1 Imaging

Time-lapse imaging of PLCδd-PH-GFP and β-Tub-GFP was performed on a spinning disk confocal microscope from Zeiss and Solamere Technologies Group with 63x/1.4NA objectives. PLCδd-PH-GFP is used to tag the plasma membrane for the purpose cell segmentation and β-Tub-GFP tags microtubules to view spindles for the purpose of identifying the stages of cytokinesis. Germline cells were imaged after dissection and placement in Voltalef 10S oil. Live imaging was performed using exposure settings of 250 msec and 4D image sets were acquired every 60 seconds with a Z-interval of 1 micron.

5.2.2 3D Segmentation

Cells were segmented in 3D using a 3D seeded watershed algorithm developed with the MATLAB image processing toolbox (Fig. 5.2). For the first frame of each movie seeds had to be manually initialized. A seed was manually drawn for each cell and the background in each Z-layer to construct 3D seeds. Using these seeds, the 3D watershed algorithm was applied on the 3D Gaussian filtered image stack. For each subsequent time frame, the new seeds were generated by propagating the 'eroded' segmentation results from the previous time frame. An erosion in 3D is a morphological operation which essentially removes the outermost layer or surface of a voxelated object by a specified amount; without erosion the seeds would overlap with the surface of the cell in the next frame and lead to segmentation errors. On some occasions, as will be explained below, the erosion of the previous segmentation still overlapped the cell surface and additional manual intervention was necessary.

There were a number of features in the images that posed challenges for the watershed transform, however, the use of seeds helped overcome these issues. The main types of issues faced were threefold. First, the GFP labeled not only the plasma membrane (PM) of the cells but also the spindle apparatus which forms during cytokinesis. It was often the case that the spindles were just as bright or brighter than the PM. During furrow ingression the spindle density increases near the furrow and appears to co-localize with the PM near the neck of the furrow. To overcome this issue it was necessary, in many of the cases, to manually adjust the boundaries of the seeds to cover the spindles and prevent the watershed surface from 'falling' into the cell and onto the spindles. Second, occasionally the signal to noise (S/N) ratio was very low in certain locations of the cell surface. The side of the cell furthest from the microscope objective will, as a result of increased light scattering, tend to have lower S/N. In some instances however, in z-layers close to the objective there were parts of the membrane that had weaker signal, perhaps as a result of lower local GFP concentrations. To handle these issues it was, again, important to apply careful manipulation of seeds to make sure the segmentation lines did not leak in or outside of the true cell surface location. Third and lastly, on a few rare occasions there were small bright vesicle-like objects that were adjacent to the outside of the cell membrane on some of the cells. These objects sometimes caused the segmentation to protrude outside and essentially include the vesicle-like object with the cell. Again, the solution to this problem was to 'mask out' the object by covering the object (or most of the object) by the background seed. After segmentation was complete the cell could be visualized in 3D using the MATLAB *isosurface* function (Fig. 5.3).

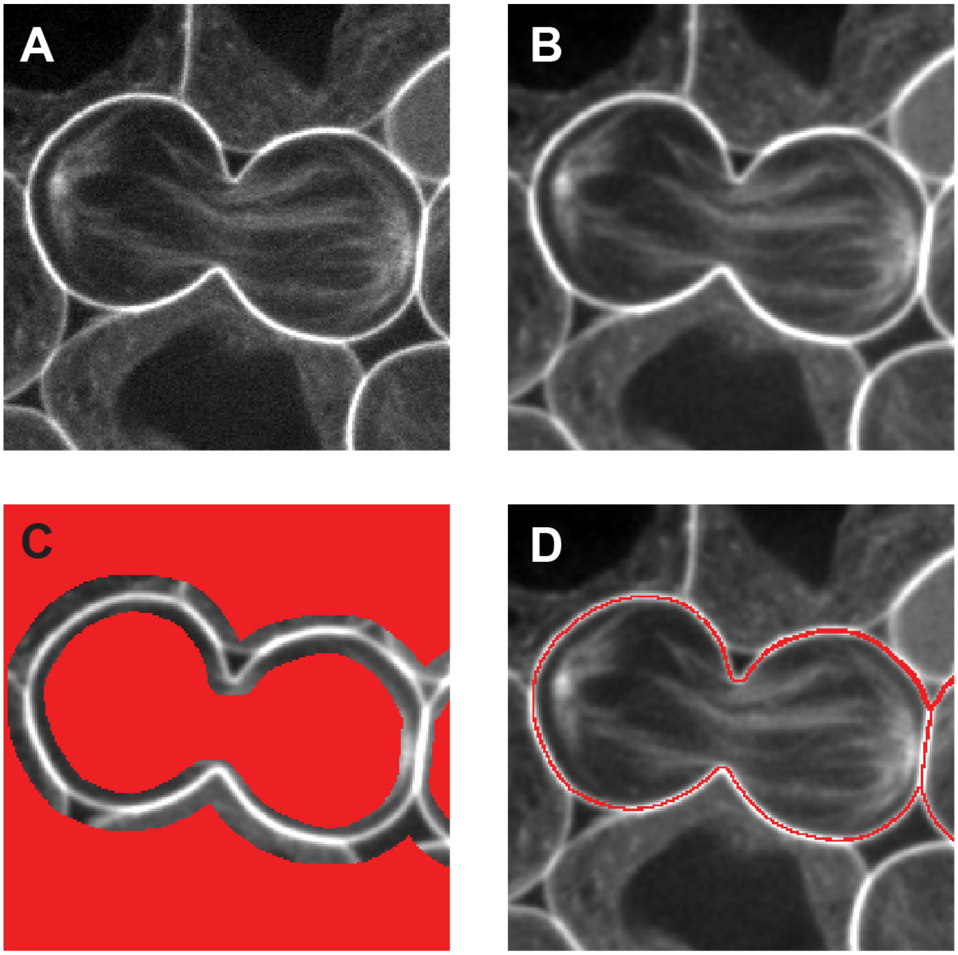

Figure 5.2: 2D cross-section of the seeded watershed transform results. (A) Raw Image of a cell undergoing cytokinesis. (B) Gaussian filter applied to the image. (C) Seeds (red regions) applied to the image to block interior spindles and exterior features. (D) Segmentation lines (in red) overlaid on the filtered image.

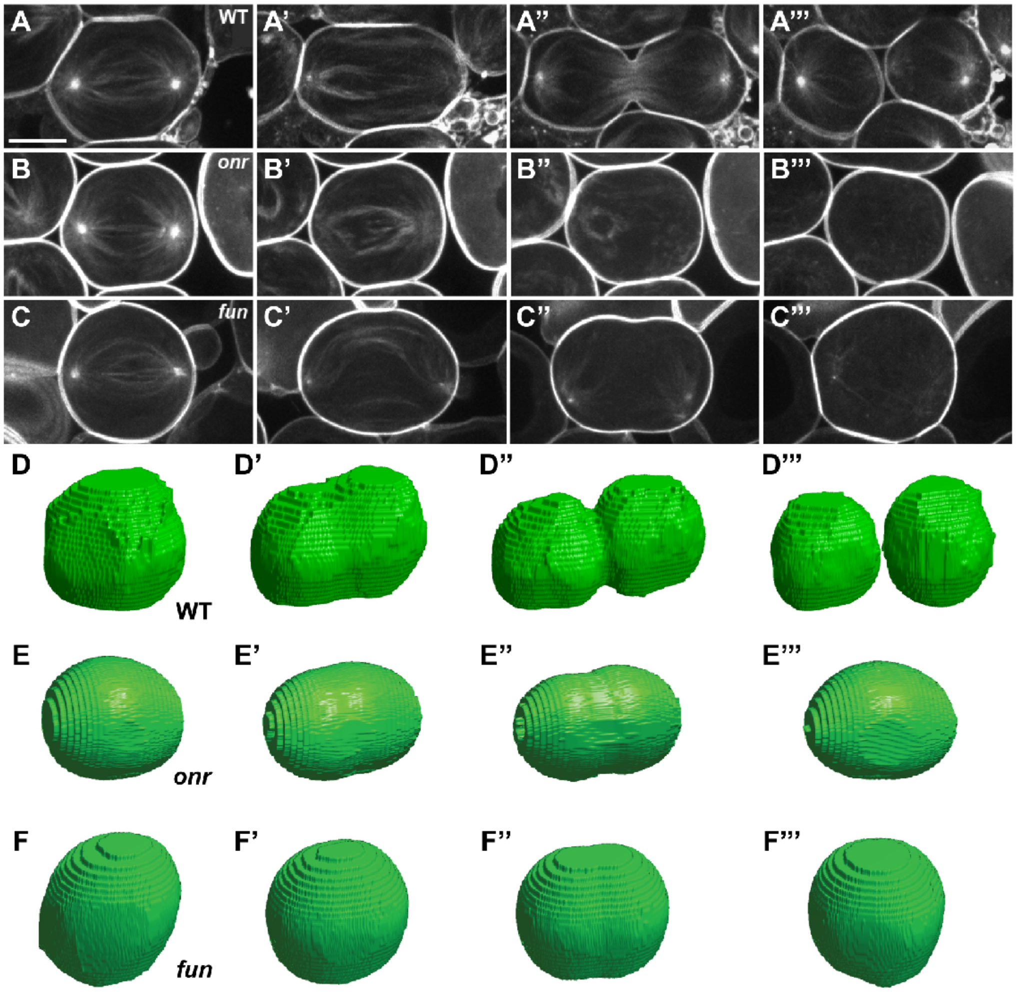

Figure 5.3: 3D segmentation results. (A-C) Still frames from time-lapse confocal microscopy of wild-type (A), *onr* (B), and *fun* mutant (C) male germline cells expressing PLCδd-PH-GFP and β-Tub-GFP (imaged simultaneously in single channel). Cells are shown just prior to elongation (A, B, C), immediately before ingression (A', B', C'), during ingression (A", B", C"), and after successfully completing or failing to complete cytokinesis (A"', B"', C"'). (D-F) Representative segmented and voxelized cells of wild-type (D), *onr* mutant (E), and *fun* mutant (F) cells.

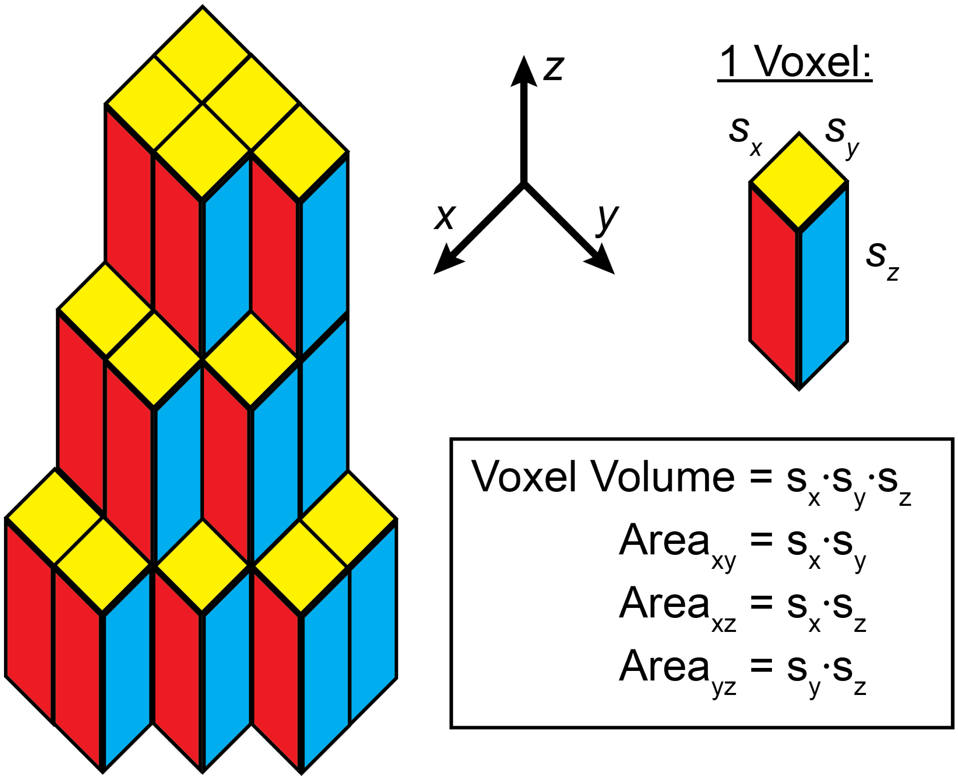

Figure 5.4: Illustration of voxelized object. As is often in the case in 3D imaging, the z-resolution is lower than the x-y resolution resulting in anisotropic voxels. For the data analyzed in this project the pixel size in the x and y dimensions (s_x and s_y) is 0.166 μm and z-layers are acquired every 1 micron ($s_z = 1\mu m$).

5.2.3 Volume and Surface Area Measurements

Measuring the volume of a 3D segmented object is a straightforward computational task. The volume is simply the number of voxels (a 3D pixel) of the segmented region multiplied by the volume of a single voxel. The pixel size in the image data was 0.166 μm and the z-layers were imaged with a spacing of 1 μm so the volume of a voxel would be $0.166\mu m \times 0.166\mu m \times 1\mu m = 0.0276\mu m^3$. The anisotropic nature of the voxels made some other computations a little more complicated as will be pointed out later.

To measure the surface area of a voxelized region the sum of all the ‘exposed’ voxel surfaces was taken, i.e. surfaces touching the background. Due to the anisotropic voxel shape (Fig. 5.4) lateral (x-z or y-z) surfaces have different areas than x-y surfaces and therefore had to be counted differently. The method used to identify and count the surface areas of these two distinct sizes of exposed surfaces was to take the differential of the binary 3D image along the three different axes x, y, and z. The differential along the x dimension, for example, yields a matrix with values of $+1$ in locations where a 0 is followed by a 1 and values of -1 in locations where 1 is followed by a 0 along the x-axis; these locations correspond to y-z exposed surfaces which can then be counted, multiplied by their scale factor, and added to the sum of x-z and x-y surface areas.

5.2.4 Aspect Ratio

The aspect ratio is defined as the length of the major axis divided by the length of the minor axis (Fig. 5.5A). The major axis length in 3D was measured by finding the maximum distance between any pair of surface positions of the cell. As the minor axis length, the diameter of the larger sphere-like lobe of the cell was computed via a 3D distance transform on the 3D binary image of the cell. With these definitions for the major and minor axis length, a sphere will have an aspect ratio of 1, and two just-touching spheres of equal radius will have an aspect ratio of 2. Since cells are frequently deformed due to mechanical contact with neighboring cells, they generally do not approximate spheres.

5.2.5 Convex Hull Volume Ratio

To quantify ingression of the furrow a metric called the convex hull volume ratio (CHVR) was used. The convex hull of a set of points X is the smallest convex set containing X. The convex hull may be visualized as the shape enclosed by a rubber band stretched around a set of 2D coordinates X, or that of a rubber membrane if X is a set of 3D coordinates (Fig. 5.5B). Thus, for a fully convex object the convex

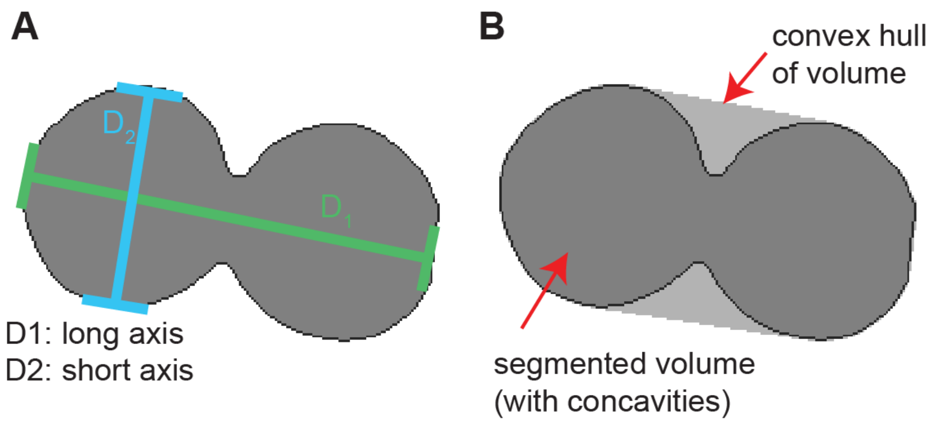

Figure 5.5: Illustration of two metrics that describe cell geometry: (A) the aspect ratio and (B) the convex hull volume ratio (CHVR).

hull of the object is the equivalent to the object itself. The CHVR was defined as the volume of the convex hull divided by the actual volume (i.e., the segmented volume). By this definition the CHVR can be greater or equal to one: equal, in cases where there are no concavities such as a sphere or an ellipsoid and greater than 1 in cases where the cell has concavities such as that generated by a furrow. It should be noted that there will be some small levels of concavities in cell surfaces due to local external or internal forces or due to localization error of the surface, however, these levels of concavity will be small compared to that of a cytokinetic furrow. For an idealized example, the CHVR equals 1.25 for an object composed of two equal sized spheres touching at a point, a situation similar to two daughter cells after cytokinesis is complete. What a CHVR of 1.25 means is that the volume of the concave space is 25% of the volume of the object.

5.2.6 Data Alignment

In order to average time-courses of multiple experiments for a given condition, and to effectively compare wild-type, *onr*, and *fun* conditions with each other, cell shape measurements have to be aligned to a common 'reference' time point that represents the initiation of cytokinesis. While the *onr* and *fun* mutants do not undergo significant rate changes in volume, surface area, or CHVR that could provide useful fiduciary markers for temporal alignment, it was observed that the mutants still undergo a distinct initial increase of their aspect ratio, i.e., they show a small but significant elongation, even in the absence of effective furrow ingression (Fig. 5.3) . An automated algorithm was used to identify this 'shoulder' point of the aspect ratio in each individual cell trace (Fig. 5.6B-D), and used as a reference time point (representing t = 0) for subsequent temporal alignment. Mathematically, the reference time point is the first time point at which the slope of the forward 10 min time window increases by 20% (wild type) or 60% (mutants) relative to the backward 10 min time window (Fig. 5.6A). This automated alignment was in excellent agreement with manual alignment via observation of spindle formation. In a few cases the automated method did not perform well and in these cases our imager, Cayla Jewett, helped with finding the appropriate alignment time by looking at the spindle dynamics.

5.3 Results

5.3.1 *fun* and *onr* Encode *Drosophila* Homologs of Exocyst Complex Subunits

fun and *onr* were identified in a screen for mutations that disrupt cytokinetic events in male germline cells [23]. Previous characterization of *fun* and *onr* revealed that these mutations do not affect central spindle or F-actin ring formation in dividing spermatocytes. Nonetheless, in *fun* and *onr* mutants, cytokinesis fails at an early stage [23]. The fun^{z1010} mutation was mapped to the 83C1;83C4 interval on chromosome III in the region of the Sec8 gene. Deficiency

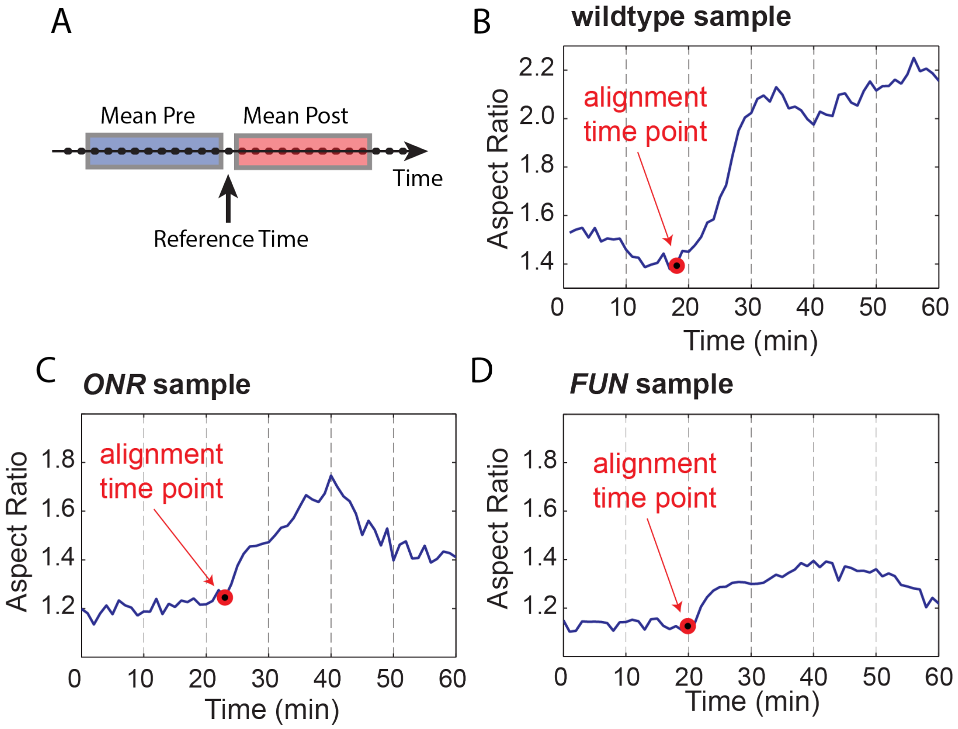

Figure 5.6: Data alignment for multiple cells. (A) Illustration of the time windows (each 10 min) that are used to find significant changes in the aspect ratio and the alignment time. (B-D) Examples showing the alignment times found for WT (B), *onr* (C), and *fun* (D).

mapping revealed that fun^{z1010} failed to complement *Df(3R)Exel6145* for the male sterility and cytokinesis defects (Fig. 5.7A and B). Two lines of evidence indicate that fun^{z1010} is an allele of Drosophila Sec8. First, a 6.6 kb genomic transgene containing the predicted Sec8 coding region, 1.0 kb of upstream promoter sequence, and 1.9 kb of downstream sequence fully rescued the cytokinesis defects in *fun* mutant male germline cells (Fig. 5.7B and D). Indeed, 100% of onion-stage spermatids from $fun^{z1010}/Df(3R)Exel6145$ males bearing a single copy of the rescuing transgene possess a wild type 1:1 ratio of nuclei to nebenkern (n = 102), compared with 0.8% in males of identical genotype devoid of the transgene (n = 125). These results provide evidence that fun^{z1010} represents a mutation in the Sec8 gene.

While fun^{z1010} disrupted functioning of the Sec8 exocyst subunit, the *onr* mutation from the same phenotypic class of mutants [23] was previously shown to affect the Exo84 exocyst subunit [6]. In short, the onr^{z4840} allele possesses a nonsense mutation that is predicted to generate a truncated protein containing 581 of 672 amino acids [6]. Consistent with this, a 4.5 kb genomic transgene containing the predicted Exo84 coding region, 1.5 kb of upstream promoter sequence, and 1 kb of downstream sequence fully rescued cytokinesis defects in *onr* mutant male germline cells (Fig. 5.7C and E; 98.2% of onion-stage spermatids from $onr^{z4840}/Df(3R)Espl3$ hemizygous males bearing a single copy of the rescuing transgene exhibit a wild-type 1:1 ratio of nuclei to nebenkern (n = 112), compared to 0% in *onr* hemizygotes devoid of the transgene (n = 101).

5.3.2 Sec8 Localizes to the Equatorial Cortex

Localization of the exocyst complex protein Sec8 was analyzed in primary spermatocytes from larval testes fixed with methanol-free formaldehyde (Fig. 5.8). Staining of interphase primary spermatocytes with anti-Tubulin and anti-Sec8

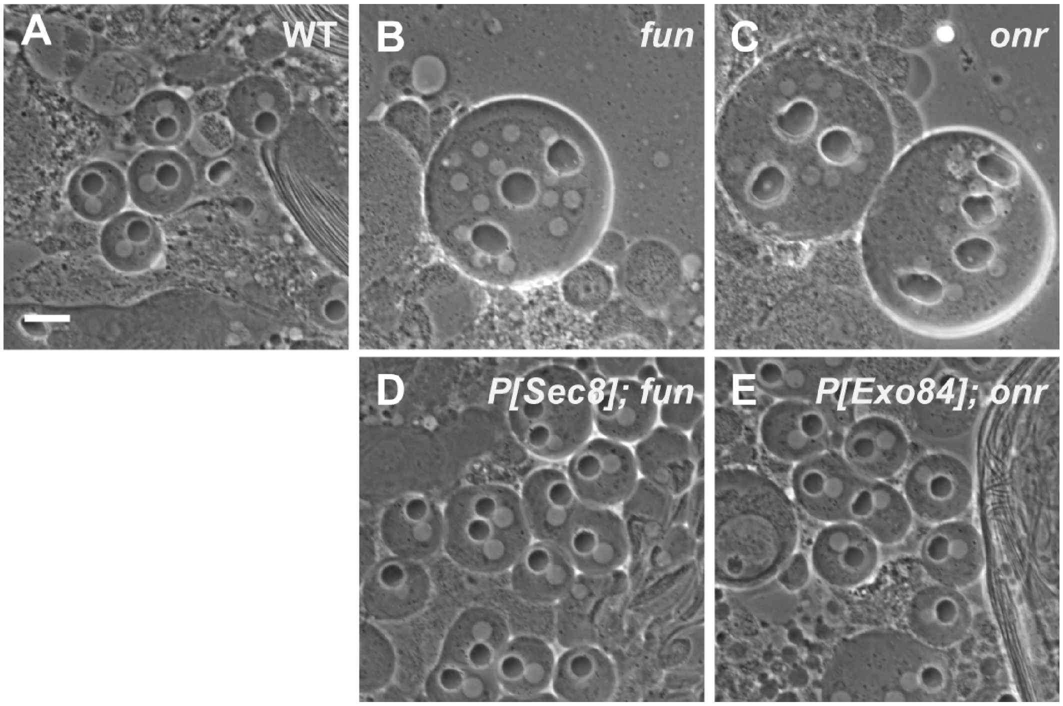

Figure 5.7: Rescue of *fun* and *onr* mutant cells by Sec8 and Exo84. (A) Phase contrast microscopy of wild type, $fun^{z1010}/Df(3R)Exel6145$ mutant (B) and $onr^{z4840}/Df(3R)Espl3$ mutant (C) male germline cells. In *fun* and *onr* mutant cells, cell division fails and multiple nuclei (white spherical objects) are observed in association with enlarged nebenkern (black spherical objects). In wild-type cells, single nuclei are found in association with nebenkern of approximately equal size. A single copy of a transgene containing either genomic Sec8 (D) or genomic Exo84 (E) rescues cytokinesis defects in $fun^{z1010}/Df(3R)Exel6145$ (D) and $onr^{z4840}/Df(3R)Espl3$ (E) mutant cells. Scale bar, 10 μm.

antibodies revealed that Sec8 protein was diffuse throughout the cytoplasm and enriched at the plasma membrane (Fig. 5.8). In dividing spermatocytes, while localized to the plasma membrane, Sec8 was also enriched in a broad cortical area at the cell equator and excluded from the poles (Fig. 5.8). During mid-telo-phase and late telophase, Sec8 protein accumulated at the cortex, near the ingressing furrow membrane (Fig. 5.8).

5.3.3 Failure in Elongation, Furrow Progression, and Membrane Addition in *onr* and *fun*

The dynamics of cell size and shape in wild-type cells were very consistent between cells. Wild-type volume did not change significantly during cytokinesis (Fig. 5.9, $p = 0.5297$ when comparing wild-type cells at $t = 0$ to t =25 min). Cytokinesis is therefore dependent on an increase in surface area (Fig. 5.9). For the idealized geometry of a sphere dividing into two spheres of half the volume, the increase in surface area would be approximately 26%. The wild-type data were in good agreement with this percentage increase (26.1%), and the peak rate of increase is approximately 63 $\mu m^2/min$. The average aspect ratio increased by just over 51.8%, and the average CHVR increased by 23% over the course of 25 minutes (Fig. 5.10). In contrast, onr^{z4840} mutant cells had a brief period where surface area temporarily increased at a peak rate of 5.0 $\mu m^2/min$, and surface area increased by 1.3% over 25 minutes (Fig. 5.9). In fun^{z1010} mutant cells, the peak rate of surface area increase was 3.0 $\mu m^2/min$, a rate similar to *onr* mutants but over 20 times slower than wild type, and the total percent increase over 25 minutes was 2.0% (Fig. 5.9). Intriguingly, cell volume and surface area were nearly identical in wild type, *onr* mutant, and *fun* mutant cells prior to the start cell division, suggesting that there is not a general blockade of plasma membrane trafficking in *onr* and *fun* mutants (Fig. 5.9). This also further suggests that

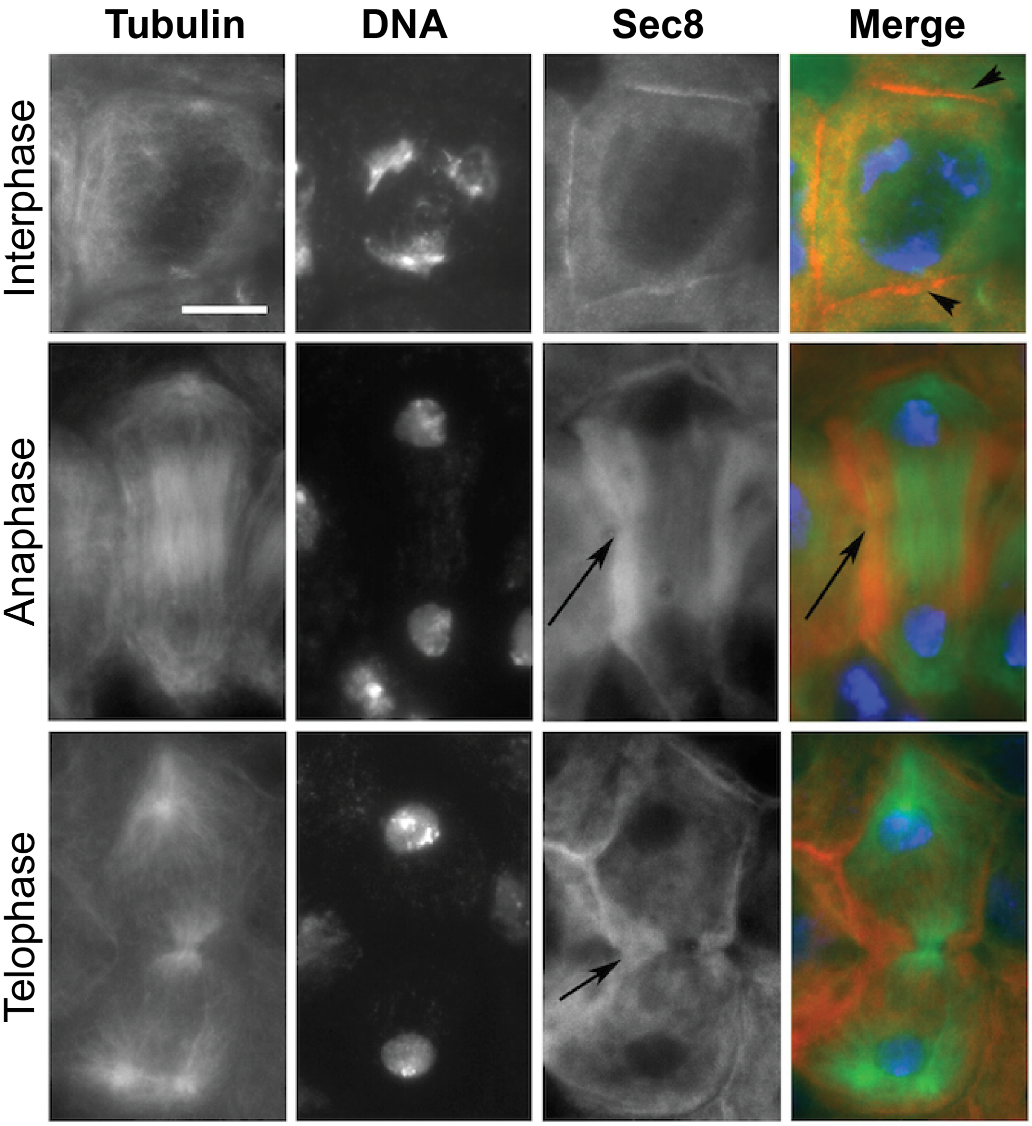

Figure 5.8: Localization of Sec8 protein in wild-type primary spermatocytes. Interphase and dividing spermatocytes were stained for Tubulin (green), Sec8 (red) and DNA (blue). During interphase, Sec8 was mostly diffuse in the cytoplasm and enriched at the plasma membrane (arrowheads). In dividing spermatocytes, Sec8 appeared enriched in a broad cortical band that encircled the midzone (arrows) and was excluded from the poles.

directed trafficking specifically during anaphase cell elongation and cytokinesis may be an essential mediator of cell shape change.

An essential requirement for *onr* and *fun* function during anaphase cell elongation and cytokinesis can also be observed by directly examining the aspect ratio and the CHVR in these two mutants. In both mutants, the aspect ratio initially displayed a slight increase but peaked at 1.5 in onr^{z4840} mutants and at 1.4 in fun^{z1010} mutants before it then started to decline (as compared to 2.4 in wild-type cells). Similarly, cleavage furrow progression was disrupted in *onr* and *fun* mutant cells. Intriguingly, ingression of the cleavage furrow failed almost immediately in spermatocytes lacking *onr* or *fun* function (Fig. 5.10). During this process, the average CHVR reached a peak of 1.015 in *onr* mutants. Thus, on average, the volume of the ingression furrow was at most 1.5% of the cell volume. In *fun* mutant cells the CHVR peaked at 1.018. These results suggest that, in vivo, Exo84 and Sec8 function is required for a core set of cell shape changes that occur during cell division.

5.3.4 Build Up in Internal Membrane Stores and Golgi Bloating in *onr* and *fun* Mutant Cells

Since surface area addition was defective in *onr* and *fun* mutant cells, transmission electron microscopy (TEM) was used to analyze the ultrastructure of spermatocyte cells to determine if internal membrane compartments were altered. Intriguingly, *onr* and *fun* mutant cells displayed large accumulations of cytoplasmic membranes (Fig. 5.11B and C). Indeed, parafusorial and astral membranes appeared enlarged, fragmented and vacuolated in *fun* and *onr* mutant dividing spermatocytes (Fig. 5.11B and C). Golgi compartments were also bloated and vacuolated when *fun* (10/14 Golgi bodies, or 71%) or *onr* (10/10 Golgi bodies, or 100%) functions were disrupted (Fig. 5.11K and L), as compared to wild type

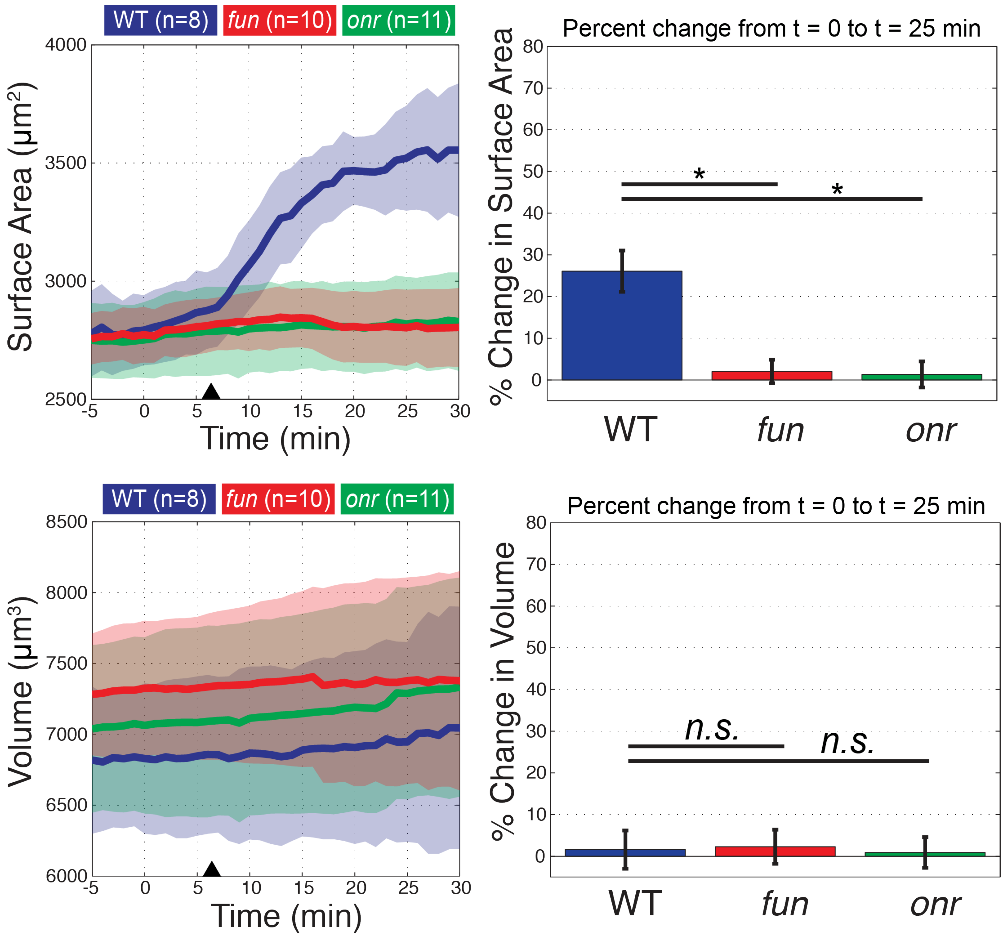

Figure 5.9: Quantitative computational analysis of surface area (A) and volume (B) in wild-type (blue, n=8), *onr* mutant (red, n=10), and *fun* mutant (green, n=11) cells. Left, lines are average values of wild-type, *onr*, and *fun* segmented cells. Data from individual cells were aligned such that t = 0 is the start of anaphase elongation, while arrowheads mark the initiation of cytokinesis in wild-type cells. Right, quantitation of percent change from $t = 0$ to $t = 25$ min. Shaded region indicates standard error; *p<0.0001, significantly different from control in the two-sample Student t-test; n.s. = not significant, p>0.23.

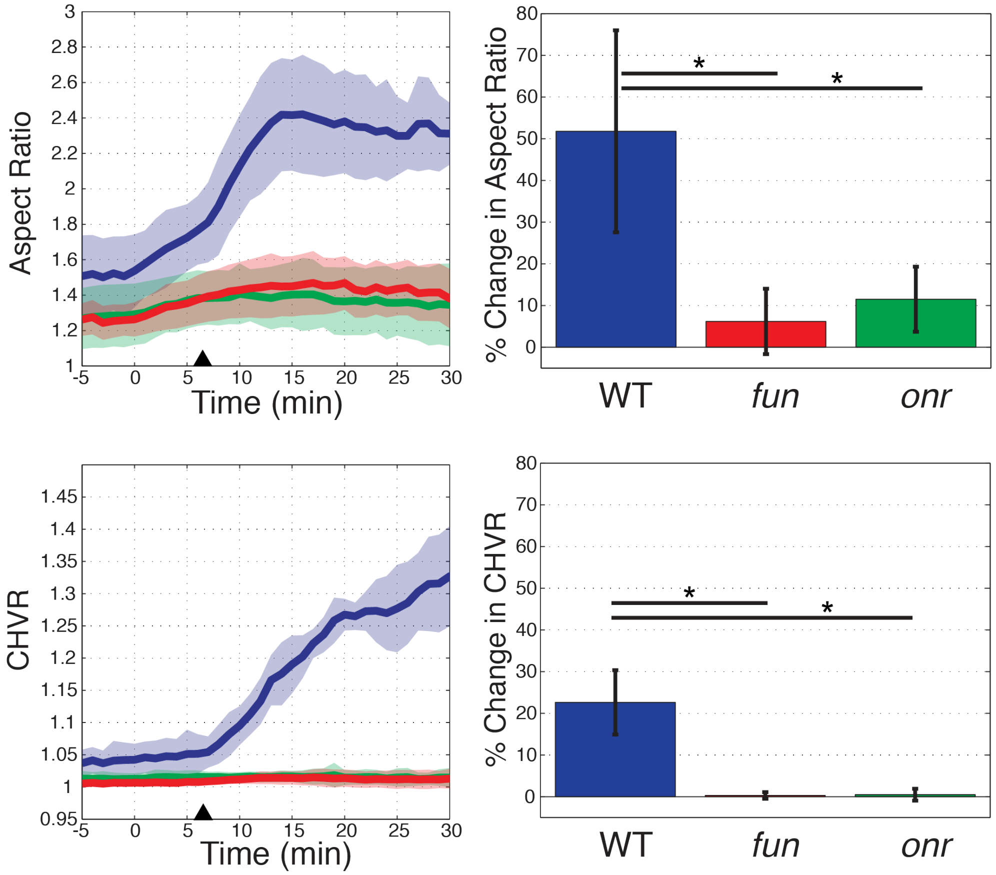

Figure 5.10: Quantitative computational analysis of aspect ratio (A) and convex hull volume ratio (B) in wild-type (blue, n=8), *onr* mutant (red, n=10), and *fun* mutant (green, n=11) cells. Left, lines are average values of wild-type, *onr*, and *fun* segmented cells. Data from individual cells were aligned such that t = 0 is the start of anaphase elongation, while arrowheads mark the initiation of cytokinesis in wild-type cells. Right, quantitation of percent change from $t = 0$ to $t = 25$ min. Shaded region indicates standard error; *p<0.0001, significantly different from control in the two-sample Student t-test; n.s. = not significant, p>0.23.

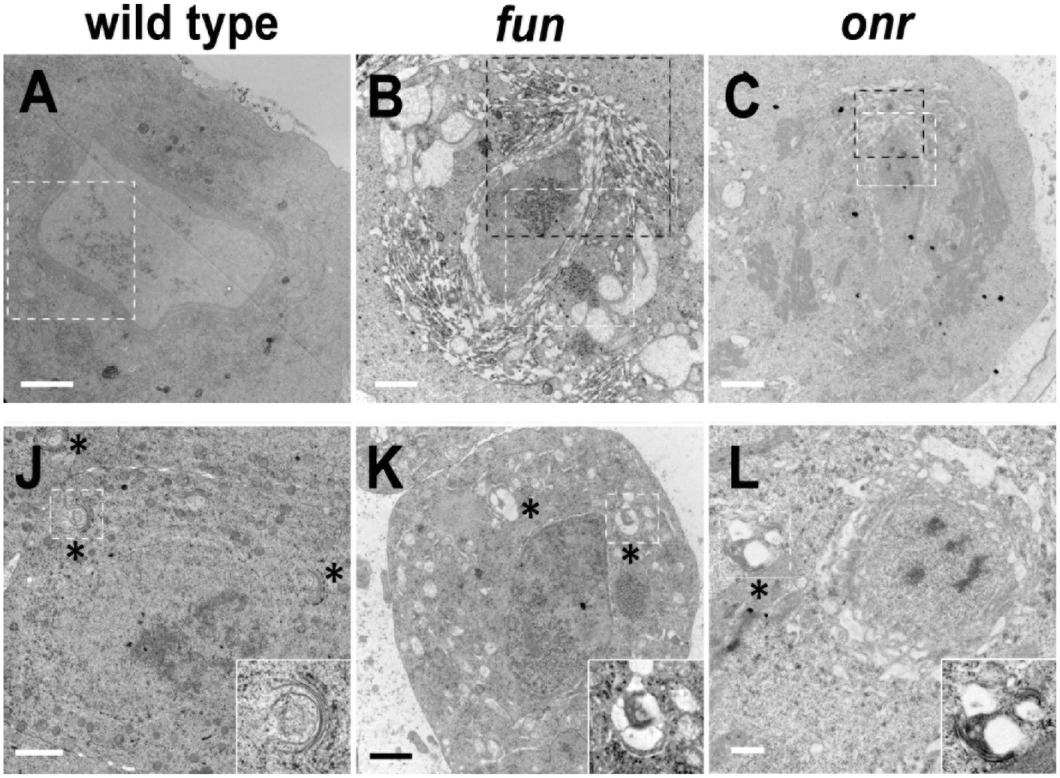

Figure 5.11: TEM showing parafusorial membranes (A-C), and Golgi bodies (J-L) in *fun* and *onr* mutant spermatocytes. Parafusorial and astral membranes (arrows) are enlarged, fragmented and vacuolated in *fun* (B) and *onr* (C) dividing spermatocytes. Golgi bodies (asterisks) show vacuolated regions in *fun* (K) and *onr* (L) mutant spermatocytes. Scale bars are 2 μm (A-C,J,K) or 500 nm (L).

(1/15 Golgi bodies, or 7%). These results are consistent with a failure in vesicle trafficking to the cell surface required to mediate cell remodeling and elongation during anaphase and cytokinesis.

5.4 Discussion

These results indicate that the exocyst complex is required for the major cell shape changes that occur in dividing animal cells during anaphase and telophase. Automated computational analysis of live *Drosophila* spermatocytes shows that membrane addition correlates specifically with onset of anaphase cell elongation and that membrane addition peaks during early stages of cytokinetic furrow ingression in wild-type cells. Spermatocytes carrying mutations in the Exo84 or Sec8 proteins display a greatly reduced rate of surface area growth specifically at anaphase and cytokinesis, indicating a requirement for exocyst complex function in guiding plasma membrane expansion and remodeling in dividing cells. In agreement with this hypothesis, TEM analysis of *onr* and *fun* spermatocytes showed a massive build up of cytoplasmic astral membranes in dividing cells and altered Golgi architecture in interphase primary spermatocytes, suggesting that defective vesicular trafficking through these membrane compartments may result in reduced membrane material for the surface area increase required during anaphase cell elongation and cytokinesis.

These results indicate that a common membrane trafficking pathway may link anaphase cell elongation and cytokinesis. Previous studies have shown a fundamental connection between cell size and the extent of anaphase elongation [25], suggesting that limits in cell size and available surface area may dictate the degree to which elongation of the spindle at anaphase B can occur. The data presented here also demonstrates that cell volume is conserved throughout anaphase and cytokinesis. This implies that, due to geometric constraints, cell surface area must increase as the cell adopts an elongated shape. Consistent with this, surface area addition fails in cells mutant for *onr* or *fun*, and anaphase cell elongation is also disrupted. A small change in aspect ratio is still observed in *onr* and *fun* mutant spermatocytes, which might indicate that a limited reservoir of excess membrane/elasticity exists in the plasma membrane at the beginning of anaphase elongation. Alternatively, this may result from residual exocyst function in the hypomorphic *onr* and *fun* alleles.

Appendix A

List of Publications

- Maria Grazia Giansanti, Timothy E Vanderleest, Cayla E Jewett, Stefano Sechi, Anna Frappaolo, Lacramioara Fabian, Carmen C Robinett, Julie A Brill, Dinah Loerke, Margaret T Fuller, et al. Exocyst-dependent membrane addition is required for anaphase cell elongation and cytokinesis in drosophila. *PLoS genetics*, 11(11):e1005632, 2015.

- Cayla E Jewett, Timothy E Vanderleest, Hui Miao, Yi Xie, Roopa Madhu, Dinah Loerke, and J Todd Blankenship. Planar polarized rab35 functions as an oscillatory ratchet during cell intercalation in the drosophila epithelium. *Nature communications*, 8(1):476, 2017.

- Timothy E Vanderleest, Celia M Smits, Yi Xie, Cayla E Jewett, J Todd Blankenship, and Dinah Loerke. Vertex sliding drives intercalation by radial coupling of adhesion and actomyosin networks during drosophila germband extension. *Elife*, 7:e34586, 2018.

Bibliography

[1] Rolf Adams and Leanne Bischof. Seeded region growing. *Pattern Analysis and Machine Intelligence, IEEE Transactions on*, 16(6):641–647, 1994.

[2] Yanru An, Guosheng Xue, Yang Shaobo, Deng Mingxi, Xiaowei Zhou, Weichuan Yu, Toyotaka Ishibashi, Lei Zhang, and Yan Yan. Apical constriction is driven by a pulsatile apical myosin network in delaminating drosophila neuroblasts. *Development*, 144:2153–2164, 2017.

[3] Andrius Baskys, Ildar Bayazitov, Ercheng Zhu, Liwei Fang, and Rong Wang. Rab-mediated endocytosis: Linking neurodegeneration, neuroprotection, and synaptic plasticity? *Annals of the New York Academy of Sciences*, 1122(1):313–329, 2007.

[4] Claire Bertet, Lawrence Sulak, and Thomas Lecuit. Myosin-dependent junction remodelling controls planar cell intercalation and axis elongation. *Nature*, 429(6992):667–671, 2004.

[5] J Todd Blankenship, Stephanie T Backovic, Justina SP Sanny, Ori Weitz, and Jennifer A Zallen. Multicellular rosette formation links planar cell polarity to tissue morphogenesis. *Developmental cell*, 11(4):459–470, 2006.

[6] J Todd Blankenship, Margaret T Fuller, and Jennifer A Zallen. The drosophila homolog of the exo84 exocyst subunit promotes apical epithelial identity. *Journal of cell science*, 120(17):3099–3110, 2007.

[7] Floris Bosveld, Olga Markova, Boris Guirao, Charlotte Martin, Zhimin Wang, Anaëlle Pierre, Maria Balakireva, Isabelle Gaugue, Anna Ainslie, Nicolas Christophorou, et al. Epithelial tricellular junctions act as interphase cell shape sensors to orient mitosis. *Nature*, 530(7591):495–498, 2016.

[8] Sunitha Byri, Tvisha Misra, Zulfeqhar A Syed, Tilmann Bätz, Jimit Shah, Lukas Boril, Jade Glashauser, Tinri Aegerter-Wilmsen, Till Matzat, Bernard Moussian, et al. The triple-repeat protein anakonda controls epithelial tricellular junction formation in drosophila. *Developmental cell*, 33(5):535–548, 2015.

[9] Clothilde Cauvin, Morgane Rosendale, Neetu Gupta-Rossi, Murielle Rocancourt, Pierre Larraufie, Rémi Salomon, David Perrais, and Arnaud Echard. Rab35 gtpase triggers switch-like recruitment of the lowe syndrome lipid phosphatase ocrl on newborn endosomes. *Current Biology*, 26(1):120–128, 2016.

[10] Andrew D Chalmers and JM Slack. The xenopus tadpole gut: fate maps and morphogenetic movements. *Development*, 127(2):381–392, 2000.

[11] Laurent Chesneau, Daphné Dambournet, Mickaël Machicoane, Ilektra Kouranti, Mitsunori Fukuda, Bruno Goud, and Arnaud Echard. An arf6/rab35 gtpase cascade for endocytic recycling and successful cytokinesis. *Current Biology*, 22(2):147–153, 2012.

[12] Julien Chevallier, Charles Koop, Archana Srivastava, Ryan J Petrie, Nathalie Lamarche-Vane, and John F Presley. Rab35 regulates neurite outgrowth and cell shape. *FEBS letters*, 583(7):1096–1101, 2009.

[13] Claudio Collinet, Matteo Rauzi, Pierre-François Lenne, and Thomas Lecuit. Local and tissue-scale forces drive oriented junction growth during tissue extension. *Nature cell biology*, 17(10):1247–1258, 2015.

[14] Scott Curran, Charlotte Strandkvist, Jasper Bathmann, Marc de Gennes, Alexandre Kabla, Guillaume Salbreux, and Buzz Baum. Myosin ii controls junction fluctuations to guide epithelial tissue ordering. *Developmental cell*, 43(4):480–492, 2017.

[15] Daphné Dambournet, Mickael Machicoane, Laurent Chesneau, Martin Sachse, Murielle Rocancourt, Ahmed El Marjou, Etienne Formstecher, Rémi Salomon, Bruno Goud, and Arnaud Echard. Rab35 gtpase and ocrl phosphatase remodel lipids and f-actin for successful cytokinesis. *Nature cell biology*, 13(8):981–988, 2011.

[16] Rachel E Dawes-Hoang, Kush M Parmar, Audrey E Christiansen, Chris B Phelps, Andrea H Brand, and Eric F Wieschaus. Folded gastrulation, cell shape change and the control of myosin localization. *Development*, 132(18):4165–4178, 2005.

[17] Sérgio de Matos Simões, Avantika Mainieri, and Jennifer A Zallen. Rho gtpase and shroom direct planar polarized actomyosin contractility during convergent extension. *J Cell Biol*, 204(4):575–589, 2014.

[18] Reza Farhadifar, Jens-Christian Röper, Benoit Aigouy, Suzanne Eaton, and Frank Jülicher. The influence of cell mechanics, cell-cell interactions, and proliferation on epithelial packing. *Current Biology*, 17(24):2095–2104, 2007.

[19] Rodrigo Fernandez-Gonzalez, Sérgio de Matos Simoes, Jens-Christian Röper, Suzanne Eaton, and Jennifer A Zallen. Myosin ii dynamics are regulated by tension in intercalating cells. *Developmental cell*, 17(5):736–743, 2009.

[20] Rodrigo Fernandez-Gonzalez and Jennifer A Zallen. Oscillatory behaviors and hierarchical assembly of contractile structures in intercalating cells. *Physical biology*, 8(4):045005, 2011.

[21] Donald T Fox and Mark Peifer. Abelson kinase (abl) and rhogef2 regulate actin organization during cell constriction in drosophila. *Development*, 134(3):567–578, 2007.

[22] Stéphane Frémont, Hussein Hammich, Jian Bai, Hugo Wioland, Kerstin Klinkert, Murielle Rocancourt, Carlos Kikuti, David Stroebel, Guillaume Romet-Lemonne, Olena Pylypenko, et al. Oxidation of f-actin controls the terminal steps of cytokinesis. *Nature communications*, 8:14528, 2017.

[23] Maria Grazia Giansanti, Rebecca M Farkas, Silvia Bonaccorsi, Dan L Lindsley, Barbara T Wakimoto, Margaret T Fuller, and Maurizio Gatti. Genetic dissection of meiotic cytokinesis in drosophila males. *Molecular biology of the cell*, 15(5):2509–2522, 2004.

[24] Bianka L Grosshans, Darinel Ortiz, and Peter Novick. Rabs and their effectors: achieving specificity in membrane traffic. *Proceedings of the National Academy of Sciences*, 103(32):11821–11827, 2006.

[25] Yuki Hara and Akatsuki Kimura. Cell-size-dependent spindle elongation in the caenorhabditis elegans early embryo. *Current Biology*, 19(18):1549–1554, 2009.

[26] Camille A Hardiman, Justin A McDonough, Hayley J Newton, and Craig R Roy. The role of rab gtpases in the transport of vacuoles containing legionella

pneumophila and coxiella burnetii. *Biochemical Society Transactions*, 40(part 6):1353–1359, 2012.

[27] Conor P Horgan and Mary W McCaffrey. Endosomal trafficking in animal cytokinesis. *Front Biosci (Schol Ed)*, 4:547–555, 2012.

[28] Ming-Kuang Hsu, Jiun-Chyuan Sheu, and Cesar Hsue. Overcoming the negative frequencies-instantaneous frequency and amplitude estimation using osculating circle method. *Journal of Marine Science and Technology*, 19(5):514–521, 2011.

[29] Junichi Ikenouchi, Mikio Furuse, Kyoko Furuse, Hiroyuki Sasaki, Sachiko Tsukita, and Shoichiro Tsukita. Tricellulin constitutes a novel barrier at tricellular contacts of epithelial cells. *The Journal of cell biology*, 171(6):939–945, 2005.

[30] Kenneth D Irvine and Eric Wieschaus. Cell intercalation during drosophila germband extension and its regulation by pair-rule segmentation genes. *Development*, 120(4):827–841, 1994.

[31] C Yu Jessica and Rodrigo Fernandez-Gonzalez. Local mechanical forces promote polarized junctional assembly and axis elongation in drosophila. *Elife*, 5:e10757, 2016.

[32] Cayla E Jewett, Timothy E Vanderleest, Hui Miao, Yi Xie, Roopa Madhu, Dinah Loerke, and J Todd Blankenship. Planar polarized rab35 functions as an oscillatory ratchet during cell intercalation in the drosophila epithelium. *Nature communications*, 8(1):476, 2017.

[33] Karen E Kasza, Dene L Farrell, and Jennifer A Zallen. Spatiotemporal control of epithelial remodeling by regulated myosin phosphorylation. *Proceedings of the National Academy of Sciences*, 111(32):11732–11737, 2014.

[34] Dilpreet Kaur and Yadwinder Kaur. Various image segmentation techniques: a review. *International Journal of Computer Science and Mobile Computing*, 3(5):809–814, 2014.

[35] Ray Keller, Lance Davidson, Anna Edlund, Tamira Elul, Max Ezin, David Shook, and Paul Skoglund. Mechanisms of convergence and extension by cell intercalation. *Philosophical Transactions of the Royal Society of London B: Biological Sciences*, 355(1399):897–922, 2000.

[36] H Kobayashi, K Etoh, N Ohbayashi, and M Fukuda. Rab35 promotes the recruitment of rab8, rab13 and rab36 to recycling endosomes through mical-l1 during neurite outgrowth. *Biology open*, 3(9):803–814, 2014.

[37] Hotaka Kobayashi and Mitsunori Fukuda. Rab35 regulates arf6 activity through centaurin-β2 (acap2) during neurite outgrowth. *Journal of Cell Science*, 125:2235–2243, 2012.

[38] Ilektra Kouranti, Martin Sachse, Nassim Arouche, Bruno Goud, and Arnaud Echard. Rab35 regulates an endocytic recycling pathway essential for the terminal steps of cytokinesis. *Current biology*, 16(17):1719–1725, 2006.

[39] L LeGoff and T Lecuit. Mechanical forces and growth in animal tissues. *Cold Spring Harbor perspectives in biology*, 8(3):a019232, 2015.

[40] MARIA Leptin and BARBARA Grunewald. Cell shape changes during gastrulation in drosophila. *Development*, 110(1):73–84, 1990.

[41] Romain Levayer, Anne Pelissier-Monier, and Thomas Lecuit. Spatial regulation of dia and myosin-ii by rhogef2 controls initiation of e-cadherin endocytosis during epithelial morphogenesis. *Nature cell biology*, 13(5):529, 2011.

[42] Soeren S Lienkamp, Kun Liu, Courtney M Karner, Thomas J Carroll, Olaf Ronneberger, John B Wallingford, and Gerd Walz. Vertebrate kidney tubules

elongate using a planar cell polarity–dependent, rosette-based mechanism of convergent extension. *Nature genetics*, 44(12):1382, 2012.

[43] Adam C Martin, Matthias Kaschube, and Eric F Wieschaus. Pulsed contractions of an actin–myosin network drive apical constriction. *Nature*, 457(7228):495, 2009.

[44] Frank M Mason, Michael Tworoger, and Adam C Martin. Apical domain polarization localizes actin–myosin activity to drive ratchet-like apical constriction. *Nature cell biology*, 15(8):926, 2013.

[45] Shreya Mitra, Kwai W Cheng, and Gordon B Mills. Rab gtpases implicated in inherited and acquired disorders. In *Seminars in cell & developmental biology*, volume 22, pages 57–68. Elsevier, 2011.

[46] Akankshi Munjal, Jean-Marc Philippe, Edwin Munro, and Thomas Lecuit. A self-organized biomechanical network drives shape changes during tissue morphogenesis. *Nature*, 524(7565):351, 2015.

[47] C Noirot-Timothée, F Graf, and CH Noirot. The specialization of septate junctions in regions of tricellular junctions: Ii. pleated septate junctions. *Journal of ultrastructure research*, 78(2):152–165, 1982.

[48] Suzanne R Pfeffer. Structural clues to rab gtpase functional diversity. *Journal of Biological Chemistry*, 280(16):15485–15488, 2005.

[49] Matteo Rauzi, Pierre-François Lenne, and Thomas Lecuit. Planar polarized actomyosin contractile flows control epithelial junction remodelling. *Nature*, 468(7327):1110–1114, 2010.

[50] Matteo Rauzi, Pascale Verant, Thomas Lecuit, and Pierre-François Lenne. Nature and anisotropy of cortical forces orienting drosophila tissue morphogenesis. *Nature cell biology*, 10(12):1401, 2008.

[51] Chiara Recchi and Miguel C Seabra. Novel functions for rab gtpases in multiple aspects of tumour progression. *Biochemical Society Transactions*, 40(part 6):1398–1403, 2012.

[52] Martin Resnik-Docampo, Christopher L Koehler, Rebecca I Clark, Joseph M Schinaman, Vivien Sauer, Daniel M Wong, Sophia Lewis, Cecilia D'Alterio, David W Walker, and D Leanne Jones. Tricellular junctions regulate intestinal stem cell behaviour to maintain homeostasis. *Nature cell biology*, 19(1):52, 2017.

[53] Minna Roh-Johnson, Gidi Shemer, Christopher D Higgins, Joseph H McClellan, Adam D Werts, U Serdar Tulu, Liang Gao, Eric Betzig, Daniel P Kiehart, and Bob Goldstein. Triggering a cell shape change by exploiting preexisting actomyosin contractions. *Science*, page 1217869, 2012.

[54] Jessica K Sawyer, Wangsun Choi, Kuo-Chen Jung, Li He, Nathan J Harris, and Mark Peifer. A contractile actomyosin network linked to adherens junctions by canoe/afadin helps drive convergent extension. *Molecular biology of the cell*, 22(14):2491–2508, 2011.

[55] Jodi Schottenfeld-Roames and Amin S Ghabrial. Whacked and rab35 polarize dynein-motor-complex-dependent seamless tube growth. *Nature cell biology*, 14(4):386, 2012.

[56] Joost Schulte, Ulrich Tepass, and Vanessa J Auld. Gliotactin, a novel marker of tricellular junctions, is necessary for septate junction development in drosophila. *The Journal of cell biology*, 161(5):991–1000, 2003.

[57] Sérgio Simões, Youjin Oh, Michael FZ Wang, Rodrigo Fernandez-Gonzalez, and Ulrich Tepass. Myosin ii promotes the anisotropic loss of the apical domain during drosophila neuroblast ingression. *J Cell Biol*, 216(5):1387–1404, 2017.

[58] Jerome Solon, Aynur Kaya-Copur, Julien Colombelli, and Damian Brunner. Pulsed forces timed by a ratchet-like mechanism drive directed tissue movement during dorsal closure. *Cell*, 137(7):1331–1342, 2009.

[59] LA Staehelin. Further observations on the fine structure of freeze-cleaved tight junctions. *Journal of Cell Science*, 13(3):763–786, 1973.

[60] Zijun Sun, Christopher Amourda, Murat Shagirov, Yusuke Hara, Timothy E Saunders, and Yusuke Toyama. Basolateral protrusion and apical contraction cooperatively drive drosophila germ-band extension. *Nature cell biology*, 19(4):375, 2017.

[61] DARI Sweeton, SUKI Parks, MICHAEL Costa, and ERIC Wieschaus. Gastrulation in drosophila: the formation of the ventral furrow and posterior midgut invaginations. *Development*, 112(3):775–789, 1991.

[62] Michiko Takeda, Mustafa M Sami, and Yu-Chiun Wang. A homeostatic apical microtubule network shortens cells for epithelial folding via a basal polarity shift. *Nature cell biology*, 20(1):36, 2018.

[63] Robert J Tetley, Guy B Blanchard, Alexander G Fletcher, Richard J Adams, and Bénédicte Sanson. Unipolar distributions of junctional myosin ii identify cell stripe boundaries that drive cell intercalation throughout drosophila axis extension. *Elife*, 5:e12094, 2016.

[64] Consuelo Tudela, Miguel-Angel Formoso, Tamara Martinez, Raquel Perez, Marta Aparicio, Carmen Maestro, Aurora Del Rio, Elena Martinez, Mark Ferguson, and Concepcion Martinez-Alvarez. Tgf-beta3 is required for the adhesion and intercalation of medial edge epithelial cells during palate fusion. *International Journal of Developmental Biology*, 46(3):333–336, 2002.

[65] Valerie Uytterhoeven, Sabine Kuenen, Jaroslaw Kasprowicz, Katarzyna Miskiewicz, and Patrik Verstreken. Loss of skywalker reveals synaptic endosomes as sorting stations for synaptic vesicle proteins. *Cell*, 145(1):117–132, 2011.

[66] Athea Vichas and Jennifer A Zallen. Translating cell polarity into tissue elongation. In *Seminars in cell & developmental biology*, volume 22, pages 858–864. Elsevier, 2011.

[67] Jianbo Wang, Sharayne Mark, Xiaohui Zhang, Dong Qian, Seung-Jong Yoo, Kristen Radde-Gallwitz, Yanping Zhang, Xi Lin, Andres Collazo, Anthony Wynshaw-Boris, et al. Regulation of polarized extension and planar cell polarity in the cochlea by the vertebrate pcp pathway. *Nature genetics*, 37(9):980, 2005.

[68] Yu-Chiun Wang, Zia Khan, Matthias Kaschube, and Eric F Wieschaus. Differential positioning of adherens junctions is associated with initiation of epithelial folding. *Nature*, 484(7394):390, 2012.

[69] Yu-Chiun Wang, Zia Khan, and Eric F Wieschaus. Distinct rap1 activity states control the extent of epithelial invagination via α-catenin. *Developmental cell*, 25(3):299–309, 2013.

[70] Stephanie C Weber, Michael A Thompson, WE Moerner, Andrew J Spakowitz, and Julie A Theriot. Analytical tools to distinguish the effects of localization error, confinement, and medium elasticity on the velocity autocorrelation function. *Biophysical journal*, 102(11):2443–2450, 2012.

[71] Jennifer A Zallen and Eric Wieschaus. Patterned gene expression directs bipolar planar polarity in drosophila. *Developmental cell*, 6(3):343–355, 2004.